Isolating and Discriminating Overlapping Signatures in Cluttered Environments

MR-1664

Final Report

Submitted to

Strategic Environmental Research and Development Program (SERDP)

February 21, 2013

Revision **2.0**

By

U.S. Army Corps of Engineers (USACE) Engineering Research and Development Center (ERDC)
Cold Regions Research and Engineering Laboratory (CRREL)
72 Lyme Road
Hanover, NH 03755

Principal Investigators
Drs. Ben Barrowes and Fridon Shubitidze
benjamin.e.barrowes@usace.army.mil

REPORT DOCUMENTATION PAGE

Form Approved
OMB No. 0704–0188

The public reporting burden for this collection of information is estimated to average 1 hour per response, including the time for reviewing instructions, searching existing data sources, gathering and maintaining the data needed, and completing and reviewing the collection of information. Send comments regarding this burden estimate or any other aspect of this collection of information, including suggestions for reducing this burden to Department of Defense, Washington Headquarters Services, Directorate for Information Operations and Reports (0704–0188), 1215 Jefferson Davis Highway, Suite 1204, Arlington, VA 22202–4302. Respondents should be aware that notwithstanding any other provision of law, no person shall be subject to any penalty for failing to comply with a collection of information if it does not display a currently valid OMB control number. **PLEASE DO NOT RETURN YOUR FORM TO THE ABOVE ADDRESS.**

1. REPORT DATE *(DD–MM–YYYY)*	2. REPORT TYPE	3. DATES COVERED *(From — To)*
12–15–2012	Final	05 January 2009 — 20 February 2012

4. TITLE AND SUBTITLE

Isolating and Discriminating Overlapping Signatures in Cluttered Environments

5a. CONTRACT NUMBER

W74RDV10601876

5b. GRANT NUMBER

5c. PROGRAM ELEMENT NUMBER

6. AUTHOR(S)

Barrowes, Benjamin, E., and Shubitidze, Fridon

5d. PROJECT NUMBER

MR-1664

5e. TASK NUMBER

5f. WORK UNIT NUMBER

7. PERFORMING ORGANIZATION NAME(S) AND ADDRESS(ES)

U.S. Army Corps of Engineers, Engineer Research and Development Center
Cold Regions Research and Engineering Laboratory (CRREL)
72 Lyme Road
Hanover, NH 03755

8. PERFORMING ORGANIZATION REPORT NUMBER

9. SPONSORING / MONITORING AGENCY NAME(S) AND ADDRESS(ES)

SERDP Program Office
901 North Stuart Street, Suite 303
Arlington, Virginia 22203-1821
(703) 696-2127

10. SPONSOR/MONITOR'S ACRONYM(S)

11. SPONSOR/MONITOR'S REPORT NUMBER(S)

12. DISTRIBUTION / AVAILABILITY STATEMENT

Approval for public release; distribution is unlimited.

13. SUPPLEMENTARY NOTES

The views, opinions and/or findings contained in this report are those of the authors and should not be construed as an official U.S. Government position, policy or decision, unless so designated by other documentation.

14. ABSTRACT

SERDP project MR-1664 entitled "Isolating and Discriminating Overlapping Signatures in Cluttered Environments" is complete. Significant progress has been made in the dual purposes of this project: 1) to estimate the number of targets simultaneously in the field of view of the sensor, and 2) isolate the contribution to the EMI signal and find their features through inversion indiviually. During the course of this project, we developed the Joint Diagonalization method which estimates the number of targets simultaneously in the field of view of the sensor in real-time. By finding the eigenvalues of the Multistatic Response Matrix (MSR) and interpreting the number of eigenvalues that rise above the noise level, the number of targets present in the data can be rapidly estimated. This estimate in turn is used as an input to our multitarget inversion solvers. We have developed a multidipole Gauss-Newton solver and the Orthonormalized Volume Magnetic Source method (ONVMS) . These combined methods can reliably find up to six targets simultaneously in lab data and have shown unsurpassed results in live site demonstrations.

15. SUBJECT TERMS

keywords; electromagnetic induction, multiple targets, rigorous models, inversion, dipole model, joint diagonalization, ONVMS, multitarget, time domain

16. SECURITY CLASSIFICATION OF:			17. LIMITATION OF ABSTRACT	18. NUMBER OF PAGES	19a. NAME OF RESPONSIBLE PERSON
a. REPORT	b. ABSTRACT	c. THIS PAGE			Benjamin E. Barrowes
U	U	U	UU	122	19b. TELEPHONE NUMBER *(include area code)* (603)646-4822

Contents

1 Abstract **iii**

2 Objectives **1**

3 Background **2**

4 Materials and Methods **3**
4.1 Canonical Targets . . . 3
4.2 Multiple Dipole Inversion . . . 8
4.2.a Introduction . . . 8
4.2.b Problem configuration and EMI sensors . . . 9
4.2.c Data analysis . . . 11
4.2.d Inversion results . . . 15
4.2.d.(1) MPV data . . . 15
4.2.d.(2) TEMTADS data . . . 17
4.2.e Discussion and Conclusions . . . 23
4.3 The Joint Diagonalization Technique . . . 27
4.3.a Introduction . . . 27
4.3.b Methods . . . 28
4.3.b.(1) The TEMTADS sensor array . . . 28
4.3.b.(2) Multi-static response matrices . . . 28
4.3.b.(3) Time development of the MSR eigenvalues . . . 31
4.3.c Results . . . 32
4.3.c.(1) Test-stand measurements . . . 32
4.3.c.(2) Camp Butner blind test . . . 38
4.3.d Conclusion . . . 44
4.4 The ONVMS Method . . . 46
4.4.a Introduction . . . 46
4.4.b Methods . . . 48
4.4.c Results . . . 51
4.4.c.(1) A Test-Stand Experiment . . . 52
4.4.c.(2) Camp Butner TEMTADS Data . . . 57
4.4.d Conclusion . . . 60

5 Results and Discussion **62**
5.1 TEMTADS Data and Results . . . 62
5.2 MetalMapper Data and Results . . . 62
5.3 MPV2 Data . . . 65
5.4 Camp Butner Results . . . 69
5.4.a Introduction . . . 69
5.4.b Methods . . . 70
5.4.b.(1) Data inversion . . . 70
5.4.b.(2) Classification . . . 72

5.4.c Results 74
5.4.d Conclusions 78
5.5 Camp Beale Results 81
5.5.a Introduction 81
5.5.b 2 × 2 TEMTADS Inversion Scheme 83
5.5.c Inversion and Classification Scheme for MPV-II Data 89
5.5.d Conclusion 89

6 Conclusions and Implications 94

APPENDICES

A Appendices – Supporting Data 95
A.1 MPV Single Target Blind Test Results 95
A.2 Previous Multiple Target Inversion Results 95
A.2.a GEM-3 Data over 2 UXO 96
A.2.b Projection of GEM-3 Data over 1 UXO Obscured by Clutter 96
A.3 Simplified Model of the MSR Matrix 97
A.4 Algorithm for Joint Diagonalization 100
A.5 The Green Tensor 101

B List of Scientific/Technical Publications 102

C Other Supporting Materials 102

References 102

1 Abstract

SERDP project MR-1664 entitled "Isolating and Discriminating Overlapping Signatures in Cluttered Environments" is complete. Significant progress has been made in working toward the original objectives of the project. Three new methods for localizing multiple sources in close proximity using EMI data have been developed, tested in lab settings, and applied to field data. Specifically, these methods are:

- A multiple dipole search method based on a Gauss-Newton gradient search algorithm utilizing an analytical Jacobian (see Sec. 4.2)
- A Joint Diagonalization (JD) method for quickly estimating the number of targets presented in the data (see Sec. 4.3)
- A Orthonormalized Volume Magnetic Source (ONVMS) method (see Sec. 4.4)

Canonical targets of various shapes, sizes and material parameters have been fabricated (see Sec. 4.1. Data acquired from these targets as well as standard UXO targets has been acquired by the TEMTADS and MPV2 instruments in many multitarget configurations (see Sec. 4.1). The methods developed under this MR-1664 have been able to isolate and discriminate up to six targets simultaneously in the case of lab data (see Sec. 5).

The JD method is able to almost instantaneously provide a good estimate for the number of distinct targets in the EMI data. After this estimate is obtained, the first or second methods delineated above (and described below) are used to invert for the parameters of the N identified targets. The combined JD ONVMS approach has been applied to data acquired from several instruments and from several different live site demonstrations. For example, when applied to the data from Camp Beale, this combined method was able to find all the Targets of Interest (TOI) with few false positives. Additionally, this method found all the small fuze targets in the midst of up to five other pieces of clutter (see Fig. 5.16). No other method or group was able to find all of the fuzes.

Using these methods, researchers and industry can more confidently leave innocuous scrap in the ground, saving time and resources.

List of Acronyms (and page references to first use)

APG	Aberdeen Proving Ground – first used on page (40)
BOR	Body of Revolution – first used on page (12)
BSS	blind source separation – first used on page (2)
CRREL	Cold Regions Research and Engineering Lab – first used on page (1)
EM	Expectation Maximization – first used on page (1)
EMI	Electromagnetic Induction – first used on page (1)
ERDC	Engineering Research and Development Center – first used on page (1)
ESTCP	Environmental Security Technology Certification Program – first used on page (2)
FY	fiscal year – first used on page (3)
GPR	Ground Penetrating Radar – first used on page (2)
HAP	H-magnetic field, A-Magnetic vector potential, P-magnetic scalar potential – first used on page (1)
JD	Joint Diagonalization – first used on page (iii)
MEC	Munitions and Explosives of Concern – first used on page (2)
MIT	Massachusetts Institute of Technology – first used on page (3)
MM	Munitions Management – first used on page (iii)
MPV	Man-Portable Vector – first used on page (iii)
MPV2	Man-Portable Vector Sensor, Version 2.0 – first used on page (iii)
MQS	magnetoquasistatic – first used on page (64)
MR	Munitions Response – first used on page (iii)
MSR	Multistatic Response Matrix – first used on page (1)
MUSIC	Multiple Signal Classifier – first used on page (2)
NSMS	Normalized Surface Magnetic Source – first used on page (1)
ONVMS	Orthonormalized Volume Magnetic Source – first used on page (1)
SEA	Standardized Excitations Approach – first used on page (1)
SERDP	Strategic Environmental Research and Development Program – first used on page (iii)
SNR	signal to noise ratio – first used on page (3)
SVM	Support Vector Machines – first used on page (1)
TEMTADS	Time-domain Electromagnetic Multi-sensor Tower Array Detection System – first used on page (iii)
TOI	Targets of Interest – first used on page (iii)
USACE	United States Army Corps of Engineers – first used on page (1)
UXO	UneXploded Ordnance – first used on page (iii)

Keywords: electromagnetic induction, multiple targets, rigorous models, inversion, dipole model, joint diagonalization, ONVMS

Acknowledgements: This project was funded by the Strategic Environmental Research and Development Program (SERDP) under project MR-1664. Drs. Jeff Marqusee, Anne Andrews, Herb Nelson, and the review committee for SERDP, provided support and constructive reviews during the course of the project. Thanks also go to Dr. Nicolas Lhomme of Sky Research who closelay collaborated on this project and shepherded the MPV instrument into the MPV-2.

List of Figures

4.1 Spheroid collection used for testing. Specifications are listed in Table 1. 4
4.2 Larger steel spheroids SS1-SP6. Specifications are listed in Table 2. 6
4.3 Larger steel spheroids SP7-SO4. Specifications are listed in Table 2. 7
4.4 EMI Sensor Problem Configuration 10
4.5 Time domain polarizabilities for two types of UXO (81-mm and BLU26) measured and inverted separately from MPV data. 16
4.6 Time domain polarizabilities for two two-target configurations measured by the MPV. Inverted positions are summarized in Table 4. 18
4.7 Time domain polarizabilities and inverted positions for three independent UXO using TEMTADS data. 20
4.8 Time dependent polarizabilities for two-target inversions 21
4.9 Three-target inversions from TEMTADS data. The mortar and the baseplate are held fixed at $(x,y,z) = (0,0,60)$ [cm] and $(x,y,z) = (50,0,49)$ [cm], respectively, while the nose-cone moves along $\hat{x}$ from case to case. True and inverted positions are given in Table 7. 24
4.10 The TEMTADS Sensor 29
4.11 A test-stand experiment featuring an increasing number of targets under interrogation by TEMTADS. As in Fig. 4.10, the system is observed essentially head-on from the $+\hat{\mathbf{y}}$-direction. 33
4.12 (a) Eigenvalues of the TEMTADS multi-static response matrix for a 105-mm M60 howitzer shell (shown in the inset). (b) Eigenvalues of the TEMTADS multi-static response matrix for a 60-mm M49 mortar round (shown in the inset). 34
4.13 Measured eigenvalues for an aluminum sphere of diameter 10 cm (upper) and a steel prolate spheroid (lower) of minor and major axes respectively 4 and 20 cm. 35
4.14 Eigenvalues for the 60-mm round computed using joint diagonalization for three different object locations. 36
4.15 Eigenvalues for the 60-mm round computed using the SVD at each time gate for three different object locations. 37
4.16 MSR eigenvalues of the test-stand measurement as the munitions of the sphere and spheroid (c) of Fig. 4.13. 39
4.17 MSR eigenvalues for 3 TEMTADS cases 41
4.18 (upper) MSR eigenvalues for Camp Butner Cell 124, with one kind of 37-mm projectile at 8 cm below ground. (lower) MSR eigenvalues for Camp Butner Cell 192, which contained the other kind of 37-mm projectile, this one at a depth of 20 cm. 42
4.19 (upper) MSR eigenvalues for Camp Butner Cell 58, which contained two explosion byproducts, a fuze and a shrapnel fragment, at a depth of 16 cm. (lower) MSR eigenvalues for Camp Butner Cell 1728, which contained another fuze (buried 28 cm below ground). 43
4.20 MSR eigenvalues for Camp Butner Cell 14, with a sizable plowshare buried at 7 cm. 44

4.21 (upper) MSR eigenvalues for Camp Butner Cell 13, containing fragments of a 155-mm projectile, buried 50 cm below ground. (lower) MSR eigenvalues for Camp Butner Cell 45, containing several fragments, buried at several depths, of a munition that exploded. 45
4.22 ONVMS inversion of a measurement involving one large TOI 53
4.23 Two-target inversion with the ONVMS model 54
4.24 Robustness of ONVMS method 56
4.25 Inverted ONVMS amplitudes extracted from the Camp Butner TEMTADS measurements 58
4.26 ONVMS amplitudes (and representative photographs) of the smaller targets of interest in the Camp Butner test 59
4.27 Receiver operating characteristic curve for the ONVMS inversion protocol . . . 60
5.1 Blind inversion results from Dr. Shubitidze using the combined JD and ONVMS methods. All targets correctly identified and positions are within the size of the target. 62
5.2 MetalMapper test setup with one of three targets in one of five positions. Blind multitarget test data synthesized by superposing different data cases. 64
5.3 Results from using the multiple dipole Jacobian based gradient search method. Refer to Tables 9 and 10. 66
5.4 Polarizabilities extracted for blind case 9 using the Jacobian multiple dipole search method. Refer to Tables 9 and 10. 67
5.5 Inversion results from using the combined JD and ONVMS methods. Refer to Tables 9 and 10. 68
5.6 Results of 1-target and 3-target inversions 72
5.7 Actual Q_z EMI decay curves (dots) and constrained Pasion-Oldenburg fits (solid lines) for some of the targets of interest at Camp Butner. The vertical lines mark $t_{\max}$, the upper threshold of the fitting domain. 73
5.8 Clustering of the EMI features from a single-object inversion for Camp Butner . 76
5.9 Clusters used to train the first GMM classifier and the scoring results 77
5.10 Updated GMM classifier after confirming 118 UXO in the Camp Butner data . . 77
5.11 The 1-component GMM classifier applied to three object inversion 78
5.12 Final GMM classifier based on 3-object EMI inversion of Camp Butner data . . 79
5.13 ROC curve for Camp Butner live site classification 79
5.14 Camp Beale 2 2 MSR eigenvalues versus time for two-target cases involving ISO and 37-mm TOI. 84
5.15 Camp Beale 2 2 MRS data matrix eigenvalues versus time for a 60-mm, an 81-mm, and a sample of magnetic soil. 85
5.16 Left: Camp Beale 2 × 2 TEMTADS MSR data matrix eigenvalues versus time for Test Case 758. Right: Total ONVMS for the 3-cm fuze part from Test Case-758 extracted using a five-target inversion code. 86
5.17 (Left) Scatter plot of size (log10[Mzz(t1)]) and decay (log10[Mzz(t1)/Mzz(t80)]) parameters for all Camp Beale 2 × 2 TEMTADS anomalies based on the extracted total ONVMS. (Right) Result of the supervised clustering classification for the anomalies using the size and shape information in the panel at left. 86

5.18 Total ONVMS time-decay curves for the 105-mm, 81-mm, 60-mm and 37-mm TOI buried at Camp Beale and interrogated by the 2 × 2 TEMTADS array. . . . 87
5.19 Total ONVMS time-decay curves for the ISO targets and fuze parts at Camp Beale as determined starting from 2 × 2 TEMTADS data. 88
5.20 ROC curve for the Camp Beale 2 × 2 TEMTADS anomalies as identified by our procedure: (a) Taking the fuzes to be clutter; (b) Treating the fuzes as TOI. . . . 88
5.21 Time-dependent total ONVMS, inverted from MPV-II data, for the Camp Beale 105-mm, 81-mm, 60-mm 37-mm, and ISO munitions and for the fuze parts identified as potential TOI by ESTCP. 91
5.22 Images of seven small fuze parts that were identified as TOI by the ESTCP office. The bottom-right panel has the inverted total ONVMS for all these seven small fuze parts. 92
5.23 ROC curve for the Camp Beale MPV-II anomalies, (a) assuming the fuzes to be clutter and (b) considering them as TOI. 93
A.1 NSMC model comparison to library for blind test #3. 96
A.2 GEM-3 data acquired over 2 buried targets. 97
A.3 GEM-3 data inversion results from Partners poster 2006. 98
A.4 105mm UXO under clutter layer. 99
A.5 Dense clutter layer affixed to plywood substrate. 99
A.6 As the sensor is raised, the contribution of clutter to the overall EMI response is reduced compared to the response of the 105mm UXO. 100
A.7 Projected data as a function of elevation at the center of the measurement grid. . 101

List of Tables

1 Physical dimensions of steel and aluminum spheroids. PS ⇒ Prolate Spheroid. OS ⇒ Oblate Spheroid. 4
2 Physical dimensions of larger set of steel and aluminum spheroids fabricated in 2009-2010. First letter of designation is material (A=Aluminum, S=steel), second letter is shape (S=Sphere, P=Prolate, O=Oblate), and a number designation. 5
3 Inverted positions of single targets using data from the MPV instrument. The time signatures for the 81-mm and the BLU26 are shown in Figure 4.5. Positions are rounded to the closest integer. 16
4 Inversion results on two-target configurations from data collected by the MPV sensor. Positions are rounded to the closest integer. 17
5 True and inverted positions for nosepieces 22
6 True and inverted positions for halfrounds 23
7 True and inverted positions for three object configurations 25
8 Sample data cases from TEMTADS multiobject data set, January, 2010. 63
9 Original MetalMapper calibration data. 65
10 MetalMapper blind test data configurations synthesized by superposing data cases from Table 9. 66
11 Correct answers for the blind-test data runs. 95
12 NSMC model inversion results for position and orientation for blind test data. Numbers with an asterisk are arbitrary due to BOR considerations. 95

2 Objectives

The objectives of this project were to mitigate the effects of discrete metallic clutter from EMI data, and the simultaneous discrimination of multiple anomalies in close proximity with overlapping EMI responses. Specifically, we aimed to develop a robust approach for processing high quality data from next generation EMI instruments to mitigate the effects of clutter by isolating their EMI signatures after locating them individually, and then discriminate UXO from non-UXO targets at highly contaminated sites that include challenging terrain, vegetation, and geology using rigorous models that may include interaction effects. Specific objectives included:

1. Develop an N-target estimator, able to provide estimates of the number of targets present in the sensors field of view along with their locations and orientations, without resorting to computationally expensive optimizations. This locator will utilize high quality EMI data without solving the traditional ill-posed inverse scattering problem.

   Here, three approaches for this N-target locator will be reported (Sec. 4):

   (a) A multiple dipole search method based on a gradient search algorithm utilizing an analytical Jacobian (see Sec. 4.2)

   (b) A Joint Diagonalization (JD) method for quickly estimating the number of targets presented in the data (see Sec. 4.3)

   (c) A Orthonormalized Volume Magnetic Source (ONVMS) method (see Sec. 4.4)

2. Formulate robust classifiers that segregate N targets into UXO and non-UXO. This classifier will consider model based parameters such as volume estimates and HAP (H-magnetic field, A-Magnetic vector potential, P-magnetic scalar potential) estimate of polarizability and may be based on rapid statistical techniques such as Support Vector Machines (SVM).

   Significant progress on this has been made. For example, our group recently achieved a very encouraging score (no false negatives and very few false positives) on our dig list for the Camp Butner demonstration site using an Expectation Maximization (EM) algorithm (see [1]). In addition, our Camp Beale results were the best reported (see Sec. 5.5) for which we were awarded the SERDP Project of the Year (for MR-1672).

3. Discriminate UXO-like targets using rigorous (NSMS, SEA) models which explicitly include coupling between targets if required (see Sec. 4.2–Sec. 4.4).

Unmatched high quality data from advanced instruments such as the MetalMapper [2], the MPV2 [3], the TEMTADS [4], and the 2x2 TEMTADS [5] in the time domain were used used (Sec. 4.1). These instruments provide tremendous data diversity including vector data, monostatic and multistatic measurements, allowing us to assess the benefits of data diversity. As well, rigorous, physically complete models (see Sec. 4.2–Sec. 4.4) were developed to discriminate targets and anomalies based on their extracted EMI model parameters. These high fidelity models reduce to dipole models but can also provide much more information than traditional dipole models alone. The JD method, for example, trades knowledge of the target's **position** and what the **amplitude** of its polarizabilities are for a rapid determination of the **shape** of those polarizabilities.

3 Background

EMI data acquired over subsurface anomalies must be processed and inverted in order to discriminate innocuous scrap metal or geology from munitions and explosives of concern (MEC). At highly contaminated sites, processing data containing responses from disperse metallic clutter and overlapping anomalies is a difficult task both theoretically and computationally. Response from shallow yet small metallic clutter can often obscure deeper targets of interest (for example, see Figs. A.4–A.6), and the electromagnetic induction (EMI) response from targets in close proximity may affect each other due to mutual coupling [6, 7] and confuse or confound inversion schemes. These realities often lead to misclassification at best, or a complete failure of the routine at worst. Both outcomes raise the probability of false alarm and the probability of a missed MEC.

Prior approaches aimed at addressing the topic of discriminating multiple overlapping signals have serious limitations. Some studies cast the problem as a blind source separation (BSS) problem [8–10]. These studies assumed no interaction between anomalies which interaction is known to exist [11], were constrained to a maximum of two targets [8], were simulations that had prior knowledge of the target [9], or a combination of similar limitations. Other studies used data from multiple instruments (such as simultaneous EMI and GPR) which can be costly and is not generally available [12–15]. ESTCP project UX-0415 attempted to use a pair of dipoles to accommodate 2 targets and an iterative approach for isolating multiple dipole sources. However other work [16] has shown that even single multi-part UXO's require multiple dipoles for effective representation, and an optimization may not be able to distinguish a single heterogeneous UXO from multiple UXOs.

A recent SERDP project, MM-1637, *Selecting Optimal Models for Inverting EMI Data* concentrates on model selection and data quality to determine whether a given data set should be modeled as one or two targets. They then use a probability based inversion scheme to invert the data based on their assumed number of targets. Our approach differs from these approaches in fundamental ways. First, we are using analytical techniques to mitigate the noise due to disperse clutter which problem MM-1637 does not address. Second, we are developing methods to locate N targets simultaneously as a initial step either prior to or during inversion (Sec. 4) whereas MM-1637 only addresses the cases of one or two objects. This N-target locator (the JD method (see Sec. 4.4) and MUSIC target localizer [17] avoid time consuming and computationally complex inversion stages that MM-1637 does not avoid. Finally, we have access to the latest generation, well located instruments which provide high quality data from realistic field conditions.

In these studies, the objects are generally modeled using simple dipole models to accommodate two targets and the targets are isolated via a laborious time consuming inversion approach. Problems during the inversion phase also arise when the digital geophysical data are very low quality and simple phenomenological models fail to accurately represent overlapping EMI signals from anomalies in close proximity. In addition, many single heterogeneous targets may be well modeled by two dipoles, further complicating inversion processes based solely on dipoles. In these cases, the parameters of the phenomenological model (which are used as discrimination features in statistical decisions algorithms) become unseparable and as a result the classification is unreliable. Our approach detailed in Sec. 4.2 uses multiple dipoles seeded into the subsurface space, but uses the analytical Jacobian to simultaneously speed up the gradient search and provide higher confidence in the results.

As an example of EMI data with overlapping responses, Fig. A.2 in Appendix A.2 shows typ-

ical frequency domain data from a GEM-3 acquired over multiple buried targets [18]. Figure A.6 (top left subfigure) also show GEM-3 data from a 105mm UXO obfuscated by a layer of discrete clutter affixed to plywood. Even though we do not plan to use the GEM-3 for this research, evident in this data is the need for robust processing which identifies and classifies discrete anomalies and higher quality data addressing both positional and instrument noise.

The challenges involved with the discrimination of anomalies in close proximity are significant and persistent. In all prior cases, data quality in terms of the signal to noise ratio (SNR), positional inaccuracies, and data completeness (e.g. survey spacing), has been a significant factor which limits the success of the various models.

4 Materials and Methods

4.1 Canonical Targets

This project shares one early goal with two other projects (MR-1662 under SAIC, and MR-1669 under BAE) which started in the same FY as this MR-1664: to fabricate a set of canonical targets as a basis and baseline for measurements and testing. These targets have been fabricated and consist of two sets of spheroids and spheres combined together under the stewardship of Dan Steinhurst at NOVA Research: an old set made by Dr. Ben Barrowes while at MIT in 2003 and consists of smaller spheroidal and spherical targets under 25cm in the longest dimension (see Table 1 and Fig. 4.1), and a new set fabricated in 2009 and 2010 for these projects subcontracted through Delpsi, LLC (see Table 2). Figures 4.2–4.3 shows the spheroids from the second, larger set. Details on these targets are in Sec. 4.1. Data collected from the TEMTADS instrument over these canonical targets are summarized in Sec. 5.1 while data collected over multitarget UXO configurations with the MPV2 instrument in included in Sec. 5.3.

	comp.	type	axis ($2a$)	axis ($2b$)	nominal $e = b/a$
S1	Iron	sphere	90.62mm	90.62mm	1
S2	Steel	PS	30.02mm	182.19mm	6
S3	Steel	PS	29.94mm	90.28mm	3
S4	Steel	PS	14.97mm	90.76mm	6
S5	Steel	OS	29.32mm	4.56mm	1/6
S6	Steel	OS	29.59mm	9.65mm	1/3
S7	Steel	sphere	29.87mm	29.87mm	1
S8	Steel	OS	89.85mm	28.39mm	1/3
S9	Steel	OS	89.95mm	15.32mm	1/6
A1	Al	PS	30.17mm	180.23mm	6
A2	Al	PS	29.9mm	91.29mm	3
A3	Al	PS	15.04mm	91.14mm	6
A4	Al	OS	29.36mm	4.34mm	1/6
A5	Al	OS	29.36mm	8.88mm	1/3
A6	Al	sphere	29.91mm	29.91mm	1
A7	Al	OS	89.92mm	30.38mm	1/3
A8	Al	OS	89.98mm	15.94mm	1/6

Table 1: Physical dimensions of steel and aluminum spheroids. PS ⇒ Prolate Spheroid. OS ⇒ Oblate Spheroid.

Figure 4.1: Spheroid collection used for testing. Specifications are listed in Table 1.

	comp.	type	nominal axis ($2a$, cm)	nominal axis ($2b$, cm)	nominal $e = b/a$
SS1	steel	sphere	10	10	1
SS2	steel	sphere	15	15	1
SP1	steel	sphere	10	20	2
SP2	steel	prolate	6.67	20	3
SP3	steel	prolate	5	20	4
SP4	steel	prolate	4	20	5
SP5	steel	prolate	6	30	5
SP6	steel	prolate	12.5	50	4
SP7	steel	prolate	10	50	5
SP8	steel	prolate	10	30	3
SP9	steel	prolate	15	30	2
SP10	steel	prolate	7.5	30	4
SO1	steel	oblate	20	8	2/5
SO2	steel	oblate	20	4	1/5
SO3	steel	oblate	20	2.67	1/7.5
SO4	steel	oblate	20	2	1/10
AS1	aluminum	sphere	10	10	1
AS2	aluminum	sphere	15	15	1
AP1	aluminum	sphere	10	20	2
AP2	aluminum	prolate	6.67	20	3
AP3	aluminum	prolate	5	20	4
AP4	aluminum	prolate	4	20	5
AP5	aluminum	prolate	6	30	5
AP6	aluminum	prolate	12.5	50	4
AP7	aluminum	prolate	10	50	5
AP8	aluminum	prolate	10	30	3
AP9	aluminum	prolate	15	30	2
AP10	aluminum	prolate	7.5	30	4
AO1	aluminum	oblate	20	8	2/5
AO2	aluminum	oblate	20	4	1/5
AO3	aluminum	oblate	20	2.67	1/7.5
AO4	aluminum	oblate	20	2	1/10

Table 2: Physical dimensions of larger set of steel and aluminum spheroids fabricated in 2009-2010. First letter of designation is material (A=Aluminum, S=steel), second letter is shape (S=Sphere, P=Prolate, O=Oblate), and a number designation.

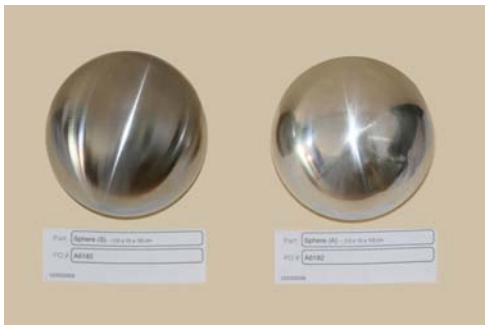

(a) SS1 and AS1

(b) SS2 and AS

(c) SP1 and AP1

(d) SP2 and AP2

(e) SP3

(f) SP4 and AP4

(g) SP5 and AP5

(h) SP6

Figure 4.2: Larger steel spheroids SS1-SP6. Specifications are listed in Table 2.

(a) SP7

(b) SP8

(c) SP9

(d) SP10

(e) SO1 and AO1

(f) SO2 and AO2

(g) SO3

(h) SO4

Figure 4.3: Larger steel spheroids SP7-SO4. Specifications are listed in Table 2.

4.2 Multiple Dipole Inversion Using Jacobian Gradient Search

The simultaneous detection and identification of multiple targets using electromagnetic induction time-domain sensors remains a challenge due to the fast decay of the magnetic field with sensor-target distance. For example, the signal from a weak yet shallow target or clutter item can overshadow that from a much larger yet deeper UXO, potentially resulting in erroneous localization and/or identification. We propose in this paper a method based on the Gauss-Newton algorithm for the inversion of multiple targets within the field of view of sensors operating at electromagnetic induction – EMI – frequencies (tens of Hertz to a few hundred kHz). In order to minimize the number of unknowns to invert for, the polarizability tensor is written as a time-independent orientation matrix multiplied by a time-dependent diagonal intrinsic polarizability tensor. Similarly, position is assumed to be time independent so that both position and orientation angles are inverted only once using all time channels collected by the instrument. Moreover, using the dipole approximation, we are able to compute the Jacobian in closed form for instruments with either square or circular primary field coils, thus contributing to the speed of the algorithm. Validating results are shown based on measurement data collected with two EMI sensors on various types of UXO.

4.2.a Introduction

Numerous military campaigns and warfare practice over the last decades have left millions of acres of land contaminated worldwide with unexploded ordnance (UXO), projectiles with explosive cores and metallic shells that did not explode upon impact and penetrated into the ground. The cleaning of these fields is currently a daunting and hugely expensive task that consumes a budget of several hundred million dollars per year in the United States alone. Such prohibitively large cost is due to a very large false-alarm rate associated with the detection of UXO with current remote sensing technologies. Differentiating between unexploded and exploded ordnance is a technological challenge that is yet to be overcome in realistic field situations, where clutter and/or geological factors can significantly jam the signals used by remote sensing algorithms. As a result, current cleaning campaigns are based on overly simple metal detection schemes with little discrimination involved, yielding hugely time consuming and expensive campaigns which result most of the time in the excavation of harmless objects.

In parallel, researchers have spent decades investigating technologies and refining algorithms to detect and discriminate metallic subsurface objects better. For example radar sensors operating in the microwave regime, which have been so successful when pointing to the sky, have been turned upside down to send and receive signals into and from the ground. Advanced signal processing techniques have proven the usefulness of this approach [19, 20], but also revealed its limitations due to the variations in soil surfaces and volume compositions which quickly obscure the signatures of the subsurface targets. As an alternative, electromagnetic induction (EMI) which utilizes magnetic fields at much lower frequencies (from tens of Hertz to a few hundred kHz) has proven remarkably robust. The associated magneto-quasistatic regime ensures that displacement currents are negligible compared to conduction currents in the metallic targets. The soil, assumed here to be non-magnetic and non-conductive, is transparent so that the UXO can be simply considered in free space. Various models have been proposed, from the simple but effective dipole model [21–24], to more elaborated theoretical studies on canonical shapes [25–27] as well as more flexible numerical models [28, 29]. The purpose of these various techniques is to improve the discrimination

capabilities of UXO in realistic environments [30–33].

A major drawback of the EMI regime, however, is its sharp field decay (approximately as $1/r^3$ at large distances compared to the primary coil size, with r being the target-sensor distance) which makes it difficult to use EMI frequencies at ranges beyond a few times the size of the coils or when identifying multiple UXO in close proximity to one another as well as in close proximity to large clutter items. For example, even a small but shallow metal object can overshadow the signal of a deeper UXO producing an erroneous classification. A related problem occurs when targets of similar sizes are buried alongside one another at comparable depths [10]. In both situations, the detection and identification can be considerably improved by considering a multi-target configuration, whereby multiple time signatures are simultaneously inverted for and used in the decision scheme. One of the first attempts along this direction collaboratively used EMI and radar signals [12, 13]. This approach, however, revealed to be both time consuming and costly due to the combination of two sets of hardware and two analysis algorithms involved. Other attempts concentrated on using only EMI data with signal processing techniques for sources separation [8]. Successful results were reported on synthetic data (i.e. computer generated) while more validation is expected using real UXO and EMI sensors. Similarly, an independent component analysis revealed the possibility of extracting the signature of a UXO in the presence of multiple clutter items, but the method concentrated on the specific situation of known UXO, i.e. a known signature which had to be extracted from a sum of multiple signatures [34]. More recently, positions, orientations, and time dependent polarizabilities were inverted on two-target configurations from both synthetic as well as sensor data [35]. The method, based on a multi-start search and separation of the linear and nonlinear parameters, was shown to yield good agreement with ground truth. However, as the authors point out, the strong nonlinearity of the problem required a good initial guess, which was provided by sampling a region of interest. This requirement could be alleviated by using a multiple signal classification approach [36, 37] for position estimation (nonlinear part) followed by a direct solution of the polarizabilities (linear part) using either a least square method [38], a Kalman filter approach [39], or other. Yet, this approach presents some limitation when monostatic data are used in the inversion process.

Trying to alleviate some of these pitfalls, we propose in this paper an algorithm significantly improved compared to our previous work [40]: factorization of the orientation angles from the time dependent unknown vector, incremental step size in the Gauss-Newton algorithm, analytical computation of the Jacobian matrix for square and circular primary field coils, and solution selection. The resulting new algorithm shows robustness to initial conditions that removes the need of user defined regions of interest, numerical stability that reduces the number of realizations necessary to filter out local minima solutions, and computational speed. The method is here extensively validated using measured data from two types of EMI sensors (MPV and TEMTADS) on a variety of UXO.

4.2.b Problem configuration and EMI sensors

We consider the problem illustrated in Figure 4.4, whereby a sensor at position $\bar{r}_s$ illuminates multiple targets described by their positions $\bar{r}_\ell = \hat{x}x_\ell + \hat{y}y_\ell + \hat{z}z_\ell$, elevations θ_ℓ and azimuths ϕ_ℓ where $\ell = 1,\ldots,N$ ($N = 3$ is shown in the figure). We suppose all N targets to be bodies of revolution, modeled as a three-axis dipole with parameters $\bar{r}_\ell$, θ_ℓ, ϕ_ℓ and intrinsic polarizabilities $\overline{\overline{\beta}}_\ell$ (see subsequent Eq. (4.2.5c)). The transmitter and receiver sensors are incorporated into our

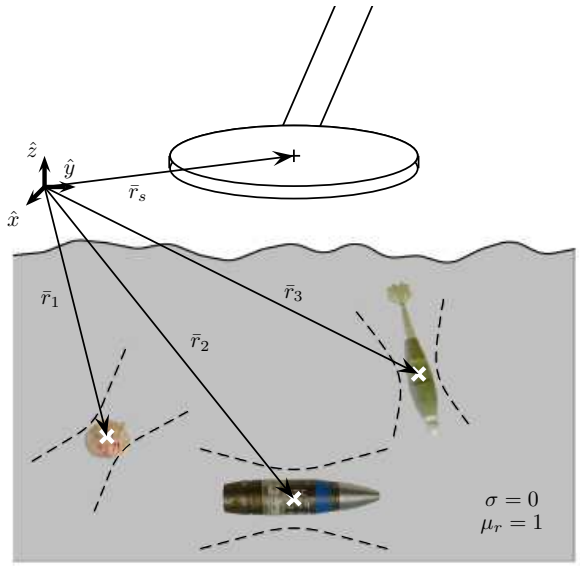

Figure 4.4: Problem configuration: an EMI sensor surveys an area where N targets are buried ($N = 3$ in the figure). The unknowns of the problem are the targets (intrinsic) polarizabilities themselves as well as their positions $\bar{r}_\ell$ and orientations (θ_ℓ, ϕ_ℓ). The soil is supposed to be non-conductive ($\sigma = 0$) and non-permeable ($\mu_r = 1$).

algorithm to closely model the hardware configuration of either the TEMTADS [41, 42] or the MPV [43] instruments. receiver sensors separated by 40 cm (center to center) in the (xy) plane and collecting z components of the secondary magnetic field induced by the target. Each sensor is composed of a square transmitting coil (side dimension: 35 cm) and a co-centered square receiving coil (side dimension: 25 cm) which are time decoupled: during the first half of the cycle, the transmitting coils emits a primary field which excites all metals in its vicinity whereas during the second half of the cycle, the receiving coil measures the derivative of the flux generated by all ringing metals. The hardware electronics integrates the flux to yield a quantity proportional to the magnetic field which is measured typically after the first 100 μs to let the instrument transients die away. The targets themselves typically ring for many milliseconds so that measurements are gathered until about 25 ms logarithmically sampled in 120 time channels. Measurements can be performed in either a monostatic mode, in which case all the 25 sensors sequentially transmit and receive yielding 25 data points, or in a bistatic mode in which case each transmitter fires sequentially and measurements are gathered by all 25 receivers yielding 625 data points. We model the transmitters as square current loops whose primary field can be written as the addition of four sections of straight wire which all carry a unit constant current. The primary field from each wire is given by

$$\bar{H}^{\text{wire}} = \frac{\hat{s}}{4\pi|\bar{s}|}(\hat{r}_1 - \hat{r}_2)\cdot\hat{r}_{12} \tag{4.2.1}$$

where a hat denotes a unit vector and a bar denotes a regular vector, $\hat{r}_1$ and $\hat{r}_2$ are the unitary vectors between each extremities of the straight wires and the observation point, $\bar{r}_{12} = \bar{r}_2 - \bar{r}_1$, and $\bar{s} = \hat{r}_{12} \times \bar{r}_1$. The received signal at each receiver is simply computed by integrating the secondary

magnetic field over the surface of the corresponding receiving square coil.

The MPV (Man Portable Vector) [43] sensor is very different from the TEMTADS in that it is much smaller and lighter. It uses a pair of coaxial circular transmitting coils (of radius 37.5 cm and vertical separation 15.6 cm) and a series of five square receiving coils (of side dimensions 10 cm) which can measure all components of the secondary field. The primary field is modeled as that produced by a circular current loop of radius a and unit current. In the cylindrical coordinate system, the field at (ρ, z) is written as [22, 44]:

$$H_\rho(\rho,z) = \frac{1}{2\pi}\frac{1}{\sqrt{(a+\rho)^2+z^2}}\frac{z}{\rho}\left[\frac{a^2+\rho^2+z^2}{(\rho-a)^2+z^2}E(k)-K(k)\right], \tag{4.2.2a}$$

$$H_z(\rho,z) = \frac{1}{2\pi}\frac{1}{\sqrt{(a+\rho)^2+z^2}}\left[\frac{a^2-\rho^2-z^2}{(\rho-a)^2+z^2}E(k)+K(k)\right], \tag{4.2.2b}$$

where $K(k)$ and $E(k)$ are the elliptic integrals of the first and second kind, respectively, with $k^2 = 4a\rho/\left[(\rho+a)^2+z^2\right]$. The received signal is computed by integrating the secondary magnetic field over the surface of the receiving perpendicular square coils. Like for the TEMTADS, measurements are gathered during off-time cycles (when the primary field is turned off), between about 0.4 ms and 23 ms sampled in 30 time channels. Inherent to its construction, the operating mode of the MPV is a mixture of monostatic and bistatic mode, typically coined multi-static (the receivers are tied to the transmitter but not collocated). Advantages compared to the TEMTADS are its vectorial property and its maneuverability in complex terrain whereas its disadvantages are its smaller field of view and the necessity of tracking its position and orientation during data acquisition.

4.2.c Data analysis

The fast field decay in the EMI regime ensures that near field effects are confined to a very small volume surrounding the buried target. As a consequence, the secondary field at the sensor location is almost identical to that of a triaxial dipole, for which the magnetic field $\bar{H}$ is given by [22]:

$$\bar{H}(\bar{r}_s) = \frac{1}{4\pi r_{ts}^3}\left[\frac{3\bar{r}_{ts}(\bar{r}_{ts}\cdot\bar{m})}{r_{ts}^2}-\bar{m}\right] \tag{4.2.3}$$

where $\bar{m} = \hat{x}m_x + \hat{y}m_y + \hat{z}m_z$ is the dipole moment of the target, $\bar{r}_t$ is the target location, $\bar{r}_s$ is the sensor location, $\bar{r}_{ts} = \bar{r}_s - \bar{r}_t$ and $r_{ts} = ||\bar{r}_{ts}||$. It should be mentioned that the dipole analysis remains an approximation which has proven accurate in the overwhelming majority of UXO configurations. However, its limitation is particularly obvious with heterogeneous targets or when multiple targets are in very close proximity to one another, typically within a sub-centimeter distance, with one or both targets being ferrous [45]. In this situation, coupling between eddy currents of the two objects can happen at a level sufficient to alter the secondary magnetic field at the receiver location [46]. Such configuration is, however, more theoretical than practical and to our knowledge, has not been encountered beyond laboratory tests. As a consequence, we suppose here that the separation between the targets is sufficient to ensure that the various UXO respond as independent dipoles with no coupling effects [47]. Within such independent scattering approximation, the magnetic field of N targets located at $\bar{r}_\ell$ ($\ell = 1,\ldots,N$) and with dipole moments $\bar{m}_\ell$ is simply obtained as the

algebraic sum of Eq. (4.2.3):

$$\bar{H}(\bar{r}_s) = \sum_{\ell=1}^{N} \frac{1}{4\pi r_{\ell s}^3} \left[\frac{3\bar{r}_{\ell s}(\bar{r}_{\ell s} \cdot \bar{m}_\ell)}{r_{\ell s}^2} - \bar{m}_\ell \right] . \tag{4.2.4}$$

Note that we assume N to be known in Eq. (4.2.4), which is an assumption further discussed in Section 4.2.e. The dipole moment $\bar{m}_\ell$ is obtained from the self-polarizability $\overline{\overline{\beta}}_\ell$ of the target along three directions, weighted by the primary field at the target location. If, in addition, the target is rotated with respect to the global reference frame, the rotation angles need to be incorporated. Restricting ourselves to bodies of revolution as most UXO are, the dipole moment $\bar{m}_\ell$ can be written as

$$\bar{m}_\ell = \overline{\overline{\Lambda}}_\ell^T \cdot \overline{\overline{\beta}}_\ell \cdot \overline{\overline{\Lambda}}_\ell \cdot \bar{H}^{pr}(\bar{r}_\ell) \tag{4.2.5a}$$

where

$$\overline{\overline{\Lambda}}_\ell = \begin{pmatrix} \cos\theta_\ell \cos\phi_\ell & \cos\theta_\ell \sin\phi_\ell & -\sin\theta_\ell \\ -\sin\phi_\ell & \cos\phi_\ell & 0 \\ \sin\theta_\ell \cos\phi_\ell & \sin\theta_\ell \sin\phi_\ell & \cos\theta_\ell \end{pmatrix} \tag{4.2.5b}$$

is the rotation matrix with the angles θ_ℓ and ϕ_ℓ,

$$\overline{\overline{\beta}}_\ell = \begin{pmatrix} \beta_{x_\ell} & 0 & 0 \\ 0 & \beta_{y_\ell} & 0 \\ 0 & 0 & \beta_{z_\ell} \end{pmatrix} , \tag{4.2.5c}$$

where $(\beta_{x_\ell}, \beta_{y_\ell}, \beta_{z_\ell})$ are the time-dependent polarizabilities along the three directions of the reference frame local to the target, and $\bar{H}^{pr}(\bar{r}_\ell)$ is the primary field at the target location. Note that two components of $\overline{\overline{\beta}}_\ell$ are expected to be identical due to the BOR assumption, even though this property is not enforced in Eq. (4.2.5c). For example, in a bistatic configuration, the transmitter remains at a unique location while the receiver spans a series of measurement points. As a consequence, the primary field $\bar{H}^{pr}(\bar{r}_\ell)$ is unique and so is $\bar{m}_\ell$. In a monostatic configuration, however, where the transmitter and receivers are collocated and span together the measurement points, $\bar{H}^{pr}(\bar{r}_\ell)$ varies from point to point, and so does $\bar{m}_\ell$. The polarizability tensor $\overline{\overline{\beta}}_\ell$, however, is invariant and can be used by a classifier for each target.

Our inversion algorithm is based on a Gauss-Newton solution of the normal equation assuming N targets present in the field of view of the sensor. The simultaneous inversion of the time-independent position, orientation, and time-dependent polarizabilities of the targets is expressed as a least-squares minimization between the measured field and the predicted field computed from Eq. (4.2.4). Hence, the unknown vector is written as

$$\mathbf{x} = [\mathbf{a}_1 \ldots \mathbf{a}_\ell \ldots \mathbf{a}_N \, \mathbf{b}_1 \ldots \mathbf{b}_\ell \ldots \mathbf{b}_N]^T , \tag{4.2.6a}$$

$$\mathbf{a}_\ell = [x_\ell \, y_\ell \, z_\ell \, \theta_\ell \, \phi_\ell]^T , \tag{4.2.6b}$$

$$\mathbf{b}_\ell = [\beta_{x_\ell}^{t_1} \, \beta_{y_\ell}^{t_1} \, \beta_{z_\ell}^{t_1} \, \ldots \beta_{x_\ell}^{t_{N_{tc}}} \, \beta_{y_\ell}^{t_{N_{tc}}} \, \beta_{z_\ell}^{t_{N_{tc}}}]^T , \tag{4.2.6c}$$

where t_j $(j = 1, \ldots, N_{tc})$ denotes the time channels and where the subscript 'T' denotes the transpose. Eq. (4.2.6c) indicates that the algorithm solves for a single position and a single orientation

per target, with multiple polarizabilities across the time history of the transmitter for all targets simultaneously. Note that it is also possible to invert for a more general polarizability tensor with six independent elements [35, 48, 49]. Although such approach has been shown to be valid and accurate, it is not adopted here: inverting a full tensor at each time channel is analogous to inverting for the rotation angles at each time channel. Within a good approximation, however, these angles can be considered time independent so that we factor them out of the polarizability tensor and included them in the time independent part of the minimization vector, thus drastically reducing the number of unknowns to invert for. Note that similarly, the algorithm inverts for a unique position rather than a time-dependent position at every time channel. Considering the position and angles to be time independent is an approximation justified in practice. Indeed, although various parts of the UXO may respond differently in time, effectively yielding slightly different positions and orientations of the tri-axial dipole used to best match the measured secondary field, we have found this effect to be small in the cases considered in this paper: inverting the positions at every time channels yields similar estimates except at later times when the field values reach the noise level (data not shown).

The task of the minimization algorithm is to estimate the unknown parameter $\mathbf{x}$ so as to minimize the sum of squares

$$\min_{\mathbf{x}} S = \min_{\mathbf{x}} \left(\Delta\bar{H}_z^T \, \Delta\bar{H}_z\right) \tag{4.2.7}$$

where $\Delta\bar{H}_z = (\bar{H}_z^{\text{mea}} - \bar{H}_z)$ with $\bar{H}_z^{\text{mea}}$ and $\bar{H}_z$ being the measured and computed z components of the magnetic field, respectively. If needed, the addition of other components of the magnetic field to the minimization problem is straightforward (e.g. the TEMTADS measures only H_z whereas the MPV measures all three components). The corresponding normal equation is written as

$$\bar{\bar{J}}_z^{\,T} \bar{\bar{J}}_z \cdot \Delta\mathbf{x} = \bar{\bar{J}}_z^{\,T} \cdot \Delta\bar{H}_z \tag{4.2.8}$$

where $\Delta\mathbf{x} = \mathbf{x}^{i+1} - \mathbf{x}^i$ is the unknown vector which provides the updated quantities of $\mathbf{x}$ at each iteration, i is the iteration number, $\bar{\bar{J}}_z$ is the Jacobian matrix. The Gauss-Newton update equation is therefore

$$\mathbf{x}^{i+1} = \mathbf{x}^i + \Delta\mathbf{x} = \mathbf{x}^i + \left(\bar{\bar{J}}_z^{\,T} \bar{\bar{J}}_z\right)^{-1} \bar{\bar{J}}_z^{\,T} \cdot \left(\bar{H}_z^{\text{mea}} - \bar{H}_z\right) \tag{4.2.9}$$

The vector notation used on $\bar{H}_z^{\text{mea}}$ and $\bar{H}_z$ refers to the fact that the magnetic field is measured and computed over a series of K observation points. The Jacobian matrix is therefore a block matrix of size $[N_{tc} \times K, N(5+3N_{tc})]$ where N_{tc} is the number of time channels. Splitting the Jacobian matrix into time independent and time dependent parts, we write:

$$\bar{\bar{J}}_z = \left[\bar{\bar{A}}_z \, , \, \bar{\bar{B}}_z\right] \tag{4.2.10}$$

where $\bar{\bar{A}}_z$, of size $[N_{tc} \times K, 5N]$, gathers the derivatives of the computed $\bar{H}_z$ field with respect to the three positions and two angles across all observation points and time channels. Assuming $N = 1$

for the sake of simplicity of notation in this example:

$$\overline{\overline{A}}_z = \begin{pmatrix} \overline{\overline{A}}_z^{t_1} \\ \vdots \\ \overline{\overline{A}}_z^{t_j} \\ \vdots \\ \overline{\overline{A}}_z^{t_{N_{tc}}} \end{pmatrix} \text{ with } \overline{\overline{A}}_z^{t_j} = \begin{pmatrix} \bar{A}_{z_1}^{t_j} \\ \vdots \\ \bar{A}_{z_\ell}^{t_j} \\ \vdots \\ \bar{A}_{z_K}^{t_j} \end{pmatrix} \tag{4.2.11a}$$

and

$$\bar{A}_{z_\ell}^{t_j} = \left[\frac{\partial}{\partial x_\ell} \; \frac{\partial}{\partial y_\ell} \; \frac{\partial}{\partial z_\ell} \; \frac{\partial}{\partial \theta_\ell} \; \frac{\partial}{\partial \phi_\ell} \right] H_z^{t_j}(\bar{r}_\ell) \tag{4.2.11b}$$

where $H_z^{t_j}(\bar{r}_\ell)$ is the z component of the magnetic field obtained from Eqs. (4.2.4) and (4.2.5) at time channel t_j. The matrix $\overline{\overline{B}}_z$ is a block diagonal matrix where each block has a size $[N_{tc} \times K, 3N_{tc}]$ (still under the assumption of $N = 1$) and gathers the derivatives of the computed $\bar{H}_z$ field with respect to the three polarizabilities:

$$\overline{\overline{B}}_z = \text{diag}[\overline{\overline{B}}_z^{t_1}, \ldots, \overline{\overline{B}}_z^{t_j}, \ldots, \overline{\overline{B}}_z^{t_{N_{tc}}}] \text{ with } \overline{\overline{B}}_z^{t_j} = \begin{pmatrix} \bar{B}_{z_1}^{t_j} \\ \vdots \\ \bar{B}_{z_\ell}^{t_j} \\ \vdots \\ \bar{B}_{z_K}^{t_j} \end{pmatrix} \tag{4.2.12a}$$

and

$$\bar{B}_{z_\ell}^{t_j} = \left[\frac{\partial}{\partial \beta_{x_\ell}} \; \frac{\partial}{\partial \beta_{y_\ell}} \; \frac{\partial}{\partial \beta_{z_\ell}} \right] H_z^{t_j}(\bar{r}_\ell) \tag{4.2.12b}$$

The formulation outlined above is straightforward to generalize to the case of $N > 1$ as well as when all components of the magnetic field are known (for example if the MPV sensor is used) by simply stacking the Jacobian matrices and right-hand side vectors corresponding to other components, and generalizing the unknown vector $\mathbf{x}$. Note that all the derivatives are straightforward to compute except those with respect to position since they require the derivative of the primary field as well, in view of Eq. (4.2.5a). This task can still be performed analytically for both the TEM-TADS and MPV sensors using Eqs. (4.2.1) and (4.2.2) and a precise knowledge of the sensors' geometries, which contributes to the computational efficiency of the algorithm.

The actual implementation of Eq. (4.2.9) is slightly modified by the addition of a weighting factor $\alpha \leq 1$ in order to control the step size:

$$\mathbf{x}^{i+1} = \mathbf{x}^i + \alpha \left(\overline{\overline{J}}_z^{\,T} \overline{\overline{J}}_z \right)^{-1} \overline{\overline{J}}_z^{\,T} \cdot \left(\bar{H}_z^{\text{mea}} - \bar{H}_z \right) \tag{4.2.13}$$

Empirical investigations revealed an increasing importance of α as the number of targets to invert for increased: from practically unnecessary for $N = 1$ to important for $N \geq 3$. While further analytical investigations might be necessary to determine the optimal α for each configurations, results reported hereafter have been obtained with $\alpha = 0.5$, which appears to offer a good compromise between accuracy and convergence speed.

4.2.d Inversion results

Despite an extensive validation campaign on synthetic data, we concentrate and only present here results from data that have been acquired by real sensors on real UXO. Data have been collected using both the TEMTADS [50] and MPV instruments [51] and the inversion results are presented in the following two sections on various multi-target configurations. It is important to keep in mind that measurements are performed on real UXO which therefore have certain physical dimensions, whereas the algorithm is inverting for one tri-axial dipole per UXO. The location of these equivalent dipoles is not precisely defined: it is close to the center of the target if the latter is buried horizontally (i.e. parallel to the sensor), whereas it migrates toward the tip for vertical targets where one extremity is closer to the sensor than the other. The positions also depend on the composition, geometry, and external features of each target such as fins, conductive rings, etc. The exact location at which a single tri-axial dipole should be located in order to best reproduce the secondary field of a given UXO is therefore not expected to match exactly the positions recorded at the data acquisition stage (which correspond typically to the exact center or exact tip of the UXO). The accuracy of the subsequent results should be judged with these considerations in mind.

4.2.d.(1) MPV data The MPV is a vectorial multi-static EMI instrument which collects data as it is waved above the surface. Due to its intrinsic portable nature, the trajectory of the MPV as well as its orientation (e.g. pitch, roll, and yaw) need to be tracked during the entire data acquisition time. The data set thus collected is then converted into components of the magnetic field along three pre-defined directions, and subsequently processed by our algorithm. The results reported hereafter have been obtained using the vectorial information of all five sensors, even though more in depth studies showed that not all carry a critical information necessary for proper inversion (data not shown).

A first series of validating tests of our MPV model was performed on single targets and yielded good results in all the cases considered for both the positions, orientations, and time dependent polarizabilities. Table 3 lists a few cases with the corresponding inverted positions and orientations which show a reasonable agreement with the ground truth. We recall here that the ground truth values typically correspond to distances to the center of the UXO, which might be a few centimeters deeper from the optimized location of an equivalent dipole (nearer to the sensor). For example, the elevation of the 60-mm UXO was set to $\theta = 270$ degrees, which corresponds to the target being horizontal. The exact location of the principal responding magnetic dipole of the target may not correspond to the geometrical center of the actual target. Therefore, a first order correction to the inverted depth for this case to account for the radius of the target, i.e. 30 mm, augments the inverted depth from 48 cm to 51 cm, in good agreement with the ground truth. Corrections to other targets are not as straightforward to incorporate because of the non-trivial elevation angles. The largest deviation in depth amounts to 10 cm and occurs with the 105-mm with $\theta = -19$ degrees. The small elevation indicates that the target is close to vertical so that an important deviation between the center position and the location of the equivalent dipole is expected, especially because this target is very long. In addition to the mismatch between the center of the target and the location of its equivalent dipole, part of the discrepancies in Table 3 can also be attributed to measurement and instrument noise while yet another part could be due to algorithmic inaccuracies (for example due to a too small data set to optimize the unknown vector to a desired level of accuracy). The overall good results, however, suggest that the algorithm is effective at inverting MPV data. This

Target	Length [mm]	Ground truth [cm] x	y	z	[degrees] θ	ϕ	Inverted results [cm] x	y	z	[degrees] θ	ϕ
Al sphere		0	22	26	-	-	0	22	29	-	-
Brass sphere		0	22	26	-	-	0	22	28	-	-
Steel sphere		0	22	26	-	-	0	22	28	-	-
81-mm	490	-23	22	52	-18	0	-14	22	50	-20	-10
105-mm	642	-20	22	63	-19	180	-12	23	50	-30	176
BLU26	70.31	0	22	38	0	0	0	22	34	-	-
57-mm	170.47	5	22	55	307	180	4	22	51	310	160
60-mm	245	0	22	51	270	0	0	22	48	260	7

Table 3: Inverted positions of single targets using data from the MPV instrument. The time signatures for the 81-mm and the BLU26 are shown in Figure 4.5. Positions are rounded to the closest integer.

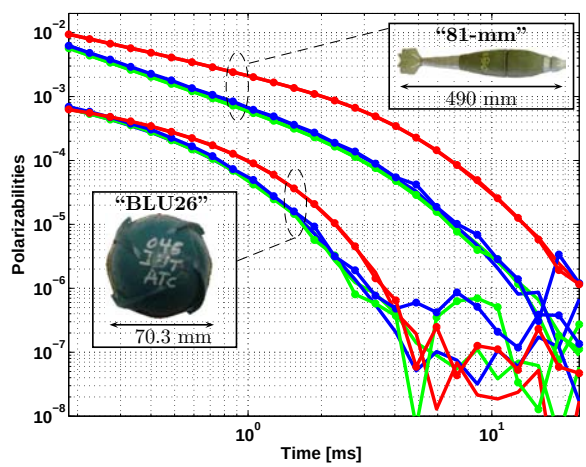

Figure 4.5: Time domain polarizabilities for two types of UXO (81-mm and BLU26) measured and inverted separately from MPV data.

conclusion is also supported by the time dependent polarizabilities obtained for these cases, a subset of which is shown in Figure 4.5. As expected, the 81-mm UXO shows one polarizability element consistently stronger than the other two which are almost identical and reveal a geometric azimuthal symmetry. The BLU26 exhibits similar characteristics but the three polarizabilities are closer to each other due to the close to spherical shape of this UXO (see inset).

Two-target results present mitigated yet consistent results within the data set available to us.Two configurations were analyzed: that of two 40-mm UXO at the same depth, and that of a 40-mm along with 81-mm UXO at varying depths, both cases for different lateral separations. Inverted positions, summarized in Table 4, indicated a good performance when the targets are at the same depth, with yet improved accuracy for larger lateral separations as intuitively expected. This is evident from the inverted polarizabilities of the two 40-mm targets, shown in Figure 6(a): while

UXO	Truth [cm]						Inverted [cm]					
	x_1	y_1	z_1	x_2	y_2	z_2	x_1	y_1	z_1	x_2	y_2	z_2
40-mm & 40-mm	0	0	40	25	0	40	2	−1	40	23	0	38
40-mm & 40-mm	0	0	40	40	0	40	1	−1	39	40	−2	39
81-mm & 40-mm	0	0	40	25	0	40	0	0	42	18	0	40
81-mm & 40-mm	0	0	65	25	0	40	0	0	43	22	0	38

Table 4: Inversion results on two-target configurations from data collected by the MPV sensor. Positions are rounded to the closest integer.

the four strong components (two targets in two configurations) are almost identical in both cases, one of the weak components is slightly under-estimated for dx=25 cm (circle marks). The good performance at identical depth is somewhat maintained with the two different targets, despite a small error in the inverted lateral separation which can be mostly attributed to the physical width of the targets. Incorporating this correction of about 6 cm, the inverted separation would be about 21 cm instead of the measured 25 cm. The overall results worsen, however, when the two targets are at different depths, with z_2 in Table 4 often under-estimated. The polarizabilities, shown in Figure 6(b) reflect this behavior: while the larger target is consistently well predicted, the weaker one is better predicted at similar depth (see the dipping weak component for dz=25 cm, indicating a sign change and thus a weak corresponding component of the secondary magnetic field).

In depth investigations of these cases suggested that the data set itself might not be totally consistent from grid point to grid point, but contains variations that are likely at the origin of some of the errors in the inversion results. As a matter of fact, although the natural operating mode of the MPV is to be waved above the targets, data provided to us has been collected in an inverted configuration, whereby the MPV was held fixed and the targets were moved on a 5×5 square grid with 20 cm separation between adjacent points. Repeatability between grid point therefore cannot be guaranteed since the two targets can easily move with respect to each other, either in distance or in orientation. Since our algorithm assumes an invariant configuration from grid point to grid point (akin to when the targets are buried), these errors would induce inversion inaccuracies. Yet, the overall good agreement between the inverted results and reported ground truth confirm the possibility of using the MPV for the detection and classification of multi-targets.

4.2.d.(2) TEMTADS data measurement campaign using the TEMTADS sensor has been undertaken by the Naval Research Laboratory on one, two, as well as three-target configurations. The targets of interest were a 4.2-inch mortar, a nose cone, and a baseplate whose time dependent polarizabilities are represented in Figure 4.7 when they are inverted as separate targets. Like the 81-mm previously, the mortar exhibits a typical signature of a UXO, whereby one polarizability dominates the other two which are almost identical, indicating that the target is a body of revolution with a preferential direction. The nose cone produces a signal that is about two orders of magnitude inferior to the mortar, with a mostly log-log linear time decay indicating a strong ferrous component. In addition, the three polarizabilities are comparable which suggests a somewhat homogeneous shape in three directions, akin to a sphere. The baseplate produces a signal of comparable magnitude to the mortar with the strongest dipole switching in time from the $\hat{x}$ direction

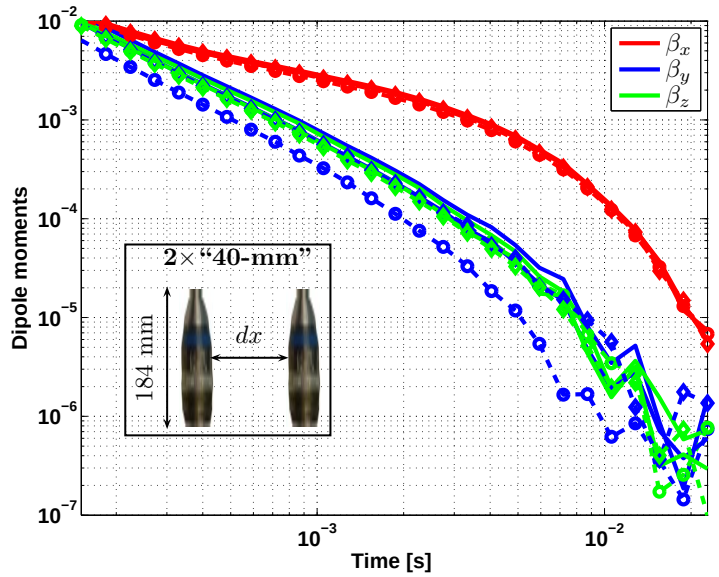

(a) Two 40-mm UXO inverted in two configurations: (dx,dz)=(25,0) and (40,0) cm. The visibly weaker components (circle marks) corresponds to dx=25 cm.

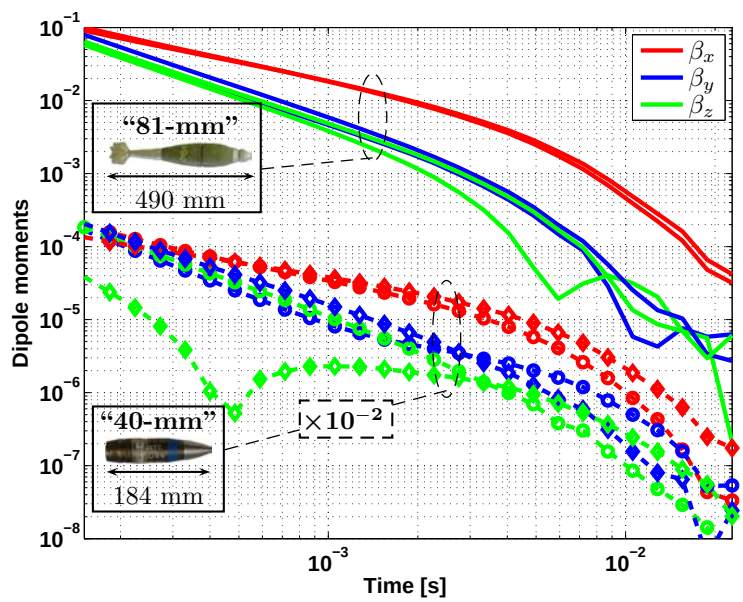

(b) 81-mm and 40-mm UXO inverted in two configurations: (dx,dz)=(25,0) and (25,25) cm. The weaker and dipping component (diamond marks) corresponds to dz=25 cm.

Figure 4.6: Time domain polarizabilities for two two-target configurations measured by the MPV. Inverted positions are summarized in Table 4.

to the $\hat{z}$ direction. These signatures have been obtained using the method presented in the previous section and have been independently validated [52, 53]. The inverted positions, listed in the captions of Figure 4.7, match the true values with a centimeter accuracy and validate our algorithm as well as the associated TEMTADS model in the case of single targets. We emphasize also the fact that the inverted angles are typically within a few degrees of their expected values.

Two-target configurations consisted of combining the mortar with one of the other two targets and varying their respective lateral distances while keeping their depths constant. The lateral distances were varied from $x = 0$ cm to $x = 100$ cm at 10 cm intervals (yielding 11 configurations). At $x = 0$ the targets are immediately on top of each other, which is known to be a challenging configuration to invert due to the strong EMI signal decay. On the other hand, the position $x = 0$ is advantageous because the target is surrounded by sensors and therefore data carry information from multiple views around the targets. At $x = 100$ cm, however, the target is at the edge of the instrument and not immediately under a receiver. The amount of quality data is therefore limited in this case: multi-looks around the target are not available and many receivers are too far away to retain usable information. As a result, inversion results are expected to be best away from the two extreme positions $x = 0$ and $x = 100$ cm.

A systematic inversion of all 11 configurations was carried out on both sets of measurements (mortar + nose cone and mortar + baseplate). The inverted positions for the first set are listed in Table 5 and the time signatures are shown in Figure 4.8(a). The results show polarizabilities of the mortar practically identical for all 11 configurations, as expected since the polarizabilities $\overline{\overline{\beta}}$ are an intrinsic property of the target, independent of its location and orientation. The polarizabilities of the nose cone present more variations, primarily due to the fact that some configurations correspond to a nose cone located close to either $x = 0$ and $x = 100$ cm. Nonetheless, all the signatures are seen to be linear and in good relationship with one another. The inverted positions of both targets remain within ± 1 cm accuracy for x between 20 cm and 60 cm, except for the depth of the nose cone whose error can amount to a few centimeters. The largest error, of about 9 cm, corresponds to the case when the lateral offset is $x = 100$ cm which brings the target at the edge of the instrument.

The results for the second set of measurements (mortar + baseplate), summarized in Table 6 and Figure 4.8(b), present more variations between the 11 configurations (note that the polarizabilities of the baseplate have been scaled by 10^{-2} in order to separate them from those of the mortar). The signature of the mortar, although still clearly separated into a strong component and two smaller identical ones, exhibits more fluctuations than in the previous case but not substantial enough to hinder a proper identification of this target. The polarizabilities of the baseplate also show a flipping dipole behavior between $\hat{x}$ in early time and $\hat{z}$ in late time, albeit somewhat smoothed out in the fluctuations between all the 11 configurations. Note again that fluctuations in the signature of the second object are expected due to its varying position which reaches the extremity of the sensor in some cases.

A series of eleven three-target configurations were analyzed whereby two targets were fixed and one was moving from case to case. The stationary targets were the mortar held horizontally at $(x,y,z) = (0,0,60)$ [cm] and the baseplate held horizontally at $(x,y,z) = (50,0,49)$ [cm]. The moving target was the nose cone held vertically at $(x,y,z) = (dx,0,30)$ [cm] with dx varying from 0 to 100 cm in increments of 10 cm. The recovered positions for these configurations are summarized in Table 7 and show an overall good agreement with the ground truth. The two stationary targets

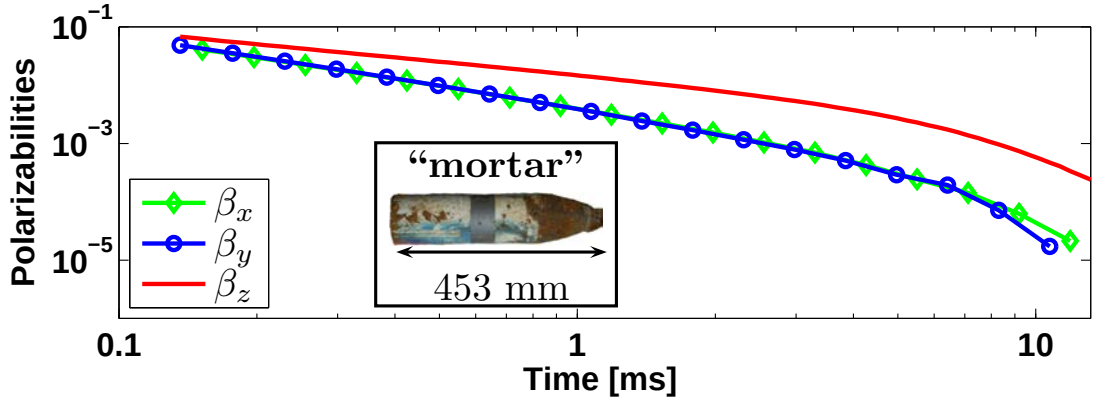

(a) Mortar. Inverted positions: (-0.5,0.6,-60.8) [cm]. True positions: (0,0,60) [cm].

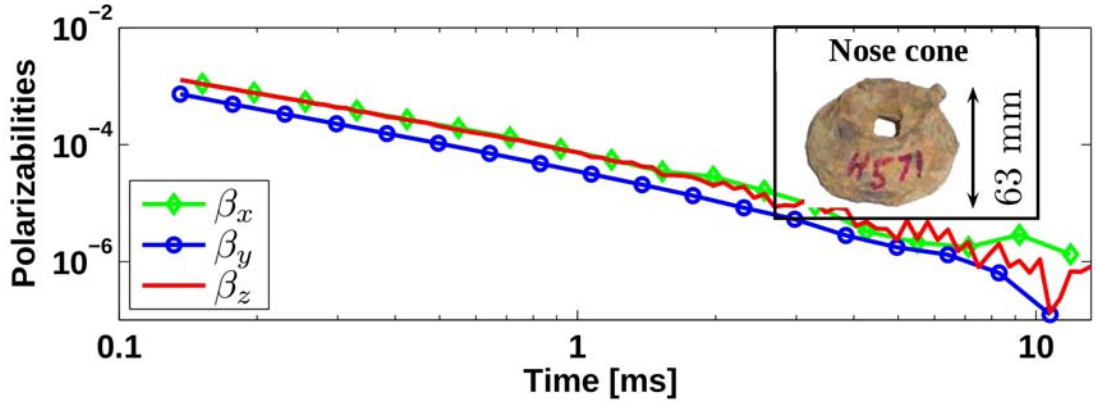

(b) Nose cone. Inverted positions: (0.2,0.2,-30.2) [cm]. True positions: (0,0,30) [cm].

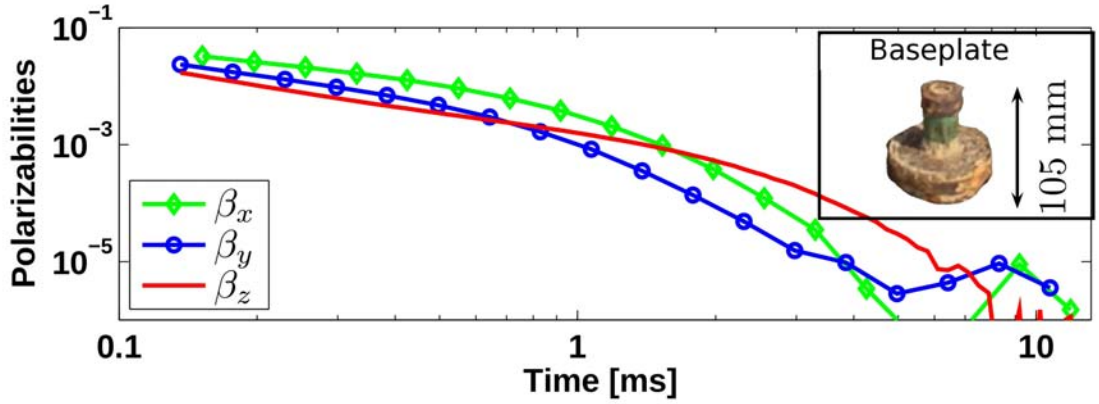

(c) Baseplate. Inverted positions: (0.4,0.1,-47.6) [cm]. True positions: (0,0,49) [cm].

Figure 4.7: Time domain polarizabilities and inverted positions for three independent UXO using TEMTADS data.

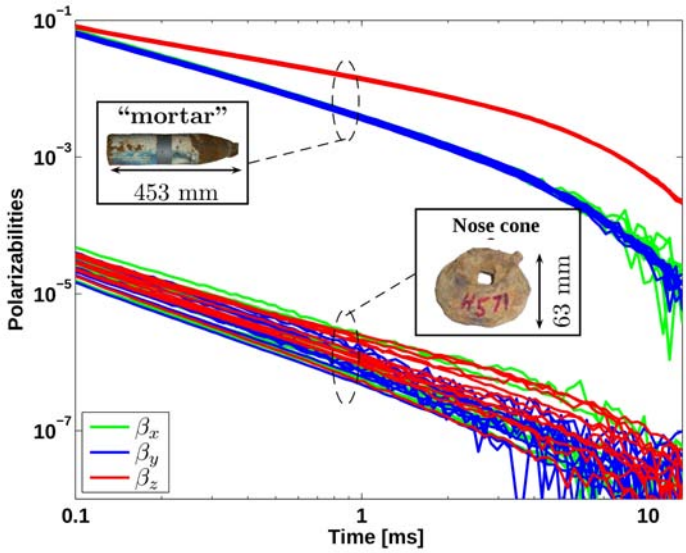

(a) Mortar + Nose cone.

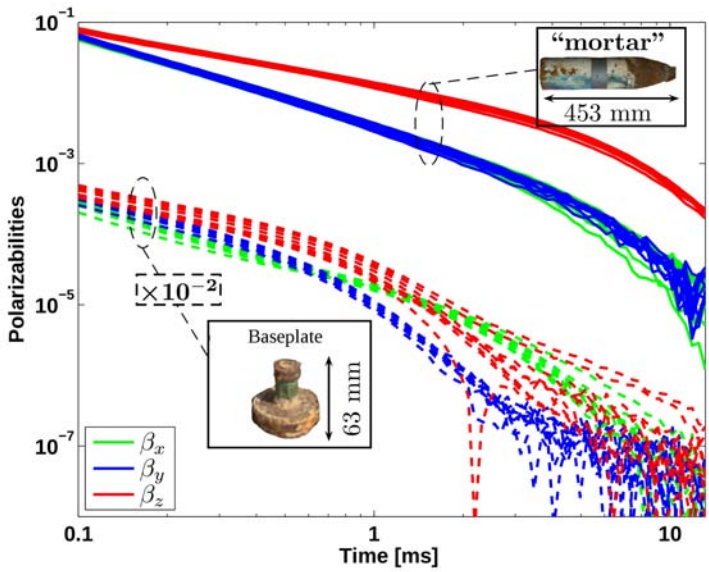

(b) Mortar + Baseplate.

Figure 4.8: Time dependent polarizabilities for two-target inversions from TEMTADS data. The various cases correspond to various lateral displacements along $\hat{x}$ of the shallower target while the deeper one (the mortar) is kept at a constant location. True and inverted positions are given in Table 5 and Table 6. Note that the polarizabilities of the baseplate in (b) have been scaled by 10^{-2} in order to visually separate them from those of the mortar.

	Mortar				Baseplate		
	x	y	z		x	y	z
Truth	0	0	60	dx		0	30
Case							
1	-1	1	62	0	2	0	33
2	0	1	60	10	15	0	30
3	1	1	61	20	21	0	34
4	1	1	61	30	31	0	34
5	1	1	60	40	41	-1	34
6	0	1	61	50	51	0	32
7	1	1	60	60	60	0	33
8	0	1	60	70	67	0	31
9	0	1	60	80	75	0	31
10	0	1	60	90	79	0	33
11	0	1	60	100	80	0	39

Table 5: True and inverted positions of two simultaneous targets whose time dependent polarizabilities are shown in Figure 4.8(a) (TEMTADS data). Ground truth corresponds to a fixed mortar and a moving nose cone along the $\hat{x}$ axis by the indicated dx while keeping y and z constants. Deviations of the first few cases are due to the difficulty in inverting accurate positions when the two targets are on top of each other whereas deviations of the last few cases are explained by the fact that the target location extends beyond the physical size of the sensor. All dimensions are in centimeters and positions are rounded to the closest integer.

are well located in the (xy) plane and the depths are typically estimated within a centimeter for the mortar and within a couple of centimeters for the baseplate, except again in a few isolated cases that correspond for the most part to targets at the edge of the instrument. The positions of the nose cone present more fluctuations while still following the ground truth reasonably well in the majority of cases. The most problematic positions are still those corresponding to the target being at the limit of the field of view of the instrument where an error up to 9 cm in lateral position and 8 cm in depth is recorded. The time-dependent polarizabilities, shown in Figure 4.9, confirm these conclusions. The mortar as well as the baseplate present very consistent signatures from case to case. Interestingly, the signatures of the baseplate are more consistent than in the two-target inversions of Figure 4.8(b), primarily due to the larger lateral separation with the mortar (50 cm in this case). The polarizabilities of the nose cone are a few orders of magnitude lower than those of the mortar and baseplate, but with much more variations from case to case. We again attribute these to two main reasons: overlapping targets and edge effects. Edge effects refer to the effect already witnessed, by which the inverted position and time domain polarizabilities of a target located at the edge of the instrument can present large errors. It is therefore expected that the region close to $x = 100$ cm is a source of inaccurate polarizabilities. The overlapping target effect refers to the fact that EMI signatures are intrinsically challenging to separate for targets in proximity and on top of each other. In this particular set of measurements, the nose cone travels from $x = 0$ to $x = 100$ cm and is directly on top of targets at $x = 0$ (the mortar) and $x = 50$ cm (the baseplate). A case by case examination reveals that the position $x = 0$ is well inverted and that the polarizabilities exhibit the

	Mortar			Baseplate			
	x	y	z		x	y	z
Truth	0	0	60	dx		0	49
Case							
1	-4	1	53	0	-14	3	44
2	10	1	58	10	11	1	48
3	-1	1	56	20	26	1	47
4	1	1	58	30	32	1	48
5	1	0	59	40	41	1	48
6	1	0	59	50	50	0	48
7	1	0	60	60	59	0	47
8	1	0	60	70	67	0	47
9	1	0	60	80	73	0	47
10	0	0	60	90	80	0	49
11	0	0	60	100	89	0	51

Table 6: True and inverted positions of two simultaneous targets whose time dependent polarizabilities are shown in Figure 4.8(b) (TEMTADS data). The ground truth corresponds to a fixed mortar and a moving baseplate along the $\hat{x}$ axis by the indicated dx while keeping y and z constants. Deviations of the first few cases are due to the difficulty in inverting accurate positions when the two targets are on top of each other whereas deviations of the last few cases are explained by the fact that the target location extends beyond the physical size of the sensor. All dimensions are in centimeters and positions are rounded to the closest integer.

expected linear decay (on a log-log scale) visible for example in Figure 4.8(a). The polarizabilities when the nose-cone is close to $x = 50$ cm, however, present much more variation and can be seen in Figure 4.9(a). The major difference between the two situations are the distances between the targets when they coincide laterally: 30 cm in one case and about 20 cm in the other. It is expected that diversification of the positions by allowing for variations in the $\hat{y}$ direction would significantly improve the results. Note also that in all cases, including those challenging ones, the inverted positions remain within reasonable bounds.

4.2.e Discussion and Conclusions

The Gauss-Newton based algorithm presented in this paper has been shown to be effective at simultaneously inverting for the positions, orientations, and time dependent polarizabilities of multiple UXO within the field of view of EMI sensors. Part of the efficiency is due to the construction of the unknown vector, in which positions and orientations of the targets' equivalent dipoles are assumed time independent and inverted for only once using the information of all time channels. Another important aspect of the algorithm is that it is largely based on an analytical derivation of the Jacobian matrix, which therefore provides exact derivatives of the secondary magnetic field with respect to all unknown quantities while reducing the computation time.

Inherent to the method itself, various initial guesses to seed the algorithm and maximum iterations numbers have been tested, depending on the complexity of the cases studied. For single

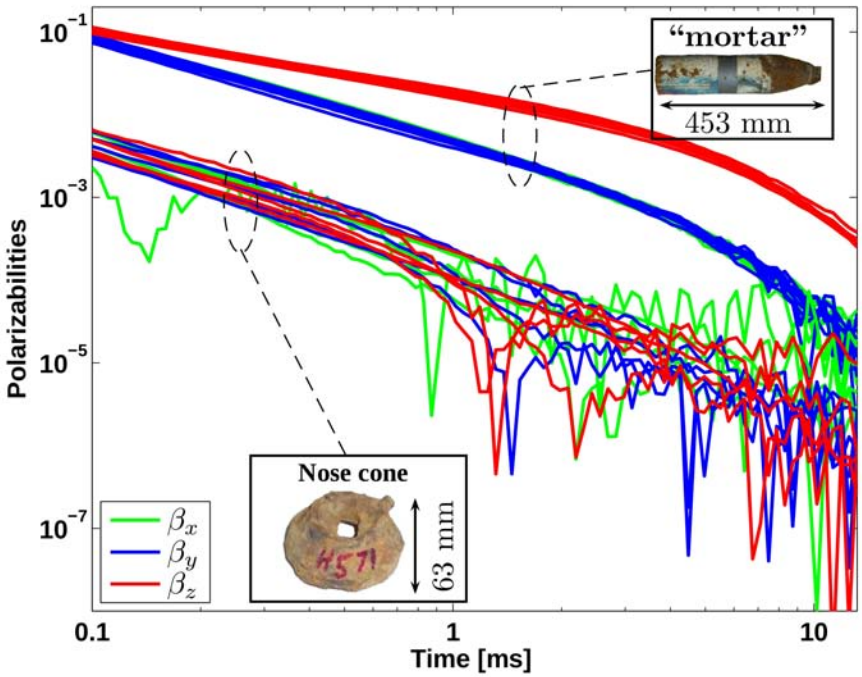

(a) Mortar and nose-cone.

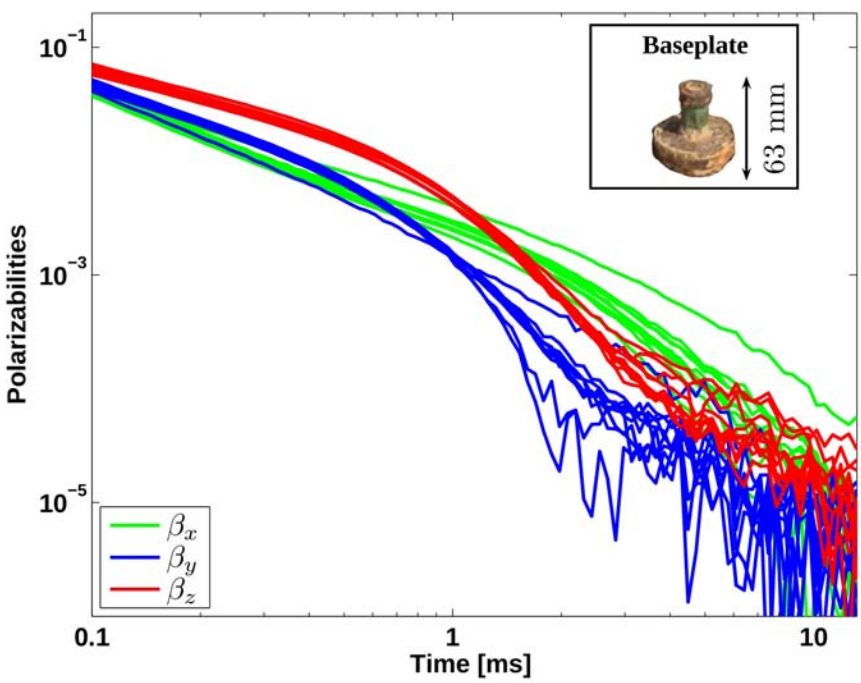

(b) Baseplate.

Figure 4.9: Three-target inversions from TEMTADS data. The mortar and the baseplate are held fixed at $(x,y,z) = (0,0,60)$ [cm] and $(x,y,z) = (50,0,49)$ [cm], respectively, while the nose-cone moves along $\hat{x}$ from case to case. True and inverted positions are given in Table 7.

	Mortar			Baseplate			Nose cone			
	x	y	z	x	y	z		x	y	z
Truth	0	0	60	50	0	49	dx		0	30
Case										
1	2	0	61	50	0	47	0	0	0	36
2	2	1	58	50	0	47	10	14	0	31
3	2	0	59	50	0	47	20	22	1	31
4	2	1	59	51	0	47	30	28	1	34
5	2	1	60	55	1	47	40	37	1	36
6	1	1	59	50	1	49	50	49	0	38
7	3	1	59	42	1	50	60	58	0	36
8	1	1	59	50	0	46	70	81	3	27
9	2	1	59	48	1	48	80	84	0	32
10	2	1	59	47	0	48	90	83	0	38
11	2	1	60	55	0	43	100	-	-	-

Table 7: True and inverted positions of three simultaneous targets whose time dependent polarizabilities are shown in Figure 4.9 (TEMTADS data). The ground truth corresponds to a fixed mortar, a fixed baseplate, and a moving nosecone along the $\hat{x}$ axis by the indicated dx while keeping y and z constants. All dimensions are in centimeters and positions are rounded to the closest integer.

targets, 10 iterations were in general sufficient whereas up to 200 iterations were run for three-target cases. An increased number of iterations naturally results in an increased computation time, which reached almost 3 minutes in case of TEMTADS data inverted on three targets (we recall that the TEMTADS data set is typically much larger than the MPV data set so that inversions are more time consuming). The final solution produced by the algorithm is remarkably insensitive to the initial guess (apart from obvious divergences), provided that the step at each iteration is weighted by a parameter $0 < \alpha < 1$. A value of $\alpha = 0.5$ yielded very consistent inverted positions in all examples shown despite large variations in initial guesses: within ± 50 cm for both x and y coordinates and between -50 cm and -20 cm for the depths. The inverted polarizabilities, however, were more sensitive especially in the three-target cases, yet still within acceptable bounds. To resolve possible variations, the algorithm was run on typically 10 realizations. The selection of the final solution was performed by using two often corroborating criteria. First, the histogram of solutions for the inverted positions was examined and the most frequent solution was declared final. Second, the error was computed between the measured field and the computed field and the solution that produced the lowest error was declared final. In all cases considered these two criteria selected identical solutions. It should also be mentioned that simpler cases such as single target inversion yielded similar final solutions in almost all the cases, so that the criteria proposed above were mostly useful when inverting multi-target configurations.

Finally, we emphasize that the assumption of a known number of targets (i.e. known N in Eq. (4.2.4)) is necessary for the development of the algorithm but is not required in practice and only the knowledge of an upper bound is needed. If the algorithm is run with N larger than the actual number of targets, the algorithm may yield two types of results. First, some dipoles cluster

around a certain location and capture the secondary field of a given UXO better than a single dipole. This situation is not very common but can occur for very heterogeneous targets. More commonly, clusters are very tight and the dipoles find themselves practically at the same location. The corresponding time-dependent polarizabilities need to be added and collectively represent the signature of the target (individual polarizabilities typically do not exhibit any physical behavior). The second type of results obtained if N is larger than the actual number of targets is that some dipoles converge to apparently irrelevant locations, either on the edge of the computational domain and/or well removed from other dipoles, with polarizabilities a few orders of magnitude lower than those of the targets themselves. We attribute this behavior to the algorithm's attempt to find a best fit for noisy data, which is obtained with a few well-identified dipoles and other weaker ones that capture average noise contributions. At the target identification stage, these spurious dipoles are easily filtered out due to their unphysical and weak responses. Note also that this latter behavior prevents the use of the misfit error to determine the number of targets since smaller errors are typically obtained with more dipoles. Consequently, the algorithm does not require the exact knowledge of the number of targets for their proper identification, and only an upper bound needs to be estimated. This topic is currently under investigation.

4.3 The Joint Diagonalization Technique

Efforts to discriminate buried unexploded ordnance from harmless surrounding clutter are often hampered by the uncertainty in the number of buried targets producing a given detected signal. In this section, we present a technique that helps determine that number with no need for data inversion. The procedure is based on the joint diagonalization of a set of multi-static response (MSR) matrices measured at different time gates by a time-domain electromagnetic induction sensor. In particular, we consider the Naval Research Laboratory's Time-domain Electromagnetic Multi-sensor Towed Array Detection System (TEMTADS), which consists of a 5×5 square grid of concentric transmitter/receiver pairs. The diagonalization process itself generalizes one of the standard procedures for extracting the eigenvalues of a single matrix; in terms of execution time it is comparable to diagonalizing the matrices one by one. We present the method, discuss and illustrate its mathematical basis and physical meaning, and apply it to several actual measurements carried out with TEMTADS at the Aberdeen Proving Ground test stand in Maryland and in the field at the former Camp Butner in North Carolina. We find that each target in a measurement is associated with a set of nonzero time-dependent MSR eigenvalues (usually three), which enables estimation of the number of targets interrogated. These eigenvalues have a characteristic shape as a function of time that does not change with the location and orientation of the target relative to the sensor. We justify analytically and numerically that symmetric targets have pairs of eigenvalues with constant ratios between them.

4.3.a Introduction

Several models used with success to detect and characterize buried metal targets build on the premise that the currents and domains that generate electromagnetic response are not distributed uniformly within each target but instead tend to concentrate around certain singular points or regions. The techniques synthesize that response as though it consisted of a set of analytic solutions of the Maxwell equations due to point sources located at those so-called "scattered field singularities" [54–56]. The time-dependent behavior of these sources is used to characterize and classify the causative targets. (In this work we use "source" to refer to these elementary analytic solutions, and not, as is often the case in geophysics, to transmitters.) The number of scattered field singularities depends on the wavelength and on the scatterers' geometry and material properties. In the EMI frequency regime, where the wavelengths are significantly larger than the targets' characteristic lengths, most homogeneous compact targets have a dominant singularity at their centers. Therefore the simplest and most widely used approach replaces each target with a single point magnetic dipole located near its geometric center [57–64]. This point dipole model tends to work best for relatively small and distant targets, and in terms of predictive accuracy and consistency has been superseded by generalizations that distribute dipole-moment densities over surfaces or volumes [65, 66]. On the other hand, all of these models fare less well when analyzing anomalies due to more than one target: the inversion becomes more computationally expensive, has more local minima, and may require regularization [67–69]. When the number of targets is not known a priori, as in all real-world tests, the situation is complicated further, since the models must be run several times (assuming different target numbers) and have the tendency to overfit the data.

The approach we introduce here is designed to make a fast estimate of the number of targets in a cell. It is not meant to replace actual inversion, since it does not yield location informa-

tion and does not characterize targets with complete precision, but rather constitutes an initial pre-processing step. (The inversion routines that use as input the resulting number estimates are presented elsewhere [65, 66] and will be studied in detail in Sec. 4.4). The technique is based on the joint diagonalization (JD) of a sequence of square time-dependent multi-static response (MSR) matrices that are synthesized directly from measured EMI signals without invoking a forward model. The number of nonzero time-dependent eigenvalues of the set of matrices is related to the number of meaningful elementary sources present in the illuminated cell. As will be shown in the Methods section, a single source generating three eigenvalues may suffice to describe a small or deeply buried target. A complex field structure, caused by a large, heterogeneous, or very shallow target, may require more than one elementary source (and thus more than three time-dependent eigenvalues) to describe the resulting field adequately. Objects like thin wires or rings that are "small" along one or more dimensions may require less than three time-dependent eigenvalues.

Joint diagonalization has become an important tool for signal processing and inverse problems, including independent component analysis [70], blind source separation or BSS [71], common principal component analysis, and kernel-based nonlinear BSS [72]. To the best of our knowledge, this is the first use of this technique for UXO remediation.

4.3.b Methods

4.3.b.(1) The TEMTADS sensor array EMI sensors operate at very low frequencies (a few Hz to a few hundred kHz) in order to penetrate conductive ground, resulting in data with poor spatial resolution. Advanced EMI sensors have been designed to overcome this limitation: they enhance the information content of the data by increasing the number of sensor/target attitudes and reduce positioning uncertainty by employing rigid arrays of transmitters and receivers. One such instrument is the Time-domain Electromagnetic Multi-sensor Towed Array Detection System (TEMTADS), developed by the Naval Research Laboratory and G&G Sciences, Inc. [73], to which we restrict attention.

Shown in Fig. 4.10, TEMTADS is a time-domain EMI sensor that consists of 25 transmitter/receiver (Tx/Rx) pairs, each composed of a 35-cm square transmitter loop surrounding a 25-cm square receiver loop. The Tx/Rx pairs are arrayed as a rectangular 5×5 grid with 40-cm neighbor-to-neighbor separation for a total array dimension of 2 m. At each location, the sensor activates the transmitter loops in sequence, and for each transmission all receivers record signals, providing 625 EMI transients from $\approx$100 μs to 25 ms over $N_g = 123$ time gates.

4.3.b.(2) Multi-static response matrices To construct the MSR matrices one assembles the 625 readings at each time gate into a 25×25 array so that each column stands for one of N_t transmitters and each row represents one of N_r receivers:

$$\mathbf{S}(t_k) = \begin{bmatrix} H_{11} & H_{12} & \cdots & H_{1N_t} \\ H_{21} & H_{22} & \cdots & H_{2N_t} \\ \vdots & \vdots & \ddots & \vdots \\ H_{N_r1} & H_{N_r2} & \cdots & H_{N_rN_t} \end{bmatrix}, \; k = 1, \ldots, N_g, \tag{4.3.1}$$

where the element H_{ij} is the field measured by the i-th receiver when the j-th transmitter is active. Below we look at the time development of the MSR sequence; here we concentrate on a single

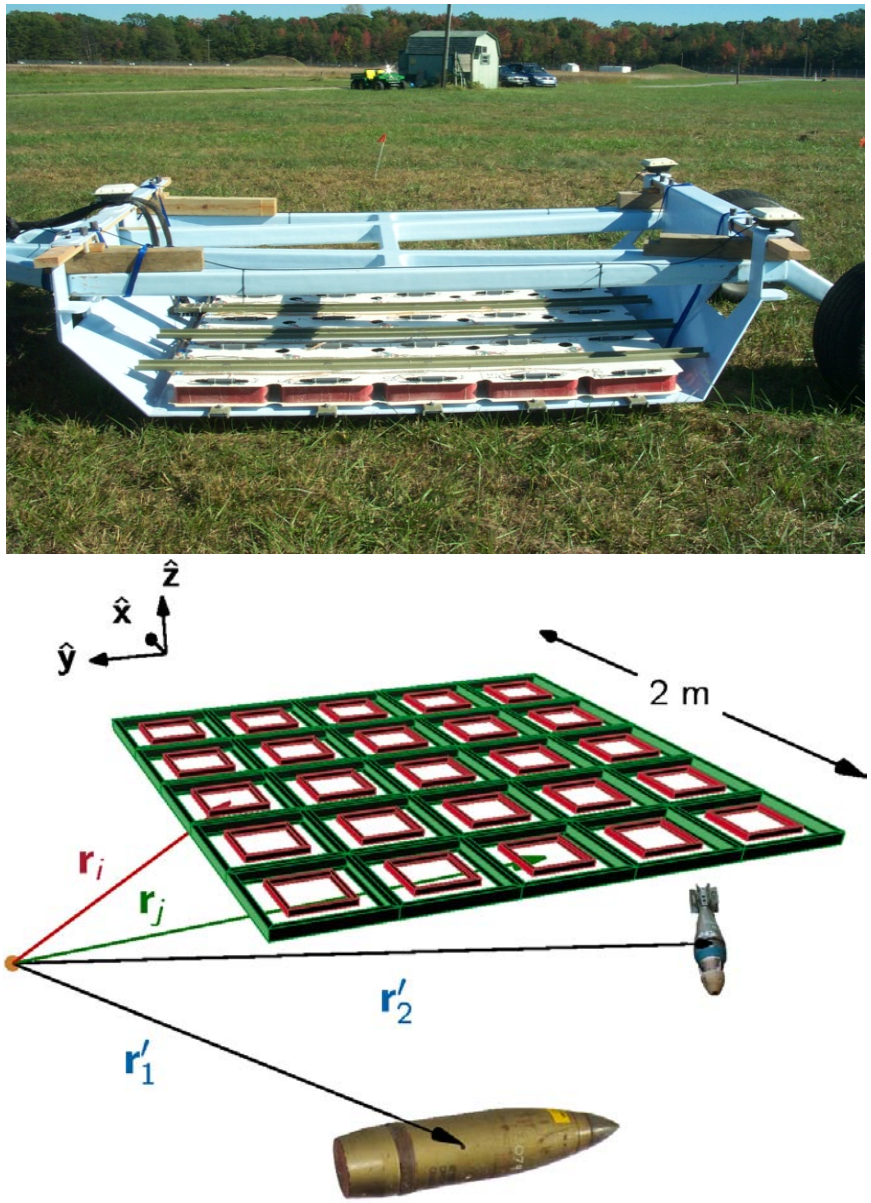

Figure 4.10: The TEMTADS sensor array consists of a 5 ×5 grid of concentric transmitter-receiver pairs forming a square of side 2 m. At each instrument location the transmitters are activated one at a time, and in each case all 25 receivers take a reading, for a total of 625 data points. Two typical objects are also shown.

time gate and interpret the information contained in each matrix. It is shown in this section that the measured data are resolved as a superposition of "elemental" spatio-temporal sub-signals, each related to the EMI signature of an elementary magnetic dipole source. Assume there are N such sources. We postulate that the field of the j-th transmitter, immediately upon being shut off, induces in the l-th source a dipole moment given by

$$\mathbf{m}_{jl} = \mathbf{U}_l \mathbf{\Lambda}_l \mathbf{U}_l^T \mathbf{B}_{jl}^{\mathrm{pr}}, \tag{4.3.2}$$

where $\mathbf{B}_{jl}^{\mathrm{pr}}$ represents the primary magnetic induction and the Euler rotation matrix $\mathbf{U}_l$ relates the transmitter array coordinate axes to the principal axes of the source. The diagonal polarizability matrix $\mathbf{\Lambda}_l$, intrinsic to the source, measures the strength of the moment that the primary field induces along each of the source axes. This polarizability matrix in principle contains all the time-dependent information in the measured secondary signal.

To compute the primary magnetic induction $\mathbf{B}_{jl}^{\mathrm{pr}}$ recall that the TEMTADS transmitter assembly consists of coplanar square loops forming a regular grid. The Biot-Savart law prescribes the primary magnetic induction at location $\mathbf{r}_l$ of the l-th source when the j-th transmitter antenna (of area σ_{Tx_j}) is excited by a current I_j:

$$\mathbf{B}_{jl}^{\mathrm{pr}} = \frac{\mu_0 I_j}{4\pi} \sigma_{\mathrm{Tx}_j} \frac{1}{\sigma_{\mathrm{Tx}_j}} \oint_{\mathrm{Tx}_j} \frac{d\mathbf{l}' \times (\mathbf{r}_l - \mathbf{r}')}{|\mathbf{r}_l - \mathbf{r}'|^3} = \mathbf{g}_{jl}^{\mathrm{pr}} \sigma_{\mathrm{Tx}_j} I_j, \tag{4.3.3}$$

where μ_0 is the permeability of free space, $d\mathbf{l}'$ is the usual Biot-Savart line element, and we have introduced the normalized Green function $\mathbf{g}_{jl}^{\mathrm{pr}}$.

According to Faraday's law, the signal measured by a receiver coil is the negative time derivative of the magnetic flux passing through it. (Long enough after transmitter shut-off, this flux is purely secondary.) The field at $\mathbf{r}$ of a dipole of moment $\mathbf{m}$ at $\mathbf{r}_l$ is

$$\mathbf{B} = \frac{\mu_0}{4\pi} \nabla \times \left(\mathbf{m} \times \frac{\mathbf{r} - \mathbf{r}_l}{|\mathbf{r} - \mathbf{r}_l|^3} \right), \quad \text{and thus} \quad \int \mathbf{B} \cdot d\mathbf{s} = -\mathbf{m} \cdot \frac{\mu_0}{4\pi} \oint d\mathbf{l} \times \frac{\mathbf{r} - \mathbf{r}_l}{|\mathbf{r} - \mathbf{r}_l|^3} \tag{4.3.4}$$

by straightforward application of Stokes's theorem. Thus the signal sampled at time t_k by the i-th receiver (of area σ_{Rx_i}) when the l-th source is excited by the j-th transmitter is

$$\begin{aligned} H_{ij}^l(t_k) \sigma_{\mathrm{Rx}_i} \sigma_{\mathrm{Tx}_j} I_j &= \frac{\mu_0}{4\pi} \sigma_{\mathrm{Rx}_i} \frac{1}{\sigma_{\mathrm{Rx}_i}} \oint_{\mathrm{Rx}_i} \frac{d\mathbf{l}'_i \times (\mathbf{r}' - \mathbf{r}_l)}{|\mathbf{r}' - \mathbf{r}_l|^3} \cdot \dot{\mathbf{m}}_{jl}(t_k) = \mathbf{g}_{li}^{\mathrm{sc}} \sigma_{\mathrm{Rx}_i} \cdot \dot{\mathbf{m}}_{jl}(t_k) \\ &= \mathbf{g}_{li}^{\mathrm{sc}} \sigma_{\mathrm{Rx}_i} \cdot [\mathbf{U} \dot{\mathbf{\Lambda}}_l(t_k) \mathbf{U}^T] \cdot \mathbf{g}_{jl}^{\mathrm{pr}} \sigma_{\mathrm{Tx}_j} I_j, \end{aligned} \tag{4.3.5}$$

where a dot over a variable indicates its time derivative. We have also introduced the normalized Green function $\mathbf{g}_{li}^{\mathrm{sc}}$ in analogy with $\mathbf{g}_{jl}^{\mathrm{pr}}$; the two are seen to have the same form. In equations 4.3.4 and 4.3.5 the line element $d\mathbf{l}'$ lies on the x-y plane, and as a consequence the Green functions are similar in structure to those of the simple model presented in AppendixA.3 (in which vertical dipoles establish the primary field and only the z-component of the secondary field is measured). Note that in the definition of the received signal we have included the exciting current I_j and the transmitter and receiver areas; these quantities are known and can be factored out.

At a given time gate, and with only the l-th source present, we construct the MSR matrix for the complete transmitter/receiver array by tiling all the $N_r \times N_t$ available samples of expression 4.3.5:

$$\mathbf{S} = \mathbf{G}^{\mathrm{sc}}\mathbf{U}_l\dot{\mathbf{\Lambda}}_l\mathbf{U}_l^T(\mathbf{G}^{\mathrm{pr}})^T = (\mathbf{G}^{\mathrm{sc}}\mathbf{U}_l)\dot{\mathbf{\Lambda}}_l(\mathbf{G}^{\mathrm{pr}}\mathbf{U}_l)^T, \tag{4.3.6}$$

where the primary (or transmitter) dyad $\mathbf{G}^{\mathrm{pr}}$ is of size $N_t \times 3$, the secondary (or receiver) dyad $\mathbf{G}^{\mathrm{sc}}$ is of size $N_r \times 3$, and the response matrix $\mathbf{U}_l\dot{\mathbf{\Lambda}}_l\mathbf{U}_l^T$ is 3×3. The matrix $\mathbf{S}$ has size $N_r \times N_t$ and is square if $N_r = N_t$, as with TEMTADS. Moreover, the condition $\mathbf{G}_l^{\mathrm{sc}} = \mathbf{G}_l^{\mathrm{pr}} \equiv \mathbf{G}_l$ holds approximately even though the receivers do not coincide exactly with the transmitters. This means that the matrix can be diagonalized to yield real eigenvalues and eigenvectors. (This diagonalization is more precisely a singular value decomposition (SVD) for each time gate, and in what follows we use "diagonalization" as shorthand for "SVD of a symmetric matrix.") Since $\mathbf{U}_l\dot{\mathbf{\Lambda}}_l\mathbf{U}_l^T$ is 3×3, the matrix $\mathbf{S}$ has only three nonzero eigenvalues for a single source; this property is the basis of the method. When there is more than one source present, the decomposition 4.3.6 expands to

$$\begin{aligned}\mathbf{S} &= \begin{bmatrix} \mathbf{G}_1^{\mathrm{sc}} & \mathbf{G}_2^{\mathrm{sc}} & \cdots \end{bmatrix} \begin{bmatrix} \mathbf{U}_1\dot{\mathbf{\Lambda}}_1\mathbf{U}_1^T & 0 & \cdots \\ 0 & \mathbf{U}_2\dot{\mathbf{\Lambda}}_2\mathbf{U}_2^T & \cdots \\ \vdots & \vdots & \ddots \end{bmatrix} \begin{bmatrix} (\mathbf{G}_1^{\mathrm{pr}})^T \\ (\mathbf{G}_2^{\mathrm{pr}})^T \\ \vdots \end{bmatrix} \\ &= \begin{bmatrix} \mathbf{G}_1^{\mathrm{sc}}\mathbf{U}_1 & \mathbf{G}_2^{\mathrm{sc}}\mathbf{U}_2 & \cdots \end{bmatrix} \begin{bmatrix} \dot{\mathbf{\Lambda}}_1 & 0 & \cdots \\ 0 & \dot{\mathbf{\Lambda}}_2 & \cdots \\ \vdots & \vdots & \ddots \end{bmatrix} \begin{bmatrix} (\mathbf{G}_1^{\mathrm{pr}}\mathbf{U}_1)^T \\ (\mathbf{G}_2^{\mathrm{pr}}\mathbf{U}_2)^T \\ \vdots \end{bmatrix},\end{aligned} \tag{4.3.7}$$

where again $\mathbf{G}_l^{\mathrm{sc}} = \mathbf{G}_l^{\mathrm{pr}} \equiv \mathbf{G}_l$. Formally, the "intrinsic" middle matrix in decomposition 4.3.7 has size $3N \times 3N$, where N is the number of sources; numerically it is a $3N \times 3N$ block-diagonal matrix padded with zeros to reach a size of $N_r \times N_t$ and thus with only $3N$ nonzero eigenvalues. The method should be able to resolve up to $\lfloor N_r \rfloor$ responding dipole sources, or eight for TEMTADS.

This procedure would be equivalent to full inversion (though without the positional information) if one could extract directly the derivative $\dot{\mathbf{\Lambda}}$ of the polarizability matrix. This is not possible, however, because the Green dyads are not orthogonal. The actual quantities obtained from the diagonalization can be found by replacing the Green dyads by their SVDs:

$$\mathbf{S} = \mathbf{G}\mathbf{U}\dot{\mathbf{\Lambda}}\mathbf{U}^T\mathbf{G}^T = \mathbf{W}\left[\mathbf{\Sigma}\mathbf{V}^T\mathbf{U}\dot{\mathbf{\Lambda}}\mathbf{U}^T\mathbf{V}\mathbf{\Sigma}\right]\mathbf{W}^T = \mathbf{W}\mathbf{Z}\mathbf{\Delta}\mathbf{Z}^T\mathbf{W}^T = \mathbf{Y}\mathbf{\Delta}\mathbf{Y}^T. \tag{4.3.8}$$

(The matrix within brackets in the second step is real and symmetric and thus has a purely real eigendecomposition.) Result 4.3.8 shows that the eigenvalues stored in matrix Δ are not solely composed of source responses, but also contain location and orientation information from the Green dyads. The crucial point is that the eigenvalues contain all of the time dependence of the signal, a property that we now exploit.

4.3.b.(3) Time development of the MSR eigenvalues The second step of the procedure consists of incorporating the time dependence of the MSR matrices to the eigenvalue analysis from the previous section. As we shall see in the Results section, this information is more useful if each eigenvalue can be tracked separately as the signal decays and associated with the same time-independent eigenvector. Thus it is necessary to diagonalize the $N_g = 123$ matrices simultaneously such that they share the same set of orthonormal time-independent eigenvectors and these appear

in the same order at all times. Denoting again as $\mathbf{S}(t_k)$ the MSR matrix at the k-th time gate, a unitary matrix $\mathbf{V}$ is sought such that the products

$$\mathbf{D}_k = \mathbf{V}^T \mathbf{S}(t_k) \mathbf{V} \tag{4.3.9}$$

are "as diagonal as possible" in the sense of definition A.4.1 in AppendixA.4. From now on we concentrate on these time-decaying diagonal elements, referring to them as "eigenvalues" even though eigenvalues are in rigor scalars, not curves, and describing them as "parallel" or "crossing each other" in a way that the figures will make clear.

One could in principle diagonalize the MSR matrix at each time gate, and the eigenvectors, which depend only on geometry, should stay constant. The fact that we cannot know a priori the order in which the eigenvalues and their corresponding eigenvectors result from each single-gate diagonalization would be only a minor complication if the data had no noise. Instead, we look for an orthogonal matrix of eigenvectors that diagonalizes all the MSR matrices simultaneously. Two different procedures, described in AppendixA.4, were employed, with identical results. The most efficient one [71, 74, 75] is a well-known generalization of the Jacobi method for diagonalizing single matrices.

4.3.c Results

4.3.c.(1) Test-stand measurements The main purpose of the JD technique is to estimate the number of targets producing a given measured signal. In this section we first describe an idealized experiment that was designed to act as a benchmark for multi-target scenarios while avoiding some of the complications that arise in the field. The experiment was carried out at the Aberdeen Proving Ground test-stand facility in Maryland by personnel from Nova Research, Inc. on 15 January 2010. The setup is depicted in Fig. 4.11. The TEMTADS sensor array was placed on an elevated platform. Underneath, several targets were added in sequence to form an increasingly complex scene, with the instrument measuring the response of every configuration.

The targets of interest (TOI) were two common UXO, a 105mm M60 howitzer shell and a 60-mm mortar round. Each lay on its side with nose pointing in the $+\hat{\mathbf{x}}$ direction: the 105-mm was at a depth of 63 cm below the center of the sensor, while the 60-mm was 38 cm below the instrument and displaced 40 cm in the $-\hat{\mathbf{y}}$-direction from the sensor center. A sphere and a spheroid were successively placed 27.5 cm below TEMTADS to simulate shallow clutter with the potential to obscure the targets of interest. The sphere, placed at $10(\hat{\mathbf{x}}+\hat{\mathbf{y}})$ cm from the origin, was made of aluminum and was 10 cm in diameter; the spheroid, made of steel with major and minor axes 20 cm and 4 cm respectively, was at $-(30\hat{\mathbf{x}}+40\hat{\mathbf{y}})$ cm from the center.

Initially the targets were interrogated individually. Figure 4.12(a) shows the complete set of 25 eigenvalues obtained for the 105mm shell, Fig. 4.12(b) shows the same result for the 60-mm round, and Fig. 4.13 displays the decay curves for the sphere and spheroid added in the course of the experiment. In all cases, at least three time-dependent eigenvalues emerge from the background noise. (Eigenvalues that could be associated with high-order sources such as quadrupoles are indistinguishable from the noise.) Two eigenvalues look parallel to one another (i.e., there is a constant ratio between the two); for the sphere of Fig. 4.13(upper) two coincide and the third is parallel. This parallelism is indicative of cylindrical symmetry, as we justify in AppendixA.3 using a simplified model. The 60-mm round has eigenvalues of comparable size to those of the 105-mm shell, even though the target is much smaller. This is due to the fact that the eigenvalues do not

Figure 4.11: A test-stand experiment featuring an increasing number of targets under interrogation by TEMTADS. As in Fig. 4.10, the system is observed essentially head-on from the $+\hat{\mathbf{y}}$-direction.

store only intrinsic responses but also positional information. It can also be noted that the 105-mm shell has at least one more above-noise eigenvalue, showing that it is not as accurately represented by a single source as the 60-mm round.

The fact that the eigenvalues change with location point out the necessity of diagonalizing the sequence of MSR matrices simultaneously. Consider the 60-mm round of Fig. 4.12(b). TEMTADS measurements were carried out on the same target at a different set of locations: Under the sensor at a depth of 35 cm (3 cm shallower than in Fig. 4.12(b)), $-10(\hat{\mathbf{x}}+\hat{\mathbf{y}})$ cm from the center and 29.5 cm below the sensor, and at the latter depth but under the center. Figure 4.14 shows the eigenvalue decay curves that result from carrying out joint diagonalization on these three data sets and Fig. 4.15 shows the same decay curves computed time gate by time gate using the SVD. Both methods find three above-threshold eigenvalues and correctly predict that there is only one target, but the eigenvalues' time developments have a crucial difference: the JD eigenvalues preserve their shapes case to case, even as the relative amplitudes vary, while those obtained with the SVD change shape as the object location varies. The simple sorting provided by the SVD explicitly disallows the eigenvalue crossings that help preserve their shapes and the parallelism that reveals possible symmetry; a more systematic procedure based on eigenvector comparison (as opposed to eigenvalue comparison) works well for one-target scenarios but breaks down in multi-target cases, where there are many more decay curves crossing each other. Again, the number of sources would be estimated correctly, but potentially important information given by the decay shape would be lost.

Figure 4.16(upper) shows the eigenvalue decay curves for the configuration consisting of the two TOI at the locations from Fig. 4.12. There are seven above-noise eigenvalue curves, indicating that there are at least two targets in the data. The two sets of crossing decay curves from Fig. 4.12

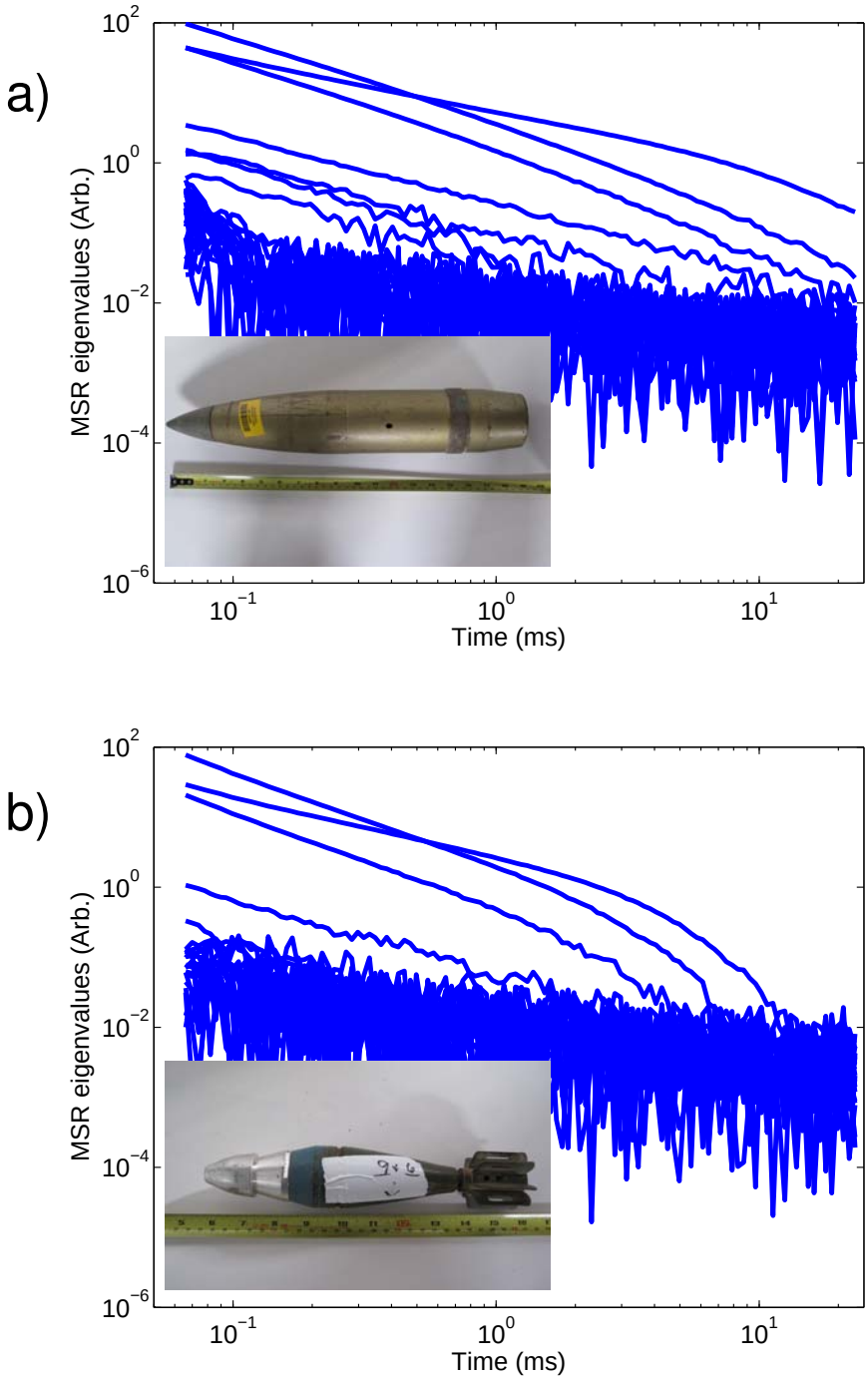

Figure 4.12: (a) Eigenvalues of the TEMTADS multi-static response matrix for a 105-mm M60 howitzer shell (shown in the inset). (b) Eigenvalues of the TEMTADS multi-static response matrix for a 60-mm M49 mortar round (shown in the inset).

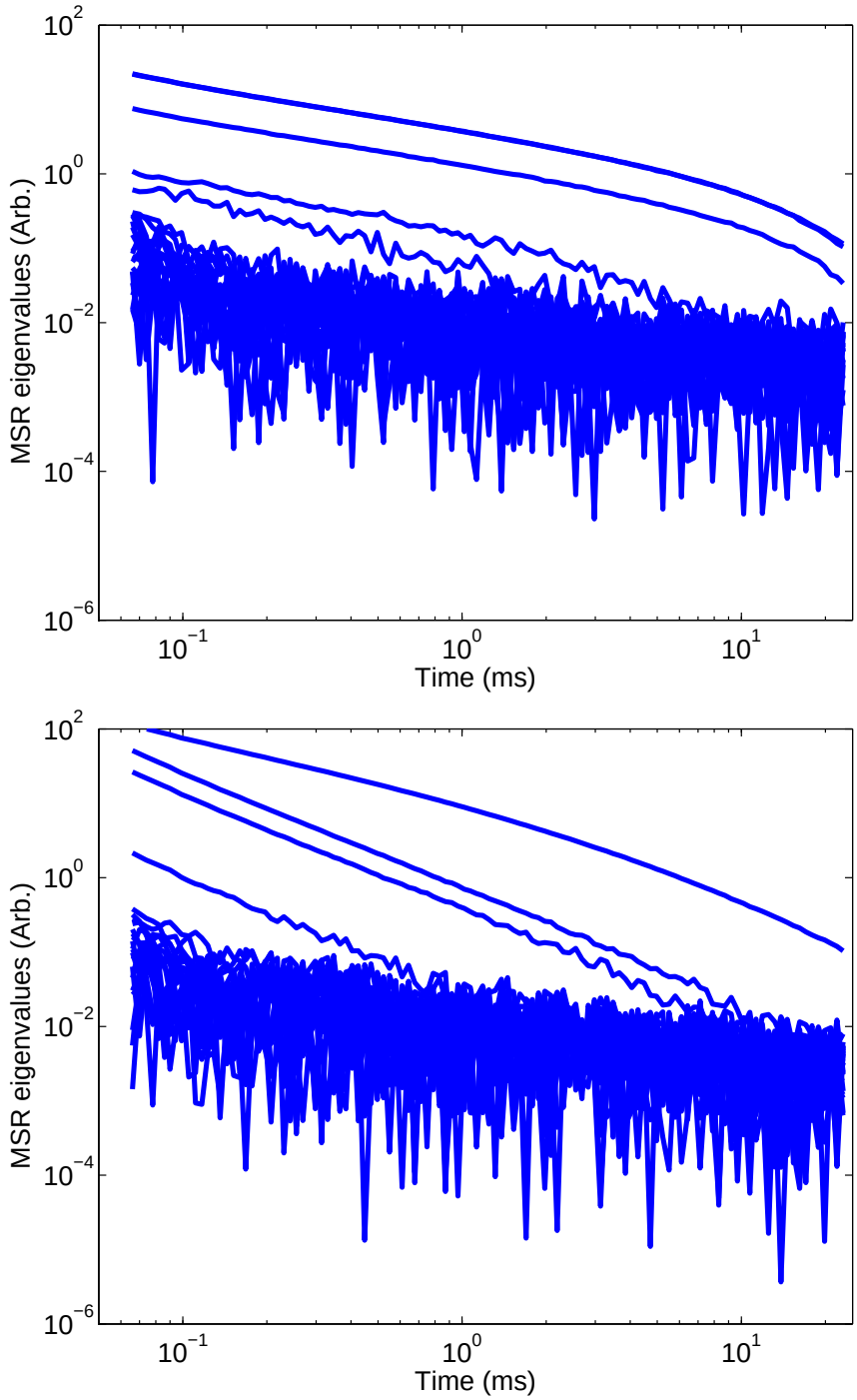

Figure 4.13: Measured eigenvalues for an aluminum sphere of diameter 10 cm (upper) and a steel prolate spheroid (lower) of minor and major axes respectively 4 and 20 cm.

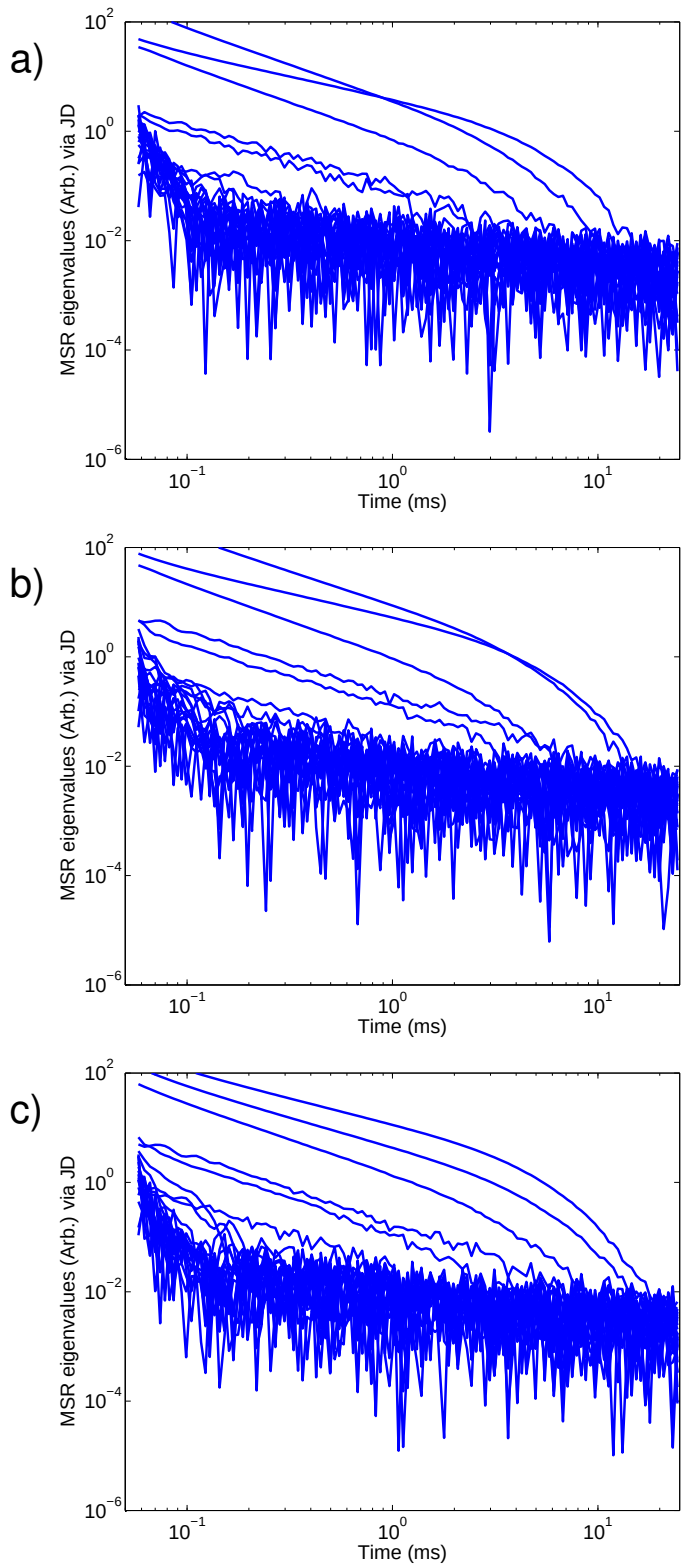

Figure 4.14: Eigenvalues for the 60-mm round computed using joint diagonalization for three different object locations.

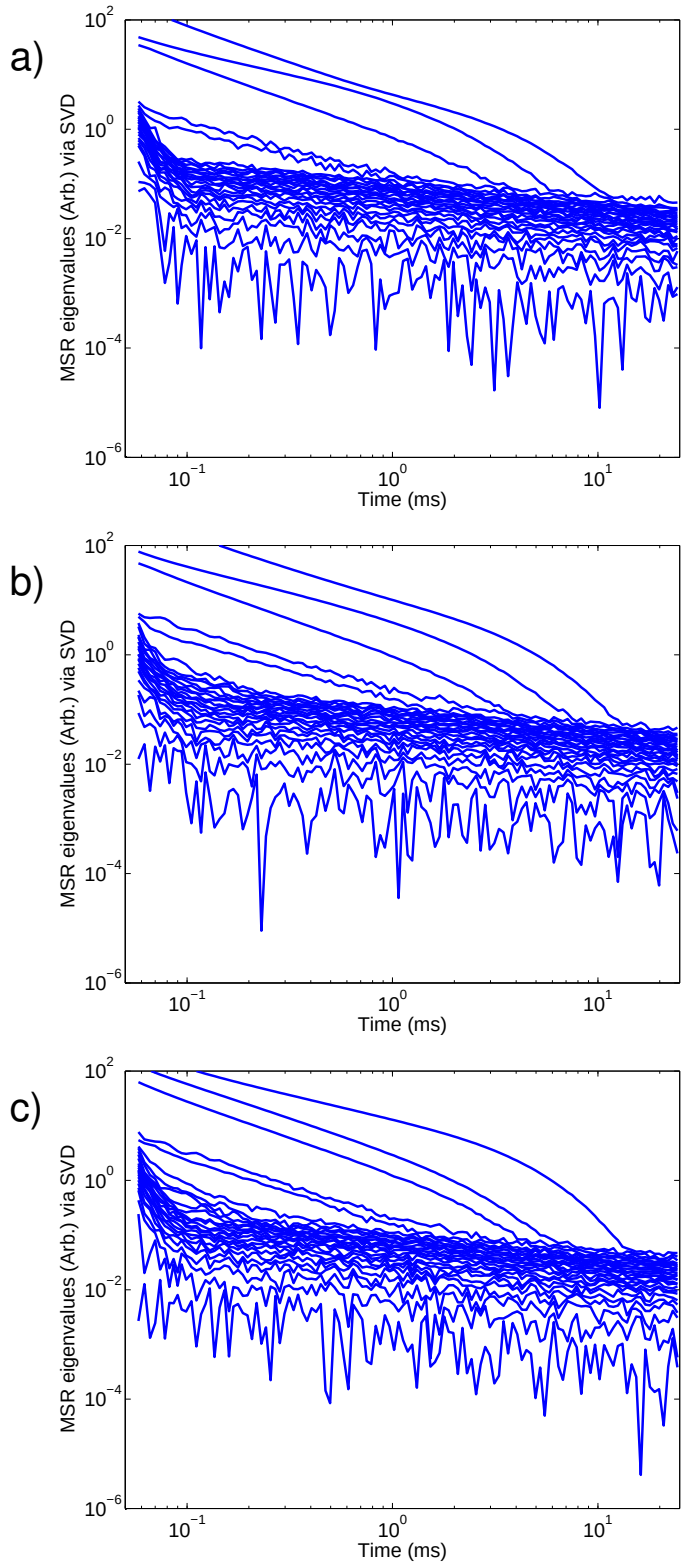

Figure 4.15: Eigenvalues for the 60-mm round computed using the SVD at each time gate for three different object locations.

are visible now as a weighted nonlinear superposition of the individual responses, including the third eigenvalue associated with the larger shell. Figure 4.16(b) and (c) show the MSR eigenvalues obtained after sequentially adding the first and second clutter items. Ten eigenvalue curves are above the noise in panel (b), revealing the presence of three targets, and 12 curves appear in panel (c), showing that the number has increased. The eigenvalue signatures of the original targets can still be discerned, but they are mixed with contributions from clutter items. A scenario with more than six nonzero eigenvalues potentially indicates the presence of a single large shallow target or of several smaller ones and will be routinely dug out when encountered in the field.

4.3.c.(2) Camp Butner blind test As part of its effort to make UXO remediation faster and more economic, the Environmental Strategic Technology Certification Program (ESTCP) of the Department of Defense is in the process of administering a series of blind classification tests of increasing realism to measure the progress made in the development of sensors and inversion and classification algorithms. The first test [65, 76], held in 2007 at the former Camp Sibert in Alabama, was relatively straightforward: it was required to discriminate between large, intact 4.2" mortar rounds and smaller explosion byproducts and assorted debris. The data were taken by two first-generation sensors, the EM-61 and EM-63, both developed by Geonics, Inc. There were 150 cells plus 66 for calibration, each one well separated from the others and containing only one target.

The second test [77, 78] was held in 2009 near San Luis Obispo in California. This new test better reflected the wide range of dangerous targets usually present in the field: there were samples of 60-mm mortars, 2.36" rockets (whole and fragments), 81-mm projectiles, and 4.2" mortars; three additional munition types were discovered during the course of the demonstration. Each cell contained an unspecified number of dangerous and/or innocuous targets. The participants were expected to identify the UXO by type. The test, moreover, featured a more demanding topography. Magnetometers and commercially available first-generation sensors were used to detect and flag anomalies that were then interrogated more closely by state-of-the art EMI instruments (TEMTADS, the Berkeley UXO Discriminator, and the Geometrics MetalMapper). The test was at a much larger scale, comprising over 1000 data sets for each instrument.

The third test [79], on which we concentrate here, took place at the former Camp Butner in North Carolina. Camp Butner functioned as a training ground for infantry divisions and artillery and engineering units during World War II. A large variety of munitions were reportedly used there; at the test site, the targets of interest consisted mostly of 37-mm projectiles (with and without a copper driving band) and 105-mm howitzer shells and HEAT rounds. The clutter items were typical explosion byproducts such as partial shells and fuzes, along with smaller shrapnel and non-ordnance metallic debris. Many of the fragments were similar in size and wall thickness to the 37-mm projectiles [80]. The test started with an exploratory cart-based survey using the Geonics EM-61 sensor. The cells in which the EM-61 data indicated the presence of an anomaly (with one or more metallic targets) were then subjected to cued examination with TEMTADS. A total of 2290 cells were interrogated, of which 171 corresponded to potentially hazardous targets. The discrimination results obtained by our group are published elsewhere [81]. Here we demonstrate only our usage of JD to estimate numbers of targets and illustrate shape differences.

Figure 4.17 shows typical examples of the two kinds of 105-mm projectiles found at the site, along with the time-dependent MSR eigenvalues extracted from the cells that contained them.

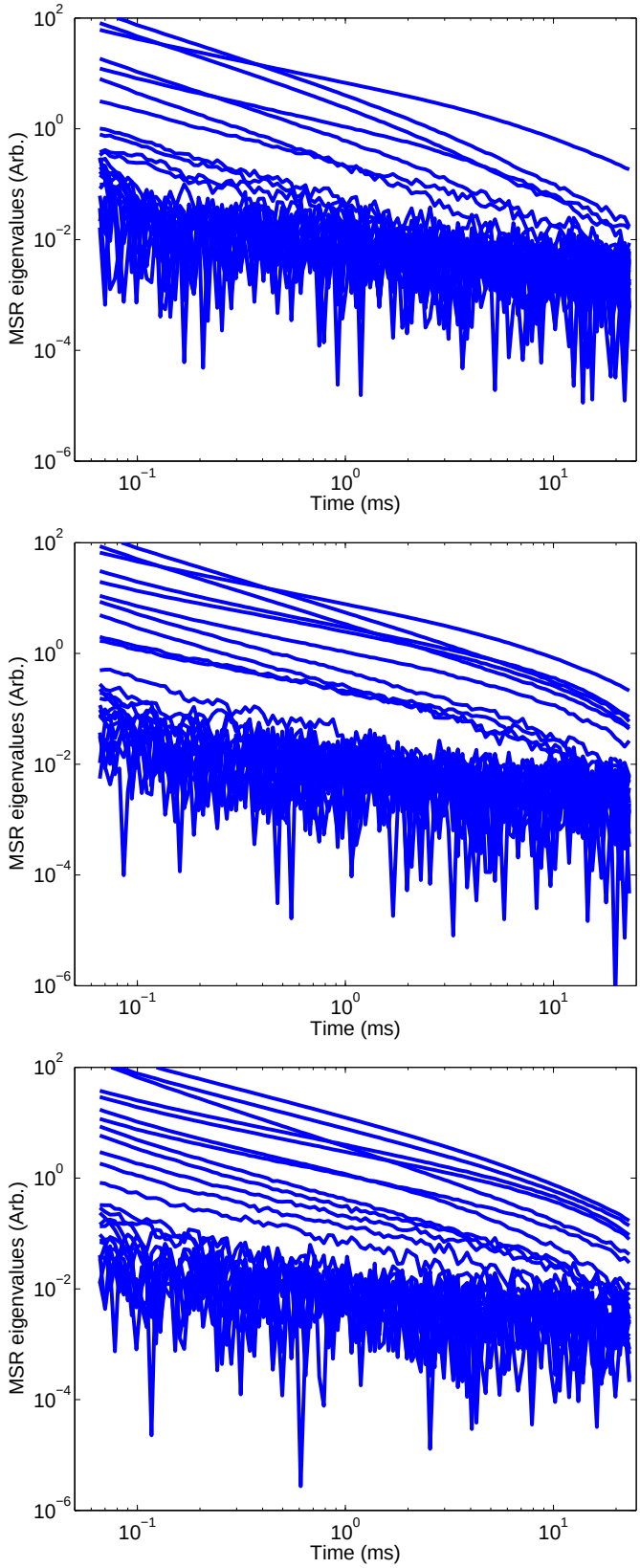

Figure 4.16: MSR eigenvalues of the test-stand measurement as the munitions of the sphere and spheroid (c) of Fig. 4.13.

There were three above-noise eigenvalues in each case, revealing the presence of one target. The howitzer shell of Fig. 4.17(upper) (the large TOI in the test-stand experiment described above) is buried 55 cm below ground, while the HEAT round in Fig. 4.17(middle) is 62 cm deep. The signal from the latter is weaker because of the greater depth, despite the lower noise level (which, in the case of Camp Butner, varied substantially from cell to cell). The slow decay of the eigenvalues indicates that these are large targets with substantial metal content [82]. Two of the eigenvalues are again seen to be roughly parallel, and in the case of the shell they overlap each other. The behavior of the other (non-parallel) above-threshold eigenvalue allows preliminary classification of the target. Fig. 4.17(lower) shows the eigenvalue decay curves (computed using both JD and constrained nonlinear optimization) for the HEAT round as measured by TEMTADS in the APG test stand of the previous section; the munition was 53 cm below the sensor center in that case. The time decay in Fig. 4.17(middle) resembles this measurement more than it does the other cell.

Typical instances of the other Camp Butner TOI, the two different kinds of 37-mm projectiles, are shown along with their time-dependent eigenvalues in Fig. 4.18. The signal in Fig. 4.18(upper) is strong and distinct, reflecting the shallowness of the target (it is only 8 cm deep). The copper driving band, with its high conductivity, influences the signal by retarding its decay. The signal in Fig. 4.18(lower) is much weaker, as the target has a larger depth, but it has three time-dependent eigenvalues that are distinct from the noise, whose level is similar to that of Fig. 4.18(upper), through the whole decay.

Figure 4.19(upper) depicts the result of running JD on a cell that contained a fuze and a small detonation fragment, both located 16 cm below the surface, while Fig. 4.19(lower) does the same for a single fuze buried almost twice as deep at 28 cm. In both cases, only three eigenvalue decay curves are above the noise threshold, indicating that the targets in each cell can be represented by a single source. The JD analysis in Fig. 4.19(upper) case fails to identify the small fragment, which was located close to the fuze. In Fig. 4.19(lower) there are still three dominant eigenvalues, but the low signal-to-noise ratio makes them barely discernible. The shape information given by JD was crucial in helping to identify this target correctly. Here, as in all real-world situations, the noise is due simultaneously to the ground, which can be magnetically responsive or wet (or both), to the sensor, and to objects too small or distant to produce detectable individual signals but whose collective response may be significant. Again it is seen that the MSR eigenvalues mix positional information with intrinsic response: small, shallow targets and large deep objects produce time-dependent eigenvalues of comparable magnitudes.

In Fig. 4.20 we have a large, shallow sample of "cultural" (i.e., not-ordnance-related) debris: a plowshare with depth of only 7 cm. The eigenvalues are quite large, as expected, but decay very fast in time, indicating that this is not a TOI. The final two figures correspond to multi-target scenarios. In Fig. 4.21(upper) we have the extracted eigenvalues corresponding to a set of fragments of a 155-mm munition buried at a depth of 50 cm. Two sources suffice to describe the objects. Figure 4.21(lower) depicts the contents and data of a veritable multi-target cell, with several explosion byproducts at a wide assortment of depths. The resulting eigenvalue map can immediately alert operators that there may be several potentially dangerous targets interred below and warn analysts from the outset that any inversion to be performed must involve a forward model that assumes many targets. (Methods to transmit this information could be incorporated into the sensor, and those cells will always be dug out.)

The results of the Camp Butner blind test were scored independently by the Institute for Defense Analyses [80, 81]. We correctly characterized all of the 2290 anomalies, each containing at

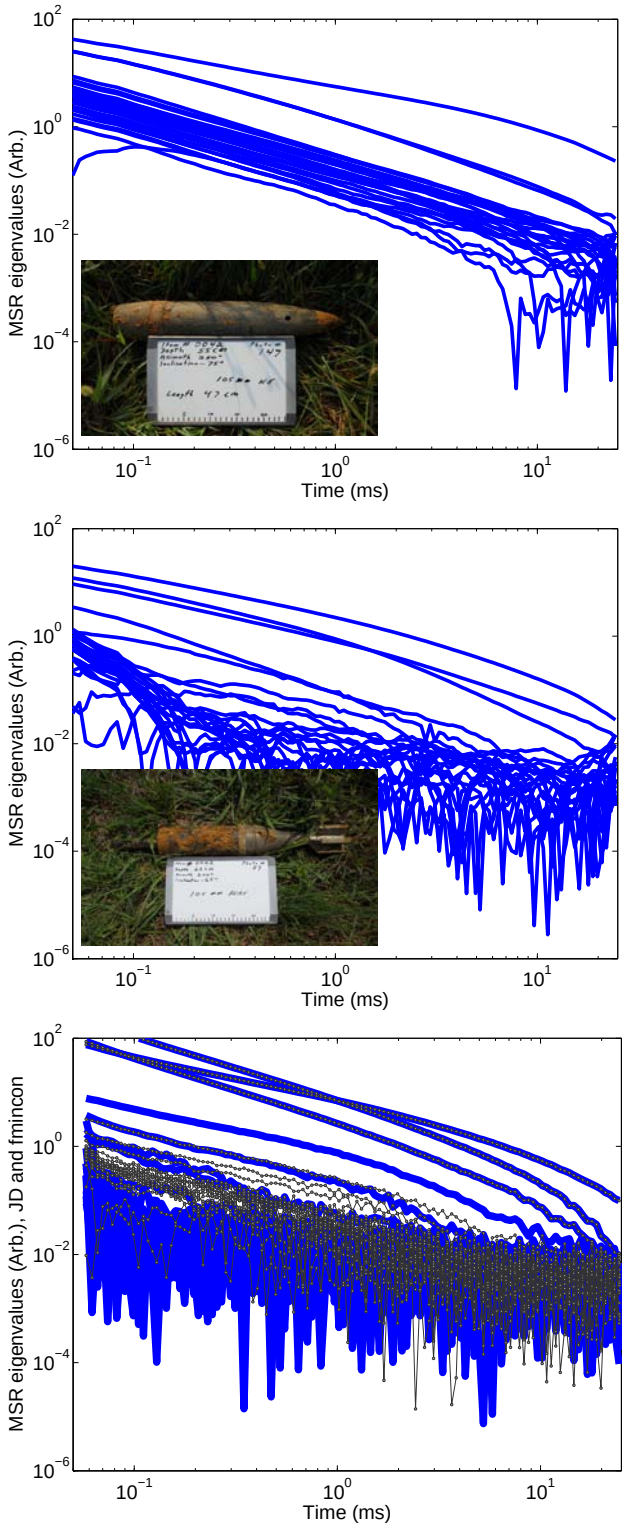

Figure 4.17: (upper) MSR eigenvalues for Camp Butner Cell 42, which contained a 105-mm HE shell buried at a depth of 55 cm. (middle) MSR eigenvalues for Camp Butner Cell 62, containing a 105-mm HEAT round buried at 62 cm. (lower) MSR eigenvalues for a 105-mm HEAT round placed 53 cm below TEMTADS in the APG test stand, computed using JD (solid lines) and nonlinear constrained optimization (dots).

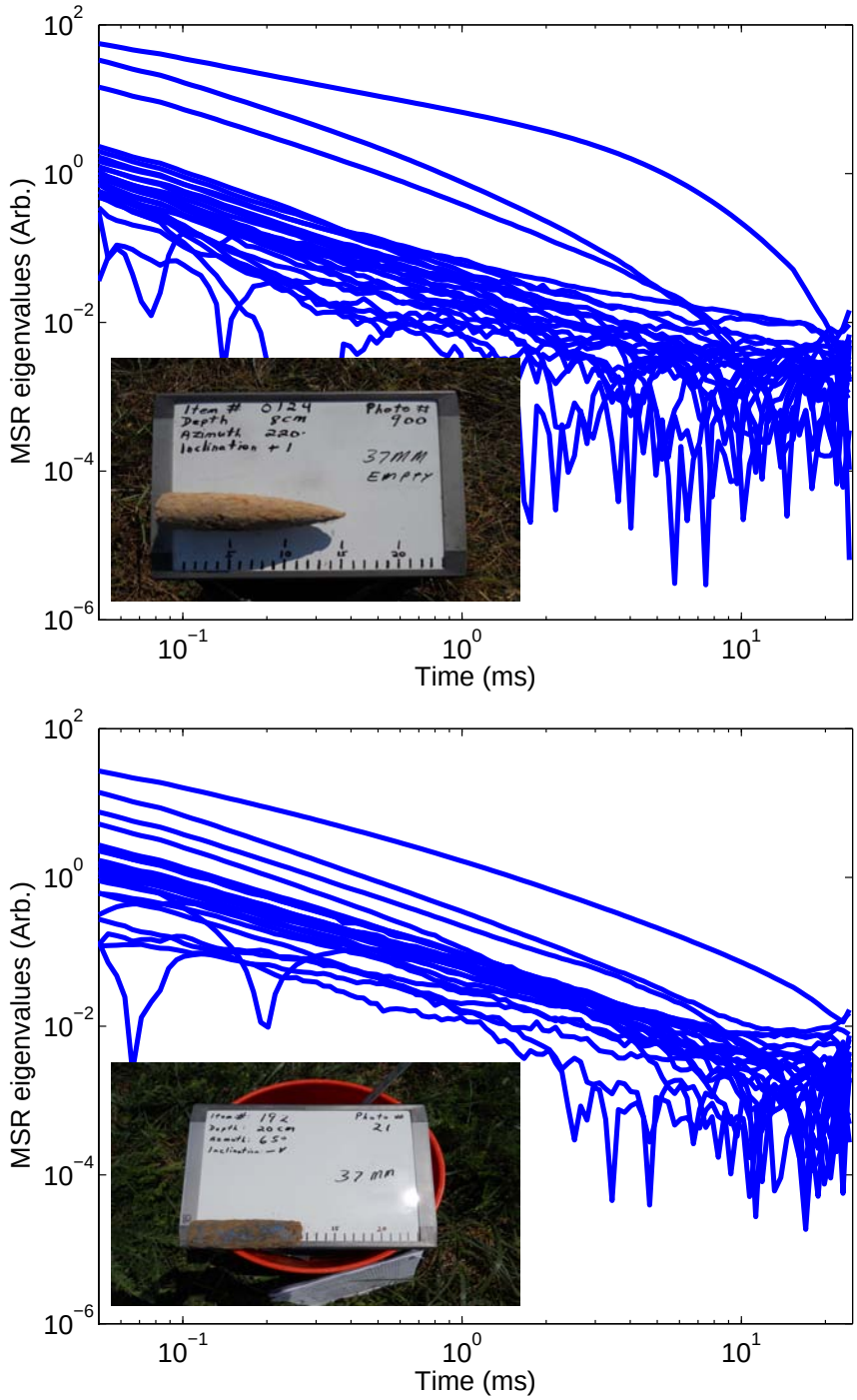

Figure 4.18: (upper) MSR eigenvalues for Camp Butner Cell 124, with one kind of 37-mm projectile at 8 cm below ground. (lower) MSR eigenvalues for Camp Butner Cell 192, which contained the other kind of 37-mm projectile, this one at a depth of 20 cm.

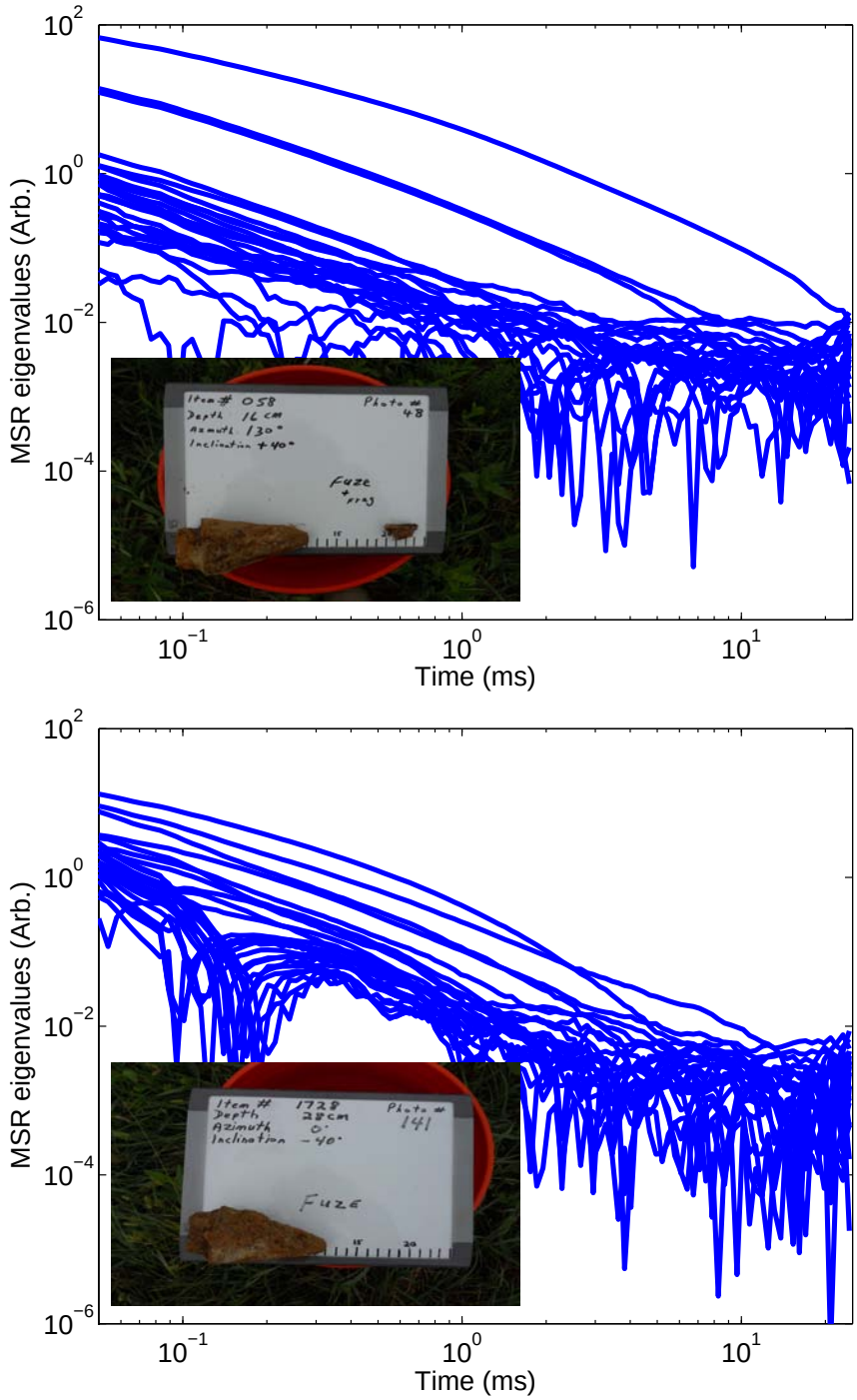

Figure 4.19: (upper) MSR eigenvalues for Camp Butner Cell 58, which contained two explosion byproducts, a fuze and a shrapnel fragment, at a depth of 16 cm. (lower) MSR eigenvalues for Camp Butner Cell 1728, which contained another fuze (buried 28 cm below ground).

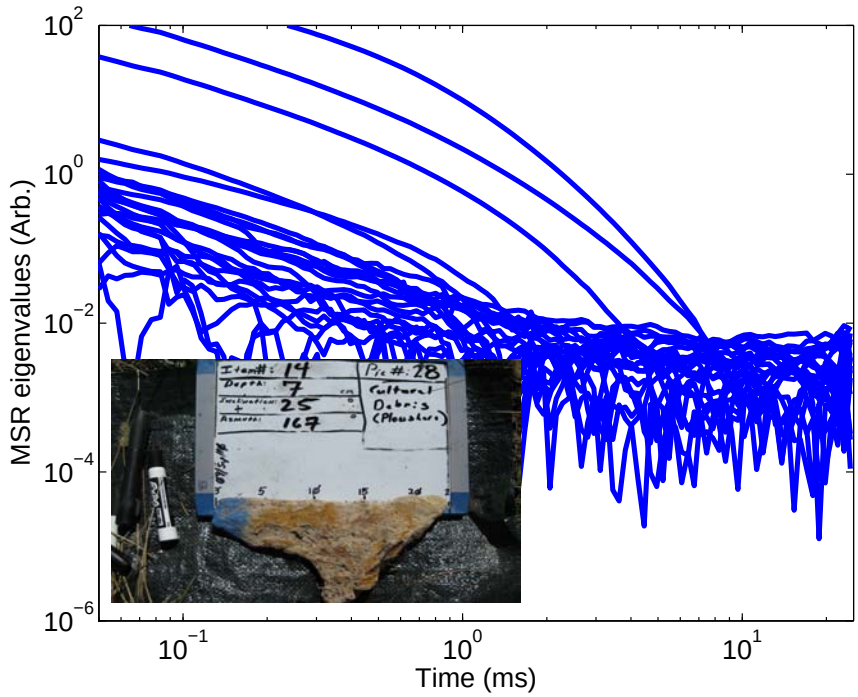

Figure 4.20: MSR eigenvalues for Camp Butner Cell 14, with a sizable plowshare buried at 7 cm.

least one target, for which data were provided. All of the 171 potentially dangerous targets were identified as such and also classified by caliber, and our algorithms moreover discerned between the two kinds of 37-mm projectiles and distinguished the 105-mm HEAT rounds from the other 105-mm shells. We asked for 116 targets to be dug before we were sure that we had identified all the TOI; in contrast, the best analysis using the dipole model required 63 extra digs to reach that level, while other procedures needed many more false alarms to be unearthed and in some cases failed to identify UXO [81]. One of the stated objectives of the Camp Butner test was to "pave [. . .] the way for reduced costs and an accelerated timeline to remediate munitions-contaminated sites throughout the nation" [79]. The success of our procedure gives an idea of the progress that has been made toward fulfilling this aim.

4.3.d Conclusion

In this section we applied a procedure based on joint diagonalization that provides a fast and reliable inversion-free estimate of the number of targets buried under an EMI sensor. The number of targets can then be input into multi-target inversion procedures, which work much faster and more reliably when given this information. The eigenvalue decay curves found by JD have amplitudes that depend on the location and orientation of the targets, but their shapes, including the appearance of parallel curves for cylindrically symmetric targets, are independent of those particulars. We reiterate that the JD procedure cannot replace inversion, which is still necessary because the depths at which the targets are buried must be known so they can be dug out safely; better knowledge of the locations, moreover, allows better determination of the intrinsic signatures of the targets and consequently more robust and reliable identification and classification.

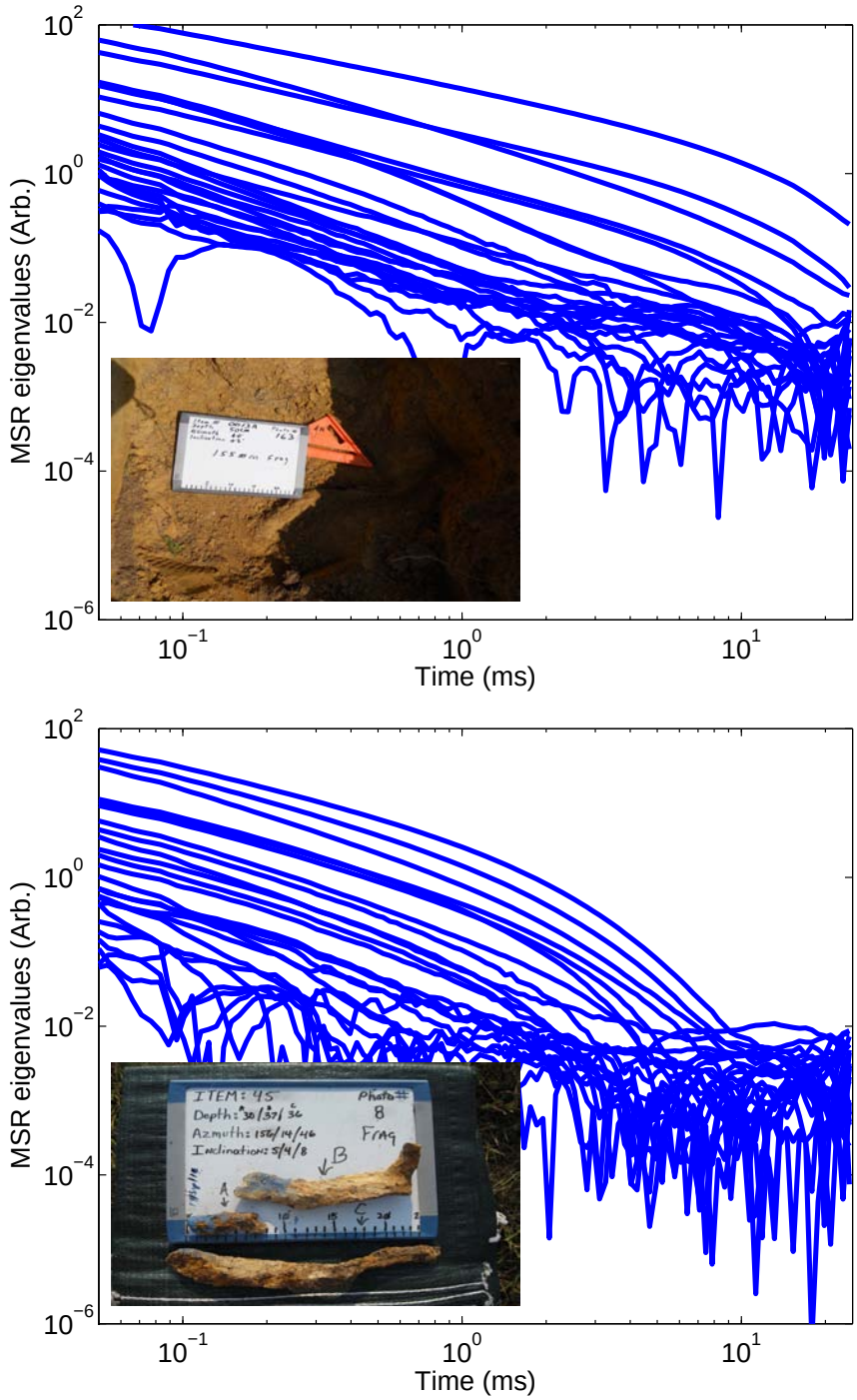

Figure 4.21: (upper) MSR eigenvalues for Camp Butner Cell 13, containing fragments of a 155-mm projectile, buried 50 cm below ground. (lower) MSR eigenvalues for Camp Butner Cell 45, containing several fragments, buried at several depths, of a munition that exploded.

The JD technique has several other potential uses, which we have started to pursue. It could be used, for example, to remove noise from data by removing the smaller extracted eigenvalues and their corresponding eigenvectors. At the other end, removing the *larger* eigenvalues and eigenvectors could make it possible to resolve smaller or deeply buried objects. (For these applications it is critical to associate each of the eigenvalues with a single eigenvector.) In addition, a JD analysis performed in the field can immediately alert data collectors about the noise level, which can then be adjusted by having TEMTADS sample signals for a longer time.

Our aim has been to introduce the JD algorithm and its application to a particular sensor, the TEMTADS array, whose design features make the JD implementation particularly transparent. We have adapted the JD technique to other EMI instruments—the Geometrics MetalMapper and a 2×2 portable version of TEMTADS—and in the future we will present the results obtained for blind tests carried out with these tools. We note that further development of the method, generalized for nonsymmetric and nonsquare MSR matrices, may require the use of a *joint SVD* algorithm, with two sets of shared vectors instead of one [83].

4.4 The Orthonormalized Volume Magnetic Source Model for Discrimination of Unexploded Ordnance

In this section, we present a new physically complete, fast, and accurate numerical technique for the solution of electromagnetic induction sensing problems called the orthonormalized volume magnetic source (ONVMS) model. The model assumes that the secondary magnetic field picked up by the sensor originates from a set of magnetic dipole sources distributed over a volume that coincides with the interrogated area. The Green functions associated with the responding sources are turned into an orthonormal basis using a generalization of the Gram-Schmidt method, enabling one to determine the sources' strengths directly from measured data without having to invert large and potentially ill-conditioned matrices. The method extends naturally to the treatment of multi-target cases. Several examples are presented to illustrate the applicability of the method in the discrimination of unexploded ordnance (UXO). In particular we analyze data taken by the TEMTADS sensor array at a test stand and during a blind test administered at a UXO live site. The method is highly successful in distinguishing UXO from among other UXO and from accompanying clutter.

4.4.a Introduction

The UXO cleanup problem has three stages: detection, inversion, and classification [84]. Detection of UXO can be considered a binary-hypothesis problem in which one must determine whether there are objects present or not. Great strides have been made on this first stage by the introduction of a series of sophisticated ultrawideband sensors designed to increase detection probability. These devices work in the electromagnetic induction (EMI) range of frequencies, which extends from tens of Hz to just under 100 kHz, and can collect time-domain [73, 85, 86] or frequency-domain [87–89] geophysical data of remarkable richness and diversity. State-of-the-art EMI sensors are capable of recording target responses, whether in scalar [85, 87, 90] or vector form [2, 3, 88, 91], with unprecedented spatial resolution and a spectral range that allows a rather complete characterization of buried objects. One such instrument is the Time-Domain Electromagnetic Multisensor Towed Array Detection System (TEMTADS), sketched in Fig. 4.10 and described in Sec. 4.3.b.(1), which took the data we analyze here.

At the final stage of the process it is necessary to classify the detected objects as UXO or clutter and, if the former, to determine the type of ordnance to which they belong. This classification step has been the subject of extensive investigation and has involved resources and tools from such varied fields as nonparametric statistics, neural networks, and statistical learning, resulting in the use of maximum likelihood methods, mixed models, support vector machines, and linear, quadratic, or Mahalanobis distance classifiers, among other approaches [24, 63, 92–96].

Between detection and classification it is necessary to perform the second step of the process, wherein the raw data provided by the sensor are inverted and turned into features intrinsic to each target that can be used as inputs to the classifier of choice. This inversion step, on which we concentrate in this Sec. 4.4, must determine the locations and orientations of the objects under interrogation simultaneously with their electromagnetic signatures. Most current inversion approaches are based on the isolated point dipole model or some variation thereof [8, 24, 62, 64, 97–99]. Those schemes use a magnetic polarizability tensor to parameterize the target response as part of a model vector that also contains positional information.

The extensive use of the dipole approximation to characterize scatterers is motivated by its speed and simplicity. However, the model reduces a target to a point and assumes that the primary (exciting) field of the sensor striking an object is essentially uniform throughout its extent. These simplifications, understandable though they may be, render the model physically incomplete and frequently make it break down under realistic field conditions [81]. A multi-source model should provide a better description of a target, since it may incorporate heterogeneity and take into account the significant variations of magnetic fields over lengths on the order of centimeters. Moreover, the situation in the field often involves two or more targets sharing a measurement cell and producing a composite signal with overlapping components, and any model used to analyze UXO data must incorporate this possibility transparently.

This Sec. 4.4 presents a new, physically complete, fast, accurate, robust, and clutter-tolerant inversion procedure that has performed quite well in several live-site blind tests. The procedure starts from the assumption that the measurable secondary field is radiated by a set of elementary dipole sources infused throughout a volume at a set of singular points [55]. The Green functions that connect these sources with the measured field are turned into an orthonormal basis to streamline the calculations. The spatial distribution of the responding dipoles (their amplitudes scaled by the primary field) traces a map of "response activity" that reveals the targets below. This orthonormalized volume magnetic source (ONVMS) model, of which a previous presentation [82] is available, is thus a generalization of the dipole model that simultaneously allows for the presence of several targets in the field of view of the sensor and for the possibility that one or more of the targets is of such complexity—by being large or heterogeneous, for example—that it needs more than one dipole to account for the spatial or temporal nuances of its response. Other models conceived along the same lines spread a continuum of elementary dipoles over a surface that surrounds the object [100] or decompose the primary field into standardized excitation modes and synthesize the target response as a superposition of catalogued responses to these modes [101, 102]. Those models usually require at each step the solution of a large system of linear equations that often is numerically ill-conditioned. The procedure we use here must also invert matrices, but these are never large and are always well behaved; this makes the method much faster and the resulting electromagnetic fingerprints more robust and noise-tolerant, all of which are desirable features.

The need to determine the locations of the sources as well as their intrinsic features results in a computationally costly nonlinear inversion in which one defines an objective function that

provides a measure of the misfit between predictions and measurements and performs a least-squares minimization. These objective functions tend to have many local minima, resulting in incorrect predictions. There is a procedure that uses elementary sources to locate a singularity directly [103], but its generalization to multi-target scenarios is not straightforward. In this work we recover the time-dependent ONVMS amplitudes and the geometric information by employing a two-step inversion approach that combines the procedure described in the next section with differential evolution (DE), a continuous genetic algorithm [104, 105] that has already been applied to UXO discrimination in conjunction with other models [28, 106]. The procedure alternates between linear ONVMS time-dependent-amplitude determinations and DE location searches, iterating until it reaches convergence.

4.4.b Methods

Consider a set of permeable and highly conducting metallic objects placed in a time-varying primary magnetic field. In the EMI frequency regime all displacement currents are negligible, and moreover we assume that the soil and air are of negligible conductivity and thus neglect any currents flowing outside the metallic objects. The primary magnetic field penetrates the targets to some degree, inducing eddy currents and magnetic response inside them, and in turn the induced sources produce a measurable secondary magnetic field outside the objects. The integral equation for the magnetic field allows us to represent this secondary field as originating from a set of M infinitesimal dipolar sources distributed over a volume. For the time being we assume that we know the locations $\mathbf{r}'_k$, $k = 1, \ldots, M$, of the sources; this condition is eventually relaxed, and the locations found by optimization. The strength of each source, once the primary field at its location is factored out, is contained in a 3 ×3 symmetric polarizability tensor [64, 97, 99, 107] that can be stretched out into a vector (denoted here as $\mathbf{m}$). The secondary field due to the i-th source can be expressed at any observation point $\mathbf{r}$ as the matrix-vector product

$$\mathbf{H}_i(\mathbf{r}) = G_i(\mathbf{r})\mathbf{m}_i, \tag{4.4.1}$$

where the Green function G_i is given in detail in Appendix A.5. When there are several such sources, the total field can be expressed as a superposition:

$$\mathbf{H}(\mathbf{r}) = \sum_{i=1}^{M} G_i(\mathbf{r})\mathbf{m}_i = \begin{bmatrix} G_1 & G_2 & \cdots \end{bmatrix} \begin{bmatrix} \mathbf{m}_1 \\ \mathbf{m}_2 \\ \vdots \end{bmatrix}. \tag{4.4.2}$$

Before going further we note that our method takes as input the (in principle unknown) number M of radiating sources. It is possible to proceed by letting M vary as part of an optimization routine, just as we do here to determine the sources' locations, but that lies outside the scope of this Sec. 4.4. We have developed a procedure based on joint diagonalization [71, 108] that estimates M starting from raw data and with no need for inversion. That technique (henceforth referred to as JD) is presented in detail in [109], and unless otherwise noted we use it to estimate M in what follows.

The superposition (4.4.2) can be used to carry out one- and multi-object inversions starting from data taken at an ensemble of points. All the measured $\mathbf{H}$-values—which can pertain to multiple transmitters, multiple receivers, changing sensor locations, and different vector components—are strung together in a one-dimensional array, while the corresponding Green functions are stacked as

matrix rows. The resulting composite G matrix can then be (pseudo)inverted to find the strengths of the sources. This procedure, which is nothing other than the dipole model if each body is taken to be represented by one source only, works well for one or two sources, but for larger numbers becomes very time-consuming (since the Green matrix becomes very large) and increasingly ill-posed, usually requiring regularization [3, 69, 110]; furthermore, those models unphysically neglect the coupling between adjoining targets and between different sections of a heterogeneous object. The ONVMS method is designed to circumvent these difficulties.

The procedure starts from the realization that the matrix-vector product (4.4.1) is valid at any observation point $\mathbf{r}$, and in particular at every point $\mathbf{r}_s$ on the plane surface delimited by the TEMTADS array (see Fig. 4.10). If we introduce the inner product

$$\langle A,B\rangle = \int_S A^T B ds = \int_{\mathrm{Rx}_0} A^T B ds + \int_{\mathrm{Rx}_1} A^T B ds + \cdots, \tag{4.4.3}$$

where the integral is computed over the "sensitive" surfaces of the sensor (which are contiguous in the case of TEMTADS, but not necessarily for other instruments), and if furthermore we can find a basis of Green functions orthogonal under this measure,

$$\mathbf{H}(\mathbf{r}_s) = \sum_{j=1}^{M} \Psi_j(\mathbf{r}_s)\,\mathbf{b}_j \text{ such that } \left\langle \Psi_j, \Psi_k \right\rangle = F_j \delta_{jk}, \tag{4.4.4}$$

where δ_{jk} is a Kronecker delta, then it is possible to find the source amplitudes $\mathbf{b}_j$ without costly and ill-conditioned inversions simply by exploiting the sifting property of the orthogonal basis:

$$\langle \Psi_k, \mathbf{H}\rangle = \sum_{j=1}^{M} \left\langle \Psi_k, \Psi_j \right\rangle \mathbf{b}_j = \sum_{j=1}^{M} F_k \delta_{kj} \mathbf{b}_j = F_k \mathbf{b}_k andthus \mathbf{b}_k = F_k^{-1} \left\langle \Psi_k, \mathbf{H} \right\rangle, \tag{4.4.5}$$

which clearly does not involve solving a large linear system of equations; it is necessary to invert only the 6 ×6 matrix F_k. Moreover, this definition of the coefficients $\mathbf{b}_j$ guarantees that they are "optimal" in the sense that the expansion (4.4.4) yields the least mean-square error $\langle \mathbf{\Delta}_M, \mathbf{\Delta}_M \rangle$, where $\mathbf{\Delta}_M = \mathbf{H} - \Sigma_{j=1}^{M} \Psi_j \mathbf{b}_j$ [111].

To construct the set of orthonormal Green functions we resort to a generalization of the Gram-Schmidt procedure [112, 113]. Assuming that the Green matrices are linearly independent—i.e., that we cannot have a collection of distinctly located dipole sources combining to produce no measurable field unless their amplitudes all vanish—we define

$$\begin{aligned} \Psi_1 &= G_1, \\ \Psi_2 &= G_2 - \Psi_1 A_{21}, \\ &\vdots \\ \Psi_m &= G_m - \sum_{k=1}^{m-1} \Psi_k A_{mk}, \\ &\vdots \\ \Psi_M &= G_M - \sum_{k=1}^{M-1} \Psi_k A_{Mk}, \end{aligned} \tag{4.4.6}$$

where the 6×6 matrices A_{jk} obey $A_{jk} = 0$ for $j \leq k$. Enforcing the orthogonality relation (4.4.4) is equivalent to setting $\langle \Psi_n, G_m \rangle = F_n A_{mn}$ for $n < m$, and using this relation twice in definition (4.4.6) we find that

$$A_{mn} = F_n^{-1} \left(C_{nm} - \sum_{k=1}^{n-1} A_{nk}^T F_k A_{mk} \right), \tag{4.4.7}$$

where the overlap integral $C_{mn} = \langle G_m, G_n \rangle$.

At the end of the process it is necessary to recover an expansion expressed, like (4.4.1), in terms of the actual Green functions, in part because the functions Ψ_j are orthogonal (and defined) only at points on the receivers, and in part because of the nonuniqueness of the coefficients $\mathbf{b}_j$ due to the arbitrary order in which the G_j enter the recursion (4.4.6). To that end, we express

$$\Psi_m = \sum_{k=1}^{m} G_k B_{mk}, \tag{4.4.8}$$

and to find the coefficients B_{mk} we compare expansion (4.4.8) term by term to the definition (4.4.6) and use the rule that $A_{jk} = 0$ for $j \leq k$ to find

$$\begin{aligned} B_{mm} &= I, \text{ the identity,} \\ B_{m(m-1)} &= -A_{m(m-1)}, \\ B_{mq} &= -\sum_{l=q}^{m-1} B_{lq} A_{ml} \text{ for } 1 \leq q \leq m-2, \end{aligned} \tag{4.4.9}$$

in terms of which we recover the physical polarizability elements:

$$\begin{aligned} \mathbf{H} &= \sum_{k=1}^{M} \Psi_k \mathbf{b}_k = \sum_{k=1}^{M} \left(\sum_{l=1}^{k} G_l B_{kl} \right) \mathbf{b}_k \\ &= \sum_{l=1}^{M} G_l \left(\sum_{k=l}^{M} B_{kl} \mathbf{b}_k \right) = \sum_{l=1}^{M} G_l \mathbf{m}_l \end{aligned} \tag{4.4.10}$$

With all the pieces in place, we can sketch an algorithm to invert EMI data using the ONVMS model:

1. Given a number of sources and their tentative locations, find the Green tensors G_i using (A.5.5) and compute the overlap integrals G_{mn} using the inner product (4.4.3).

2. Determine the first normalization factor, $F_1 = \langle G_1, G_1 \rangle$, and use it to find all the Gram-Schmidt coefficients A_{mn} with $n = 1$: $A_{m1} = F_1^{-1} C_{1m}$.

3. Set $m = 2$; compute, in sequence,

   (a) The coefficients A_{mn} with $n = 2, \ldots, m-1$ using (4.4.7);

   (b) The function Ψ_m using the expansion (4.4.6);

   (c) The normalization factor $F_m = \langle \Psi_m, \Psi_m \rangle$;

   increase m by 1 and iterate until all sources have been included.

4. Once all the A_{mn}, F_m, and Ψ_m are known, find B_{mq} using (4.4.9).

5. Use the orthonormality of the new Green functions to determine the source amplitudes using $\mathbf{b}_q = F_q^{-1}\left\langle \Psi_q, \mathbf{H}^{\text{data}} \right\rangle$, as in (4.4.5). Take the measured field to be piecewise constant—i.e., constant throughout each receiver—when evaluating the integrals.

6. Use the computed $\mathbf{b}_q$, B_{mq}, and G_m, along with the expansion (4.4.10), to generate the secondary field prescribed by the given number of sources at the given locations.

7. Compare the model prediction with the measured data, vary the source locations, and iterate until the least-squares discrepancy between prediction and measurement attains a suitable minimum.

The procedure as written applies to only one time gate, but the extension to fully time-dependent functions is straightforward: we need only substitute the vectors $\mathbf{b}_q$ and $\mathbf{H}^{\text{data}}$ for two-dimensional arrays where the columns denote time. The relations between the two, namely (4.4.5) and (4.4.10), acquire multiple right-hand-sides, and the optimization mentioned on Step 7 of the algorithm is constrained further. As a final remark we note that rigorously speaking the coefficients $\mathbf{b}_q$ (and, for that matter, the amplitudes $\mathbf{m}_k$) are *not* the polarizabilities themselves but, in accordance with Faraday's law, relate more closely to their time derivatives [64, 113].

4.4.c Results

The ONVMS technique in principle does not provide more information than its one-source reduction, the standard dipole model. Both inversion procedures generate estimates of the locations and orientations of the interrogated targets and produce three time-decay curves per object, one for each of its principal axes; the decay profiles, moreover, are similar because they reflect the same underlying EMI phenomenology. The difference is not in the quantity of information, then, but in its quality. The electromagnetic signatures generated by ONVMS are more consistent, from sample to sample of a given kind of object, than the polarizability elements given by the dipole model. The improved fidelity to the phenomenology—due to the possibility of using more than one source to describe a target when necessary, and letting these sources interact, all while avoiding numerical ill-conditioning—allows the method to make more reliable predictions in the presence of noise. Moreover, the ONVMS model treats single- and multi-object scenarios on the same footing, easing the decoupling of overlapping signals due to clustered targets—an occurrence that tends to stump other analysis tools [81]. Finally, all of these improvements in accuracy are attained without sacrificing speed—the procedure is in fact faster because the matrices that have to be inverted are always smaller.

The strongest confirmation that ONVMS is an accurate and reliable inverse model comes from real-world experience. The method has consistently outperformed its rivals in a battery of blind discrimination tests conducted by the Environmental Security Technology Certification Program (ESTCP) at actual UXO live sites. These tests, of which the first two took place in 2007 at Camp Sibert in Alabama [33] and in 2009 at Camp San Luis Obispo in California [114], have been designed to showcase the progress made in the quest to make UXO remediation more efficient and cost-effective. Each test is more realistic than the previous one, and thus more taxing on hardware, software, and human analysts. In this Sec. 4.4 we concentrate on the results obtained by

the ONVMS method in the third test—held at Camp Butner in North Carolina—but first we review a more idealized experiment that highlights the power and flexibility of the procedure.

4.4.c.(1) A Test-Stand Experiment The experiment described in this section was designed to act as a benchmark for multitarget scenarios without the complications that arise in the field. The measurements were performed by personnel from Nova Research, Inc. at their Blossom Point, MD test stand on 15 January 2010. The setup is described in Sec. 4.3.c.(1) and shown schematically in Fig. 4.24(d).

Figure 4.22 shows the result of the JD analysis and the ONVMS inversion of a measurement involving only the 105mm shell. The target is lying flat, with its nose pointing in the $\hat{\mathbf{x}}$-direction, directly underneath the center of TEMTADS on a platform 63 cm below the sensor. The multi-static response (MSR) matrix [109] of panel (a) has three dominant eigenvalues (out of a total of 25) and four more that stand out from the noise but are much smaller, indicating the presence of a single (though possibly large) target and providing a starting point for the ONVMS inversion. (The MSR eigenvalues have been divided by a factor of 10 to keep the axes consistent; they incorporate positional information and cannot be readily compared with the ONVMS amplitudes, even if they show similar patterns.)

The ONVMS procedure with one dipolar source locates the target center at $(2\hat{\mathbf{x}} - 60\hat{\mathbf{z}})$ cm with its dipole moment pointing in a direction lying on the xz plane and making an angle of 11°with the horizontal (Appendix A.5 explains how the target orientation is estimated); the corresponding ONVMS amplitude is shown in panel (b). This characterization, while reasonable, is not completely satisfactory for this straightforward measurement, particularly since EMI phenomenology dictates that objects with azimuthal symmetry, like most UXO, should have two (transverse) polarizability elements that resemble each other closely and differ markedly from the (longitudinal) third [100].

A two-source inversion, shown in panel (c), improves the fit to the measured data and clarifies the interpretation. Now the sources are at $(18\hat{\mathbf{x}} - 59\hat{\mathbf{z}})$ cm and $(-6\hat{\mathbf{x}} - 59\hat{\mathbf{z}})$ cm, right along the symmetry axis of the projectile and within 1 cm of the true depth, and their dipole moments are aligned with the x-axis to within 5°. (The actual shell has diameter 10.5 cm and is 46.5 cm long.) Of interest is the section with the larger response, which corresponds to the posterior end of the projectile: the hump seen in the late-time response of the dominant element signals the presence of a copper driving band, a fact that has been noted before [81, 115]. If we simply add the two effective polarizabilities algebraically without factoring in their estimated locations we obtain the electromagnetic signature of panel (d), which is seen to have the same scale as the single-source profile of (b) but now clearly exhibits the cylindrical symmetry of the target. Note, however, that the essence of the dominant longitudinal ONVMS amplitude is already captured well by the one-target inversion.

Next the 60mm mortar round is added. The projectile, whose diameter and length are respectively 6 and 24.5 cm, rests on a platform located 38 cm below the sensor and is parallel to the 105mm shell and displaced 40cm from it in the $-\hat{\mathbf{y}}$direction. The nonzero multi-static response eigenvalues shown in panel (a) of Fig. 4.23 suggest the presence of at least two objects, so we carry out both a two-source and a three-source ONVMS-DE inversion. As panel (c) shows, the two-source inversion stabilizes well before the end of a 100-iteration DE run; the three-source inversion requires more than 100 iterations but is done by 150. Just one source located at $(-40\hat{\mathbf{y}} - 40\hat{\mathbf{z}})$ cm suffices to describe the smaller target. Panel (b) also shows the result of a single-source inversion

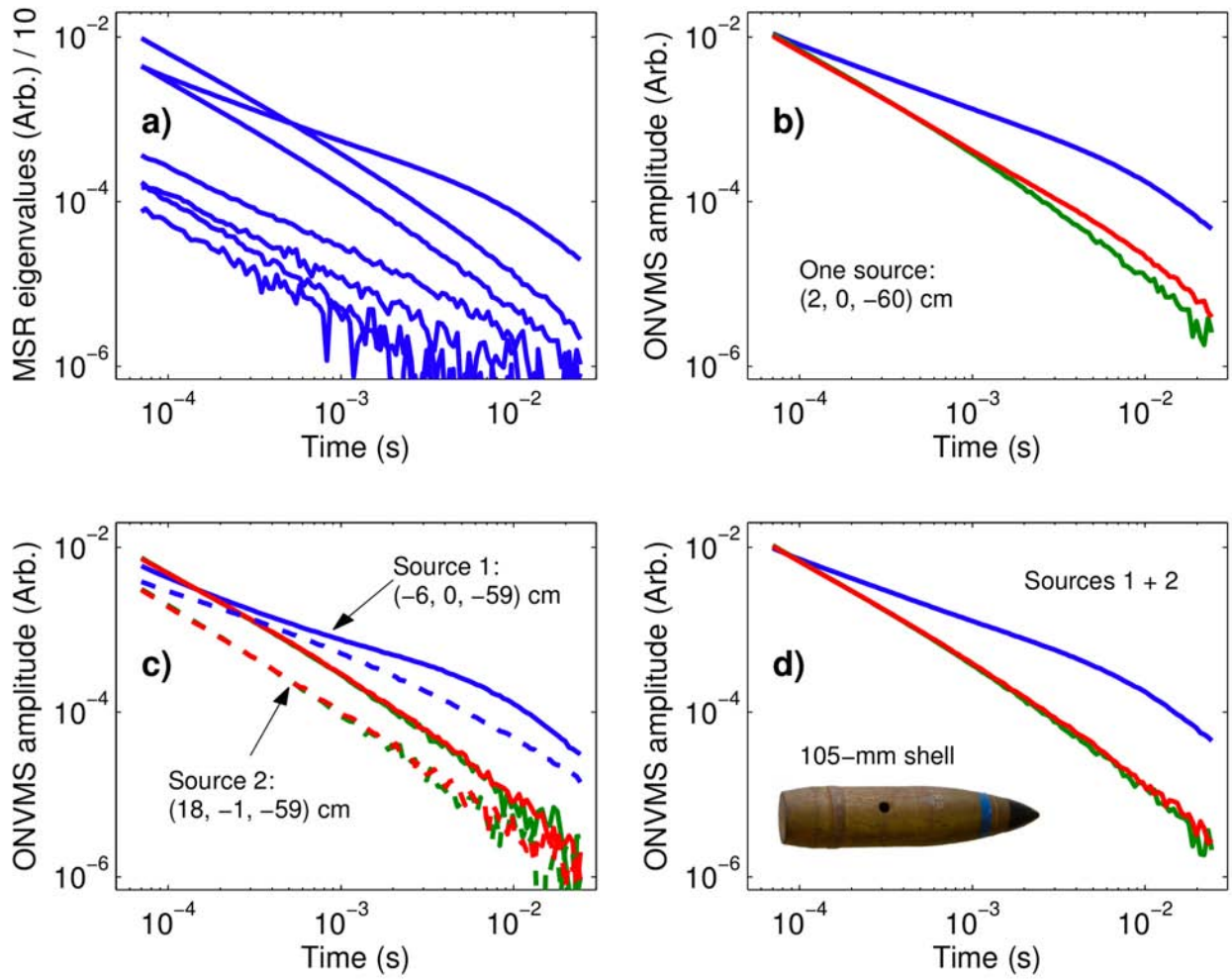

Figure 4.22: ONVMS inversion of a measurement involving one large TOI. The target is a horizontal 105mm howitzer shell lying 63 cm below the center of the TEMTADS sensor array and pointing in the $\hat{\mathbf{x}}$-direction. (a) The eigenvalues of the multistatic response matrix suggest that there may be one target. (b) A single-source inversion locates the object well and describes it reasonably, but does not reveal explicitly its cylindrical symmetry. (c) A two-source inversion describes the target as composed of two sections located along its axis of symmetry and hints at the presence of a copper driving band. (d) Simply adding the ONVMS amplitudes of the two sources restores the cylindrical symmetry of the target.

carried out on the 60mm round, again at a nominal depth of 38 cm but resting below the center of TEMTADS; there is noticeable case-to-case consistency between the time-decay profiles.

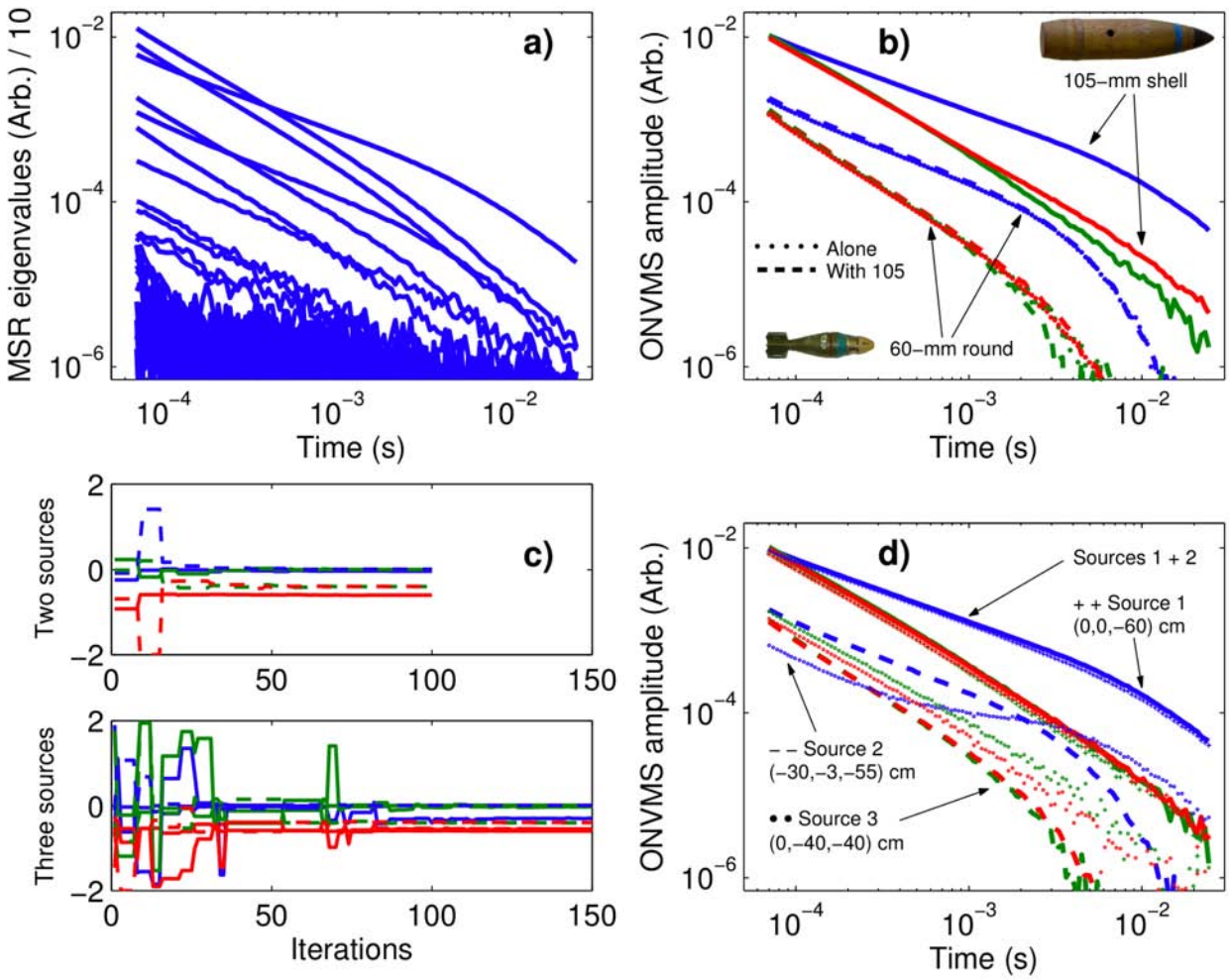

Figure 4.23: Two-target inversion with the ONVMS model. The targets are the 105-mm shell of Fig. 4.22 and a 60-mm mortar round. (a) The eigenvalues of the MSR matrix indicate the presence of a least two targets. (b) Inversion using two dipole sources. Again, one source does not suffice to fully characterize the large target. The small target is identified better: overlaid is the ONVMS amplitude for a measurement involving only the 60mm (albeit at a different location). (c) The two-target inversion stabilizes after only 50 iterations; a three-target inversion, shown in (d), requires close to 150. (d) Using two sources to describe the large target recovers its cylindrical symmetry. Again the sources all point in the $\hat{\mathbf{x}}$-direction, as do both targets.

Again we see that two sources are needed to characterize the 105mm shell completely, with the insufficiency seen as a failure to exhibit the cylindrical symmetry. The sources combining to form the 105mm are located at $-60\hat{\mathbf{z}}$ cm and $(-30\hat{\mathbf{x}} - 3\hat{\mathbf{y}} - 55\hat{\mathbf{z}})$ cm. The source corresponding to the posterior end of the 105mm again has the hump due to the driving band (whose particular geometry and nonferromagnetic nature tend to require a separate source), but is seen to be weaker, and at a different location, than when the projectile was interrogated by itself; the method does not

simply report the linear superposition of the different dipolar sources but also incorporates their interaction.

We have seen that the method can resolve targets of interest whose responses differ by an order of magnitude. We now turn to the kind of measurements for which the ONVMS method was developed: those that mix targets of interest and clutter. The next instance of the test-stand experiment includes an aluminum sphere of diameter 10 cm located at $(20\hat{\mathbf{x}}+20\hat{\mathbf{y}})$ cm and on a platform 27.5 cm below the sensor. Anticipating that we will need two sources to describe the large target (a conjecture confirmed by the MSR analysis) we perform a four-source ONVMS inversion. The result obtained after 200 iterations appears on Fig. 4.24(a). The plot looks essentially the same as those of Fig. 4.23, except that it includes the inverted ONVMS profile for the sphere. Again two sources, located this time at $(15\hat{\mathbf{x}}-2\hat{\mathbf{y}}-62\hat{\mathbf{z}})$ cm and $(-11\hat{\mathbf{x}}-\hat{\mathbf{y}}-58\hat{\mathbf{z}})$ cm, line up to yield the response of the 105mm shell, and again the posterior source has an enhanced late-time amplitude. (We have drawn the "partial" sources in a light shade of gray to avoid visual clutter.) The 60mm round is found at $(\hat{\mathbf{x}}-41\hat{\mathbf{y}}-39\hat{\mathbf{z}})$ cm and exhibits the same time-dependent behavior as before. The other target, found by the method at $(20\hat{\mathbf{x}}+22\hat{\mathbf{y}}-27\hat{\mathbf{z}})$ cm, exhibits full spherical symmetry [116, 117]. It also shows a distinct non-ferromagnetic profile whose features are dictated by the high conductivity of the material, with a relatively small initial response and a relatively slow time decay.

Figure 4.24(b) shows the result of adding to the scene a steel prolate spheroid of major and minor axes respectively 20 and 4 cm. The spheroid is parallel to the ordnance and centered at $(-20\hat{\mathbf{x}}-20\hat{\mathbf{y}})$ cm on the same platform as the sphere. Its response is somewhat similar to that of the 60mm round (found by the inversion at $(-40\hat{\mathbf{y}}-38\hat{\mathbf{z}})$ cm), and its azimuthal symmetry is clearly exhibited. To make the figure clearer we have drawn in a light shade of gray the responses of the two ordnance, the larger of which again needs two dipolar sources (located at $(-8\hat{\mathbf{x}}-59\hat{\mathbf{z}})$ cm and $(17\hat{\mathbf{x}}-4\hat{\mathbf{y}}-58\hat{\mathbf{z}})$ cm) for its adequate description. However, the reader should keep in mind that all four objects were illuminated in the measurement and that the response curves coincide quite well with those of the previous figures. The sphere and spheroid locations are estimated to be respectively $(20\hat{\mathbf{x}}+22\hat{\mathbf{y}}-26\hat{\mathbf{z}})$ cm and $(-20\hat{\mathbf{x}}-20\hat{\mathbf{y}}-29\hat{\mathbf{z}})$ cm, in good agreement with the measured values.

As a last example we add two more prolate spheroids to the setup, one made of aluminum with major and minor axes 20 and 4 cm and another made of steel with axes 20 and 5 cm, on the same flat surface as the sphere and spheroid interrogated above and with horizontal locations as shown in Fig. 4.24(d). This method is still capable of analyzing this complex scenario, though its limitations start to become apparent. We used seven sources and ran the code for 600 DE iterations. A source with the 105mm profile is found at $(-3\hat{\mathbf{x}}-59\hat{\mathbf{y}})$ cm and one with a clear set of 60mm decay curves is placed at $(-39\hat{\mathbf{y}}-38\hat{\mathbf{z}})$ cm. The sphere is found at $(-21\hat{\mathbf{x}}-19\hat{\mathbf{y}}-29\hat{\mathbf{z}})$ cm; the spheroids are located by the code at $(-22\hat{\mathbf{x}}+19\hat{\mathbf{y}}-31\hat{\mathbf{z}})$ cm, $(30\hat{\mathbf{x}}-9\hat{\mathbf{y}}-28\hat{\mathbf{z}})$ cm, and $(20\hat{\mathbf{x}}+23\hat{\mathbf{y}}-24\hat{\mathbf{z}})$ cm, again close to the actual measured locations. The appearance of a very weak, apparently unnecessary seventh source at $(7\hat{\mathbf{x}}+11\hat{\mathbf{y}}-2\hat{\mathbf{z}})$ cm (and the fact that it does not appear to contribute to the description of the large ordnance) signals that the method is reaching its limit of accuracy; the symmetry of the sphere is not as evident. On the other hand, the aluminum spheroid, with its longitudinal polarizability smaller than the transverse ones, is well characterized as a nonmagnetic target.

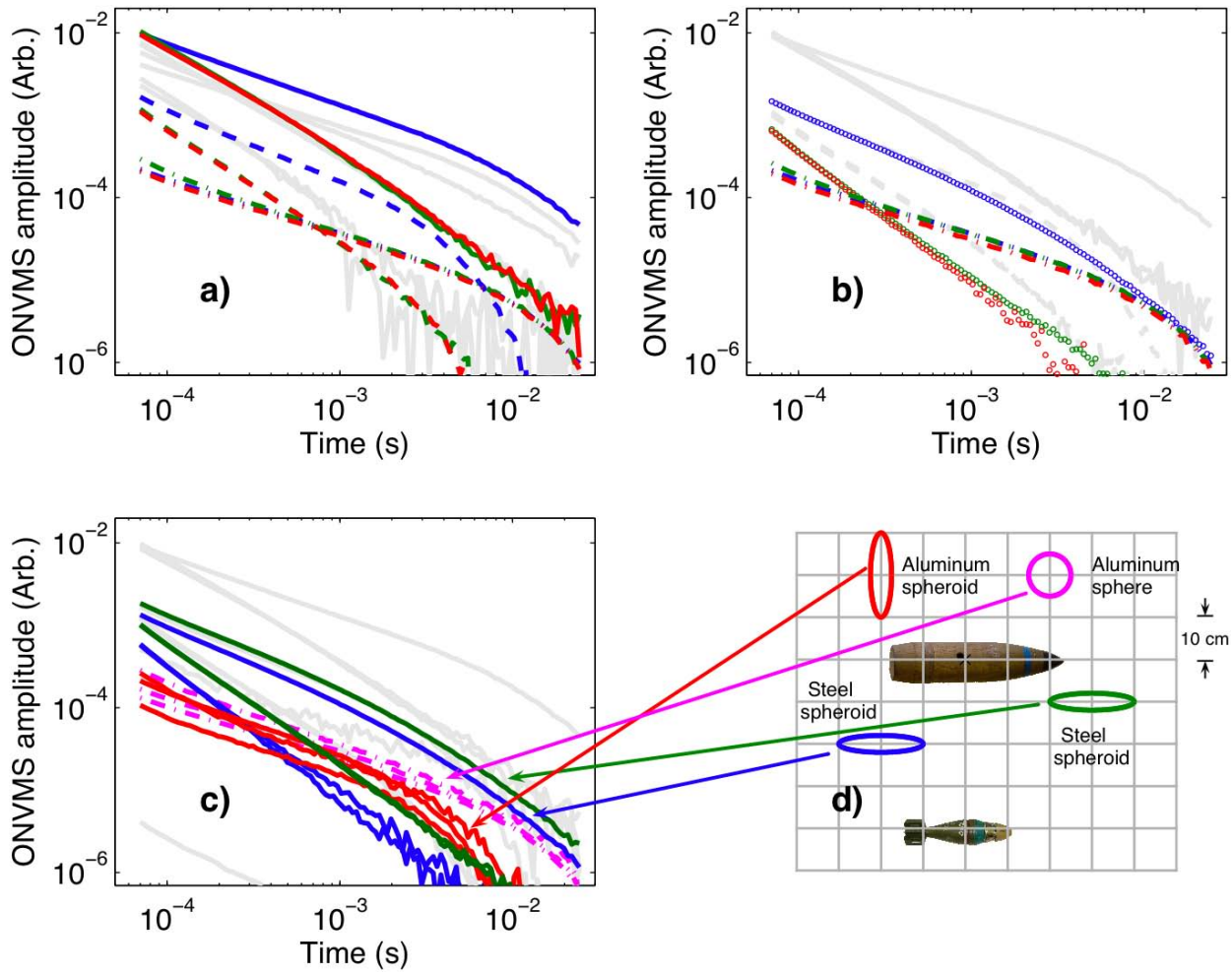

Figure 4.24: The ONVMS method is indifferent to the number of targets under interrogation. (a) A sphere is added to the setup of Figure 4 to produce a three-target scenario that is inverted straightforwardly. The sphere has all three polarizability elements equal. (The sources that compose the 105-mm shell are drawn in light gray to avoid clutter.) (b) Now a steel spheroid (dots) is added to the scene. (Now the two UXO are drawn in light gray to highlight the clutter items.) (c) Two more spheroids are added to form a six-target case with horizontal locations shown in (d). (Again the UXO are drawn in a lighter shade; in panel (c) the ONVMS amplitudes for each target share the same color.) The method yields consistent decay profiles regardless of the number of targets and estimates the locations with reasonable accuracy. The aluminum spheroid is revealed as nonmagnetic.

4.4.c.(2) Camp Butner TEMTADS Data We now look at the results from a demonstration held in 2010 at the former Camp Butner in North Carolina (see Sec. 4.3.c.(2)).

An exploratory cart-based survey with the commercially available Geonics EM61 sensor helped flag the anomalies, which were then subjected to detailed cued examination using TEMTADS (operated by personnel from Nova Research, Inc.) and the MetalMapper (operated by researchers from Geometrics, Inc. and Sky Research). Here we discuss only the data generated by the former and concentrate on its *inversion,* leaving aside the pre-inversion procedure used to estimate the number of targets in each cell and the post-inversion classification protocol; these are presented in detail elsewhere [96, 109].

Figure 4.25 shows the ONVMS profiles extracted for the two kinds of 105mm targets buried at Camp Butner along with photographs of representative samples. The decay curves are quite consistent case-to-case, and the method highlights the qualitative features of the targets transparently even for these noisy measurements. The body-of-revolution symmetry is apparent throughout. It is possible to distinguish between the howitzer shells of Fig. 4.25(a) and the HEAT rounds of Fig. 4.25(b) from the shapes of the curves despite the targets' having the same caliber. Also note the (expected) similarity between the profiles of Fig. 4.25(a) and those extracted for the 105mm shell in the test-stand measurements from the previous section.

Figure 4.26 shows the ONVMS decay curves obtained for the smaller targets of interest in the demonstration. As expected, the objects all have lower overall ONVMS amplitudes than the targets of Fig. 4.25. The fuzes of Fig. 4.26 are in fact larger than the smaller ordnance (they are 7 cm long and 6 cm in diameter), an observation confirmed by their decay profiles. The two types of 37mm projectiles, shown in Fig. 4.26(b) and (c), have curves of similar amplitude that again can be distinguished: the dominant ONVMS elements of the projectiles in Fig. 4.26(c) decay more slowly and show the late-time bulge characteristic of copper driving bands. Again the cylindrical symmetry of the targets is clearly visible. This property becomes of critical importance in discrimination for cases in which the TOI and the clutter are of comparable sizes. We have seen that adding extra sources can show the symmetry of a target more clearly, as though the sources were compensating each other to address the noise in the data; the ease with which the ONVMS procedure can be scaled up to handle multiple sources is one of its salient features.

The accurate and consistent decay profiles found by ONVMS-based inversion result in robust target classification. Fig. 4.27 shows the receiver operating characteristic (ROC) curve obtained by applying the protocol to the cued TEMTADS data. (ROC curves are a useful and increasingly popular method to characterize classifiers; the reference by Fawcett [118] is a good introduction to the topic.) The curve does not start at the origin because the analysts requested the unearthing of 70 anomalies in order to help train the classification algorithms. On the other hand, the curve has an almost 90°elbow, indicating near-perfect discrimination; this is particularly noticeable in the figure inset. In fact, the Institute for Defense Analyses, the entity responsible for scoring the different groups that took the test, declared the ONVMS analyses of MetalMapper and TEMTADS data to be "the two best results seen at the former Camp Butner," noting that the method correctly identified all potentially dangerous targets and reduced the need to dig out false alarms by more than 90% in each case [81]. For the TEMTADS test the figure is actually 95%; in other words, the ONVMS method would have exempted a remediation team from having to carefully dig out 2004 false alarms—a remarkable saving in time and money [78, 119–123].

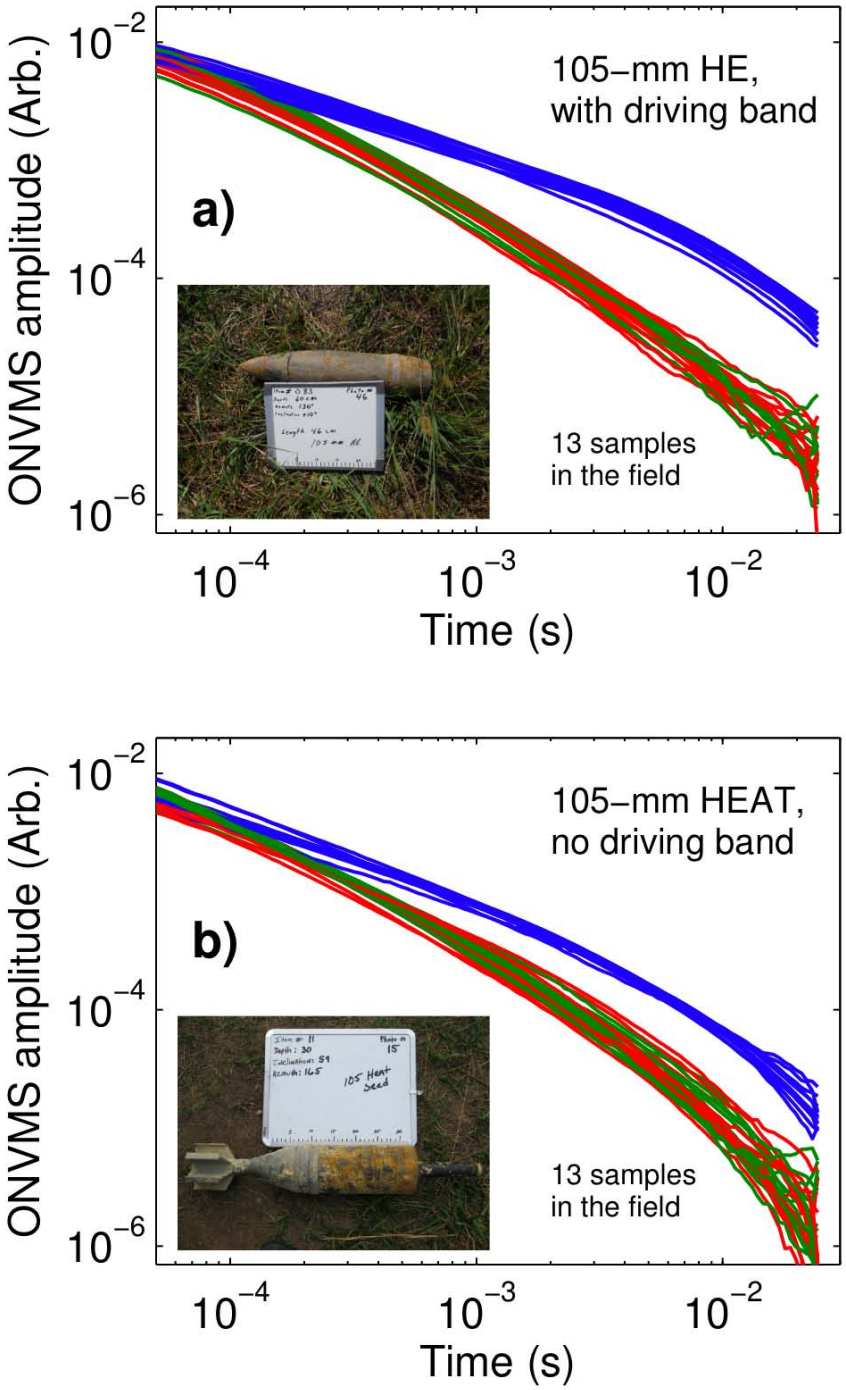

Figure 4.25: Inverted ONVMS amplitudes extracted from the Camp Butner TEMTADS measurements involving large targets of interest: (a) 105mm HE howitzer shells (with copper driving bands) and (b) HEAT rounds of the same caliber. The decay curves reflect the azimuthal symmetry of the targets and are quite consistent sample-to-sample. The insets show photographs of typical scenarios encountered at the test site.

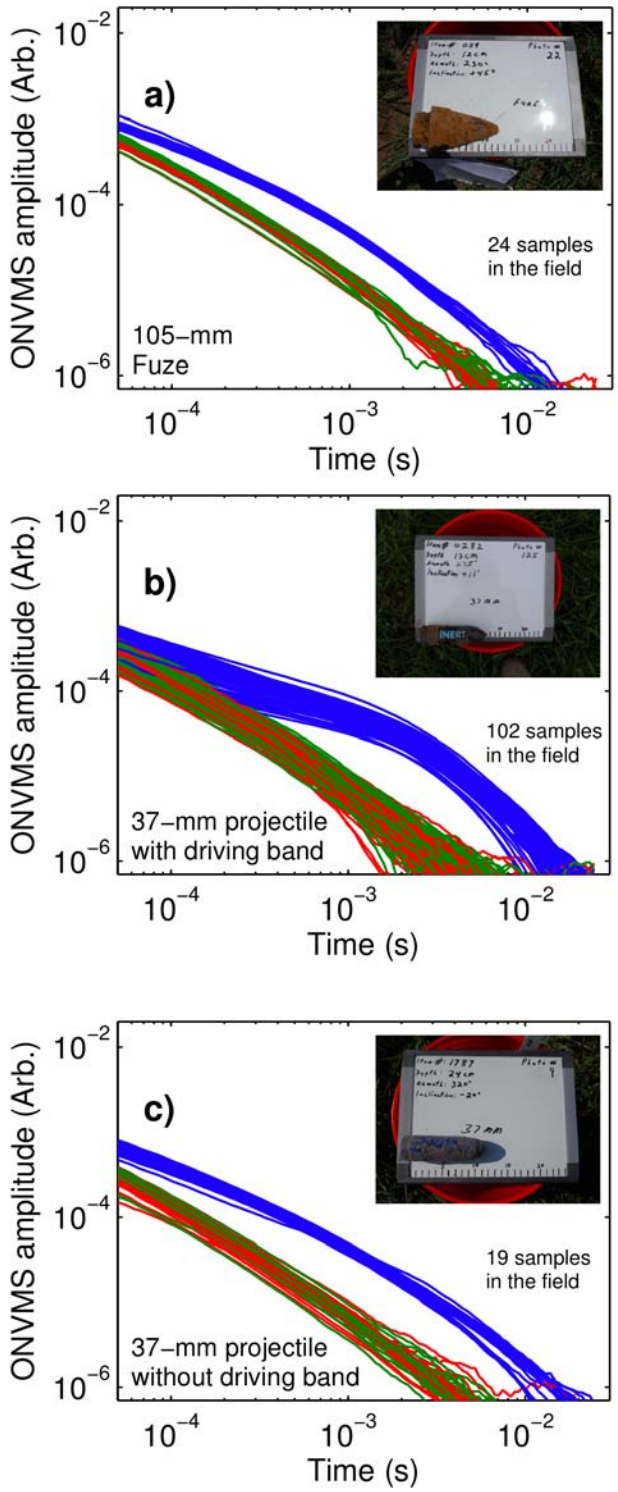

Figure 4.26: ONVMS amplitudes (and representative photographs) of the smaller targets of interest in the Camp Butner test. The fuzes of Fig. 4.26(a) are larger than the other objects. Fig. 4.26(c) shows evidence that the targets have copper driving bands. The cylindrical symmetry of the objects is noticeable throughout.

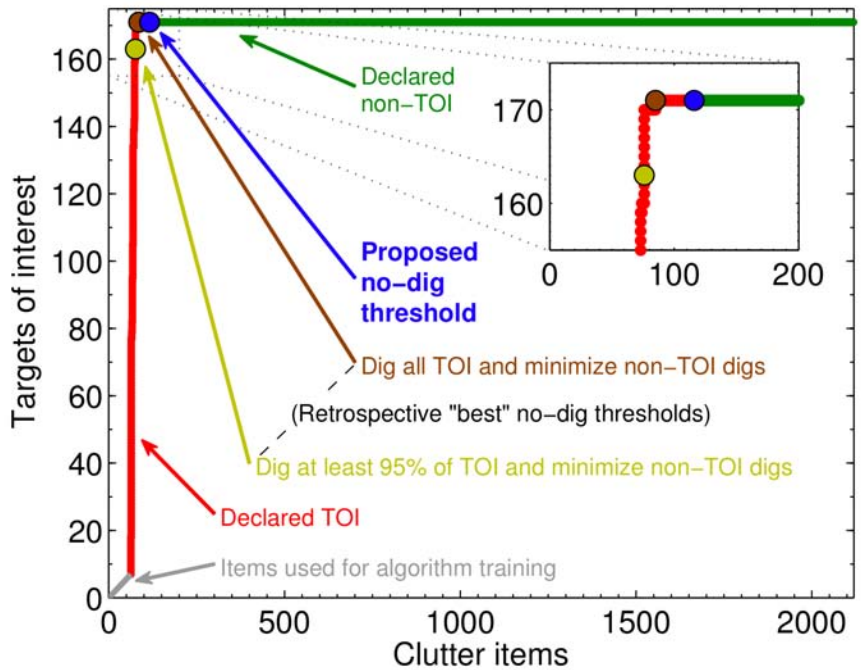

Figure 4.27: Receiver operating characteristic curve for the ONVMS inversion protocol applied to the TEMTADS cued data taken at Camp Butner. The inset zooms in on the area surrounding the "elbow." The rightmost (blue) dot indicates the no-dig threshold proposed by our group. The middle (brown) and leftmost (yellow) dots correspond to two retrospective "optimal" no-dig thresholds determined by the Institute for Defense Analyses. Note the close similarity between our proposed threshold and the "best" ones in view of the large number of targets.

4.4.d Conclusion

In this work we have introduced and presented detailed instructions to implement the orthonormalized volume magnetic source model, a fast, clutter-tolerant, and accurate procedure for inverting electromagnetic induction data to support discrimination of unexploded ordnance. The technique, which works by distributing several dipolar sources over a volume that corresponds to the field of view of the sensor, is indifferent to the number of illuminated targets. Moreover, by allowing for each target to be described by more than one source, the model is capable of characterizing UXO of any size or level of complexity with higher precision and consistency than any other method used in the field, resulting in more robust classification. The method requires the inversion of matrices of very modest size, which enhances its speed and stability, and does not require regularization. To obtain the results we present here we supplemented the ONVMS model with a data-preprocessing algorithm that gives an initial estimate of the number of sources to be used, with differential evolution optimization to determine the locations and orientations of the sources, and with a classification procedure based on hierarchical clustering and Gaussian mixture modeling.

We demonstrated the power and usefulness of the ONVMS model by inverting data collected with the state-of-the-art TEMTADS sensor array, both at a test stand in Maryland and during an actual UXO blind test administered by the Environmental Security Technology Certification Program at the former Camp Butner in North Carolina. In that particular test the technique outperformed

all of its competitors: it provided electromagnetic signatures that led to the correct identification and classification by caliber of all potentially dangerous targets and to a reduction of over 90% in the false-alarm rate. The model has performed equally well in more recent blind tests of greater complexity and has been adapted with success to the other advanced EMI systems expected to be used for UXO remediation in the near future.

5 Results and Discussion

5.1 TEMTADS Data and Results

The spheroids detailed in Sec. 4.1 are now all combined and in the custody of Dan Steinhurst at NOVA Research who maintains and operates the TEMTADS instrument under a contract from NRL. As part of this project, an extensive set of data was acquired over many configurations of multiple targets, including these canonical targets. Table 8 gives a sample of the data collected. For a full list, contact Ben Barrowes.

Data cases 117-126 were given to Dr. Fridon Shubitidze and Dr. Tomasz Grzegorczyk as a blind data set. Figure 4.11 shows a sample picture of the TEMTADS and the targets. Using the JD and ONVMS methods (see Sec. 4.4), Dr. Shubitidze was able to correctly identify all targets in this blind data set (see Fig. 5.1).

Case #	Trg#1	Trg#2	Trg#3	Trg#4	Trg#5	Trg#6
117	60mm (0,-40,-38)	x	x	x	x	x
118	60mm (0,-40,-38)	SS1 (21,22,-26)	x	x	x	x
119	60mm (0,-38,-38)	SS1 (20,20,-26)	SP4S (-20,-20,-28)	x	x	x
120	60mm (0,-37,-40)	SS1 (22,21,-25)	SP4S (-19,-19,-29)	SP4A (-14,28,-30)	x	x
121	60mm (0,-34,-32)	SS1 (18,23,-26)	SP4S (-19,-20,-31)	SP4A (-24,19,-33)	SP4S (30,-8,-28)	
122	60mm (0,-35,-37)	SS1 (23,21,-21)	SP4S (-10,-17,-33)	SP4A (-24,-19,-26)	SP4S (30,-8,-28)	105 mm (0,37, -57)
123	60mm (0,-35,-37)	SS1 (23,24,-21)	SP4S (-12,-10,-33)	SP4A (-28,-30,-24)	x	105 mm (0,41, -57)
124	60mm (0,-37,-38)	SS1 (20,19,-19)	SP4S (-19,-20,-29)	x	x	105 mm (0,36, -57)
125	60mm (0,-38,-39)	SS1 (22,20,-23)		x	x	105 mm (0,38, -58)
126	60mm (0,-38,-39)	x		x	x	105 mm (0,41, -60)

Figure 5.1: Blind inversion results from Dr. Shubitidze using the combined JD and ONVMS methods. All targets correctly identified and positions are within the size of the target.

5.2 MetalMapper Data and Results

To date, there is no good set of data from the MetalMapper over multiple targets. As a substitute, we constructed a set of multitarget data from single target data via superposition. This data comes from test data that Dave George took while calibrating the MetalMapper. For this test, one of three targets:

1. 10cm diam sphere
2. 13cm piece of rebar

Date	Prefix	Depth to Base (cm)	Targets Present	Orientation
1/15/2010	20100115_			
1/15/2010	20100115_	27.5(clutter)	SS1, Al	
1/15/2010	20100115_	27.5(clutter)	SS1, Al; SP4, steel	SP4S flat, along x
1/15/2010	20100115_	27.5(clutter)	SS1, Al; SP4, steel; SP4 Al	SP4S flat, along x, SP4A flat, along y
1/15/2010	20100115_	27.5(clutter)	SS1, Al; SP4, steel; SP4 Al; SP3 steel	SP4S flat, along x, SP4A flat, along y; SP3S flat, along x
1/15/2010	20100115_	27.5(clutter);63(105mm)	105mm; SS1, Al; SP4, steel; SP4 Al; SP3 steel	105mm flat, nose toward +x,SP4S flat, along x, SP4A flat, along y; SP3S flat, along x
1/15/2010	20100115_	27.5(clutter);63(105mm)	105mm; SS1, Al; SP4, steel; SP4 Al	105mm flat, nose toward +x,SP4S flat, along x, SP4A flat, along y
1/15/2010	20100115_	27.5(clutter);63(105mm)	105mm; SS1, Al; SP4, steel	105mm flat, nose toward +x,SP4S flat, along x
1/15/2010	20100115_	27.5(clutter);63(105mm)	105mm; SS1, Al	105mm flat, nose toward +x
1/15/2010	20100115_	63(105mm)	105mm	105mm flat, nose toward +x
1/15/2010	20100115_			
1/15/2010	20100115_	38(60mm)	60mm	60mm flat, nose toward +x
1/15/2010	20100115_	27.5(clutter);38(60mm)	60mm; SS1, Al	60mm flat, nose toward +x
1/15/2010	20100115_	27.5(clutter);38(60mm)	60mm; SS1, Al; SP4, steel	60mm flat, nose toward +x,SP4S flat, along x
1/15/2010	20100115_	27.5(clutter);38(60mm)	60mm; SS1, Al; SP4, steel; SP4, Al	60mm flat, nose toward +x,SP4S flat, along x, SP4A flat, along y
1/15/2010	20100115_	27.5(clutter);38(60mm)	60mm; SS1, Al; SP4, steel; SP4 Al; SP3 steel	60mm flat, nose toward +x,SP4S flat, along x, SP4A flat, along y; SP3S flat, along x
1/15/2010	20100115_	27.5(clutter);38(60mm); 63(105mm)	60mm; 105mm; SS1, Al; SP4, steel; SP4 Al; SP3 steel	60mm/105mm flat, nose toward +x,SP4S flat, along x, SP4A flat, along y; SP3S flat, along x
1/15/2010	20100115_	27.5(clutter);38(60mm); 63(105mm)	60mm; 105mm; SS1, Al; SP4, steel; SP4 Al	60mm/105mm flat, nose toward +x,SP4S flat, along x, SP4A flat, along y
1/15/2010	20100115_	27.5(clutter);38(60mm); 63(105mm)	60mm; 105mm; SS1, Al; SP4, steel	60mm/105mm flat, nose toward +x,SP4S flat, along x
1/15/2010	20100115_	27.5(clutter);38(60mm); 63(105mm)	60mm; 105mm; SS1, Al	60mm/105mm flat, nose toward +x
1/15/2010	20100115_	38(60mm); 63(105mm)	60mm; 105mm	60mm/105mm flat, nose toward +x

Table 8: Sample data cases from TEMTADS multiobject data set, January, 2010.

3. 21cm diameter copper ring

were placed in one of five positions under the MetalMapper (see Fig. 5.2).

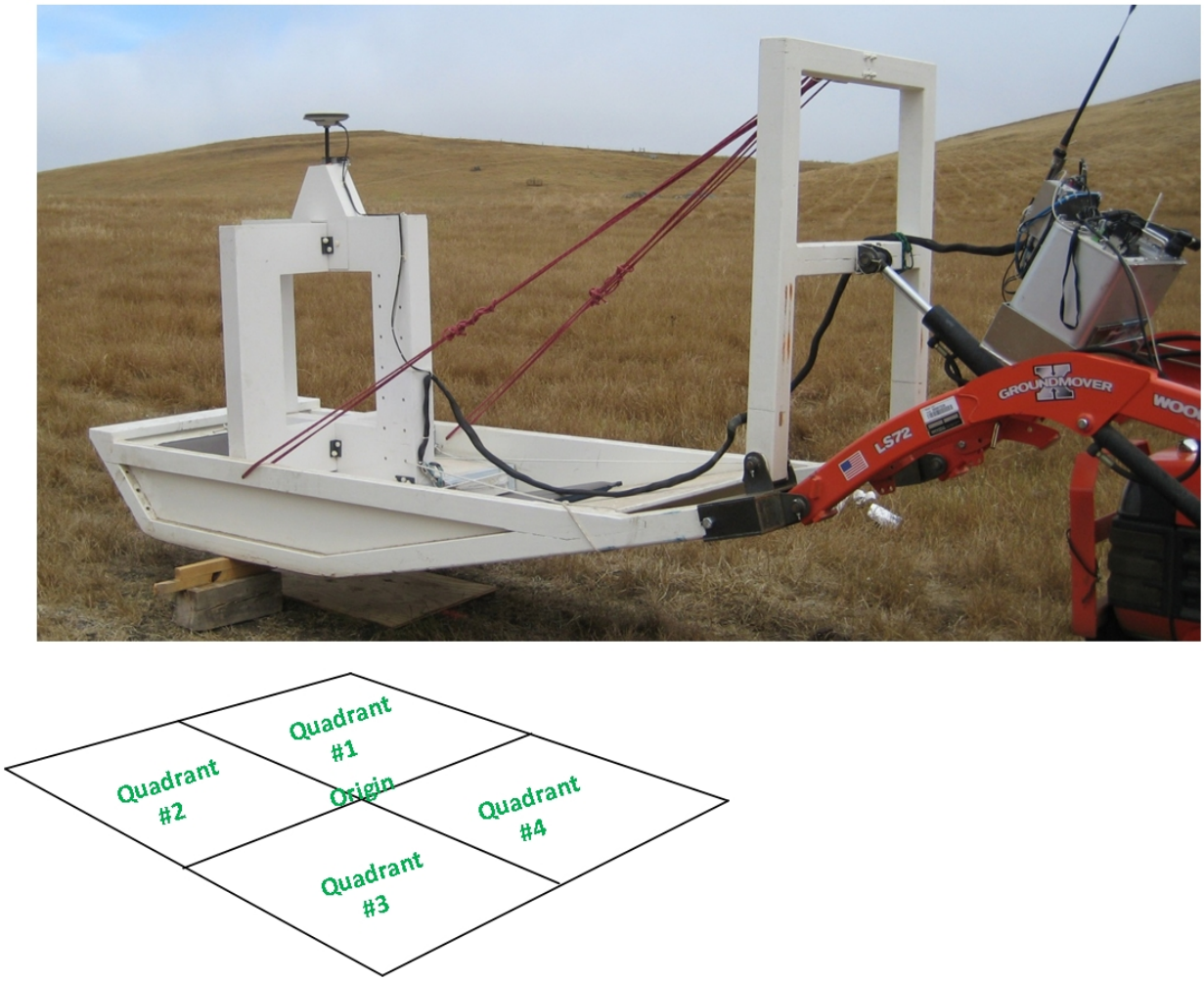

Figure 5.2: MetalMapper test setup with one of three targets in one of five positions. Blind multi-target test data synthesized by superposing different data cases.

In the magnetoquasistatic (MQS) regime, the data can be superposed without difficulty. Therefore, multitarget test data was synthesized by adding up the data from different cases of targets in different quadrants. Table 9 shows the original data from which these blind tests were synthesized. These original data were superposed (added) in the following combinations (see Table 10) before being given to Dr. Fridon Shubitidze and Dr. Tomasz Grzegorczyk as a blind data set.

Using the multiple dipole Jacobian based gradient search method (see Sec. 4.2), Dr. Grzegorczyk was able to correctly identify all the targets in the semiblind data sets (see Figs. 5.3 and 5.4). The results for each case are computed in under one minute if the number of targets, N, is known. Finding N for this method, however, still requires an expert's interpretation of the polarizabilities assuming different N.

File #	target	depth to bottom of target	orientation	quadrant
2	sphere	35cm	N/A	1
3	ring	35cm	horizontal(H)	1
4	ring	35cm	vertical(V)- 0deg	1
5	rebar	35cm	horizontal - 0deg	1
6	sphere	35cm	N/A	2
7	ring	35cm	H	2
8	ring	35cm	V - 0deg	2
9	rebar	35cm	H - 0deg	2
10	sphere	35cm	N/A	3
11	ring	35cm	V - 0deg	3
12	ring	35cm	H - 0deg	3
13	rebar	35cm	H - 0deg	3
14	sphere	35cm	N/A	4
15	ring	35cm	H - 0deg	4
16	ring	35cm	V - 0deg	4
17	rebar	35cm	H - 0deg	4
18	sphere	35cm	N/A	0
19	ring	35cm	H - 0deg	0
20	ring	35cm	V - 0deg	0
21	rebar	35cm	H - 0deg	0

Table 9: Original MetalMapper calibration data.

Using the combined JD and ONVMS methods, each of the 1-5 targets was also correctly identified for this blind set of MetalMapper data (see Fig. 5.5). These results take longer (10's of minutes for each case) to compute, but are aided by an estimate for N provided by the JD method.

5.3 MPV2 Data

MPV2 data was collected recently at CRREL in Hanover, NH in support of several SERDP project and with many goals in mind:

- Collect data over small targets at several depths including greater than 11 times the diameter (in support of MR-2106)
- Collect data over 2 and 3 target scenarios both small and larger targets in several combinations (in support of MR-2106 and MR-1664)
- Collect data over deep, larger targets
- Collect data of small and large targets with a clutter layer between the targets and the MPV2 (in support of MR-2106 and MR-1664 and MR-1005)
- To carefully characterize the beacon positioning system accuracy in terms of both position and orientation

blind test #	original file #'s
1	[18,2]
2	[13,2,7]
3	[4,7,13,14]
4	[9,21]
5	[16,3]
6	[19,10,6,5]
7	[8,21,17]
8	[15,11,9]
9	[5,8,10,15,20]

Table 10: MetalMapper blind test data configurations synthesized by superposing data cases from Table 9.

Case nb	Nb of targets	Targets id				
1	2	2	18	-	-	-
2	3	2	7	13	-	-
3	3	4	7	13	14	-
4	2	21	9	-	-	-
5	2	3	16	-	-	-
6	4	5	6	10	19	-
7	3	8	21	17	-	-
8	3	11	9	15	-	-
9	5	5	8	10	15	20

Figure 5.3: Results from using the multiple dipole Jacobian based gradient search method. Refer to Tables 9 and 10.

- To investigate the integration time of the DAQ window of the MPV2 in order to optimize the data acquisition protocol (in support of MR-1005 and future MPV2 projects)
- To collect some data used for blind tests for our recent algorithms as applied to handheld sensors

We collected this data in February 2011, and we believe our data set will fulfill all these stated goals above, but we have not had time to produce any results from this data set.

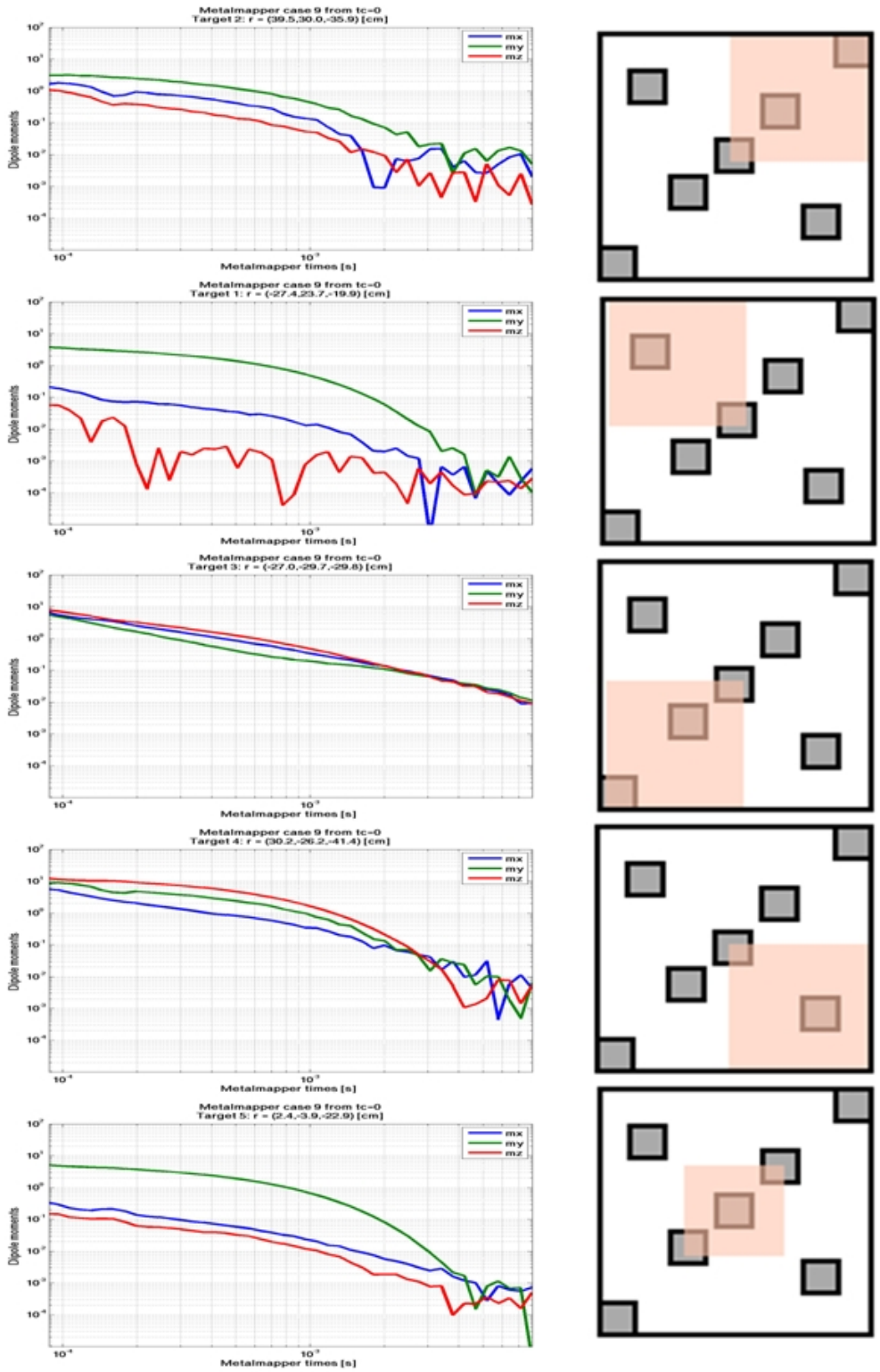

Figure 5.4: Polarizabilities extracted for blind case 9 using the Jacobian multiple dipole search method. Refer to Tables 9 and 10.

Case #	Object 1/ Location (cm)	Object 2/ Location (cm)	Object 3/ Location (cm)	Object 4/ Location (cm)	Object 5/ Location (cm)
1	Sphere / (26, 28, -37)	Sphere / (0,0, -35)	N/A	N/A	N/A
2	Sphere / (26, 28, -37)	Ring / (-26, 21, -28)	Rebar/ (-27, -28, -38)	N/A	N/A
3	Ring / (31, 28, -29)	Ring/ (-26, 21, -42)	Rebar / (-27, -28,-38)	Sphere/ (29, -26,-35)	N/A
4	Rebar/ (-28, 24, -38)	Rebar/ (0,0,-36)	N/A	N/A	N/A
5	Ring/ (26, 28, -41.5)	Ring/ (29,-27,-29)	N/A	N/A	N/A
6	Rebar/ (28,23,-38)	Sphere/ (-28, 24,-35)	Sphere/ (-26, -30, -35)	Ring/ (0,0,-40)	N/A
7	Ring/ (-30,23,-28)	Rebar/ (25,-32,37)	Rebar/ (0,0,-36)	N/A	N/A
8	Rebar/ (-28,24,-38)	Ring/ (-25,-30,-28.5)	Ring/ (29,-27,-43)	N/A	N/A
9	Rebar/ (28, 23, -38)	Ring/ (-30,23, -28)	Sphere/ (-26,-30, -30)	Ring/ (29,-27,-29)	Ring (0,0,-27)

Figure 5.5: Inversion results from using the combined JD and ONVMS methods. Refer to Tables 9 and 10.

5.4 Camp Butner Live-Site UXO Classification using Hierarchical Clustering and Gaussian Mixture Modeling

We demonstrate in detail a semi-supervised scheme to classify unexploded ordnance (UXO) using as example the data collected with the Time-domain Electromagnetic Towed Array Detection System during a live-site blind test conducted at the former Camp Butner in North Carolina. The model we use to characterize targets and generate discrimination features relies on a rigorous solution of the inverse UXO problem using the Orthonormalized Volume Magnetic Source model. Unlike other classification techniques, which often rely on library matching or expert knowledge, our combined clustering/Gaussian-mixture-model approach first uses the inherent properties of the data in feature space to build a custom training list which is then used to score all unknown targets by assigning them a likelihood of being UXO. The ground truth for the most likely candidates is then requested and used to correct the model parameters and reassign the scores. The process is repeated several times until the desired statistical margin is reached, at which point a final dig list is produced. Our method could decrease intervention by human experts and (as the results of the blind test show) identify all targets of interest correctly while minimizing the false-alarm count.

5.4.a Introduction

In this section we concentrate on the third ESTCP discrimination test, which took place at the former Camp Butner, located approximately 15 miles north of the city of Durham and straddling Durham, Granville, and Person Counties, all in North Carolina [1, 124, 125] (also see Sec. 4.3.c.(2)). Though we briefly discuss the processes of data acquisition and inversion, our main objective here is to report on the performance of an automated classification approach that reduces human involvement (and human error) and attempts to process data with high sensitivity (i.e., detecting all potentially dangerous targets) and specificity (i.e., leaving buried as many innocuous targets as possible). Several clustering and statistical signal processing techniques have been used previously to identify UXO starting from magnetometer and EMI data [8, 24, 63, 126]. In at least one case the classification is based on "shape and size information" extracted from direct magnetic field observations "examined visually" and "viewed as [...] image[s]," with no underlying physical model [127]. (The method presented in that reference is found to outperform a physics-based model, though that may be because the physics in the model is not quite correct.) Library matching and SVM or neural-net-based decision-making [93, 95, 99, 128–130] have been studied and applied to UXO classification based on different features, such as size or temporal decay [125]. Instances of successful application of Bayesian data fusion, multivariate Gaussian representation of EMI signals, and semi-supervised learning techniques have also been reported [94, 131, 132]. Most of these techniques require human knowledge and intervention and need a sample of training data, which in some cases may not be representative, or even available.

The goal of our automated classification process is to reduce the workload of human experts by having them perform the crucial tasks of decision-making and quality control while delegating to the software routine tasks such as feature extraction, clustering, and labeling. Another feature of our method is that it does not require any pre-collected training data. Instead, the algorithm "trains itself" by asking for a set of anomalies to be unearthed—either because their features are particularly representative of an already identified category of targets or because they belong to a yet-unexplored region of the feature space—and then taking in the new knowledge. At the first

stage of the process, the method examines the data and uses only unsupervised learning techniques to build and request a custom training set required to identify the "suspicious" regions characterizing all the types of UXO expected at the site. Once the truth is known, the model incorporates it and starts an iterative process, internally updating its settings to accommodate newly available information and then either requesting more ground truth to further fine-tune the classification or, at the end, provide a final priority-weighted dig list.

The third and most important feature of the method is its performance. On the Camp Butner test our procedure yielded 100% accuracy in TOI detection and by-caliber classification; it required 295 false alarms to be dug out, thus leaving in the ground more than 85% of the clutter.

5.4.b Methods

The data presented here were acquired at Camp Butner using the TEMTADS instrument (see Sec. 4.3.b.(1)).

5.4.b.(1) Data inversion UXO discrimination demands a fast and accurate representation of a target's EMI response. The model used most frequently for this purpose approximates the whole object with a set of orthogonal co-located point dipoles whose induced effective moment is related to the primary field through a symmetric polarizability tensor [97]. The model is fast and easy to implement and interpret, but it rests on assumptions that often limit its usefulness [78]. Large and complex targets (for example, those containing sections with different materials, fins, rings, etc.) require more advanced methods like the Normalized Surface Magnetic Source (NSMS) model [14, 18, 28, 100, 133, 133–135] that we used at Camp Sibert and SLO [130]. The NSMS method spreads a non-uniform distribution of normally oriented dipole moment (scaled by the primary field) over a virtual prolate spheroidal surface that encloses the target. This distribution can be determined directly by minimizing the difference between measured and modeled data for a known combination of object and sensor at a given relative location and orientation. The integral of the distribution over the spheroidal surface is a global effective magnetic polarizability (referred to as "total NSMS") that generalizes the polarizability tensor of the dipole model and provides a more rigorous description of a single object.

In real-world situations, however, TOI tend to be surrounded by metallic debris and often cluster together. As a consequence, it is frequently not clear how many objects are producing a given detected signal. This uncertainty hindered the performance of our classification scheme in the SLO test [130] and prompted us to look for a characterization model that would properly decouple overlapping signals. The result was the Orthonormalized Volume Magnetic Source (ONVMS) model [82] (see Sec. 4.4), which represents subsurface scatterers using a volumetric distribution of magnetic field sources and searches for the optimal configuration of source locations and strengths producing a given measured response.

The advantage of the ONVMS technique is that, by constructing the orthonormalized sets of Green functions, it takes into account mutual couplings between different sections of the different targets and, at the same time, avoids the appearance of singular matrices in multi-target situations. It is indifferent to the number of targets: once the amplitudes and the locations of the source dipoles are determined, one need only look at their spatial patterns and compute and diagonalize the time-dependent total polarizability tensor for each spatial group. The resulting time-dependent diagonal elements have a phenomenology similar to those of dipole polarizabilities [64] or total NSMS

amplitudes [100], providing insight into intrinsic target properties such as cylindrical symmetry, surface area, metal content, and ferromagnetic behavior.

The ONVMS method takes as input the number M of radiating sources, which is, in principle, unknown. For the MetalMapper and the 2×2 and 5×5 TEMTADS arrays [4, 5, 136] we have developed a procedure based on joint diagonalization that estimates M with no need to invert any data [109]. For other sensors one may proceed by letting M vary as part of an optimization routine.

In this study we used 1-target, 2-target, and 3-target inversions in sequence to gradually improve the accuracy of classification. One-target inversion is equivalent to the simple dipole model and can be used to perform an initial quick screening of the site and identify easy targets. Its performance degrades significantly, however, in situations where multiple physical objects fall in the field of view of the sensor. While inversions assuming more than one source can effectively decouple the signals from these complicated scenarios, additional processing is required when the actual number of buried objects is *less* than their assumed number M: in those cases, two or more triplets $Q_{\{x,y,z\}}$ of effective polarizability decay curves could correspond to different parts of a single physical object. In order to achieve consistency in object characterization, and to guarantee that all dangerous targets are identified, it is important to try out all possible combinations of these curves. For M-target inversion it is necessary to consider a total of $\Sigma_{k=1}^{M} \begin{pmatrix} M \\ k \end{pmatrix} = 2^M - 1$ combinations of effective polarizability decay curves: those of individual targets $Q_{\{x,y,z\}}(t) = JD\left(\bar{\bar{\mathbf{M}}}_i(t)\right)$, their duplets $Q_{\{x,y,z\}}(t) = JD\left(\bar{\bar{\mathbf{M}}}_i(t) + \bar{\bar{\mathbf{M}}}_j(t)\right)$, triplets $Q_{\{x,y,z\}}(t) = JD\left(\bar{\bar{\mathbf{M}}}_i(t) + \bar{\bar{\mathbf{M}}}_j(t) + \bar{\bar{\mathbf{M}}}_k(t)\right)$, and so on, where $i \neq j \neq k \in \{1, \ldots, M\}$ and JD stands for joint diagonalization.

We observe that multi-target inversions provide target signatures that are more consistent case-to-case than those resulting from single-target inversions. For example, Fig. 5.6 shows the Q_z EMI decay curves obtained for two of the Camp Butner anomalies, #30 at left and #3 at right, both of which contain 105-mm HEAT rounds. In each case, the black crosses denote the effective longitudinal polarizabilities obtained from 1-target inversion, whereas the red dots (seven curves per plot) show the possible combinations that result from 3-source inversion. For discussion purposes let us label those sources A, B and C. The UXO at left was almost vertical—the ground truth, seen in the photograph, reveals that its inclination was 81°—and the 1-target inversion captures only its top region, which is much closer to the sensor than the rest. On the other hand, if we allow two or more dipoles to describe the target, we see a decay curve that agrees better with the case at right and with HEAT-round decay profiles known from previous experiments. Though all three dipolar sources contribute to the signal, one of them (C, say) is clearly dominant; the bottom curves thus correspond to the possibilities A, B, and A+B while the top curves represent C, A+C, B+C, and A+B+C. In the case at right, the target—whose inclination is now $-10°$—is in full view of TEMTADS and can be described well using a single source. The 3-source inversion favors a two-dipole description of the TOI in this instance: if A and B are the relevant sources, then the curves at bottom correspond to A, B, C, A+C, and B+C and those on top represent A+B and A+B+C. Only by considering combinations of sources can we expect to characterize targets of interest unambiguously enough to identify and classify them.

In this study we have concentrated on Q_z the largest effective polarizability, to perform classification; we have noticed that the other amplitudes are often compromised due to low signal to noise ratio (SNR), especially for small or deep targets [130]. (Henceforth we suppress the subscript z.)

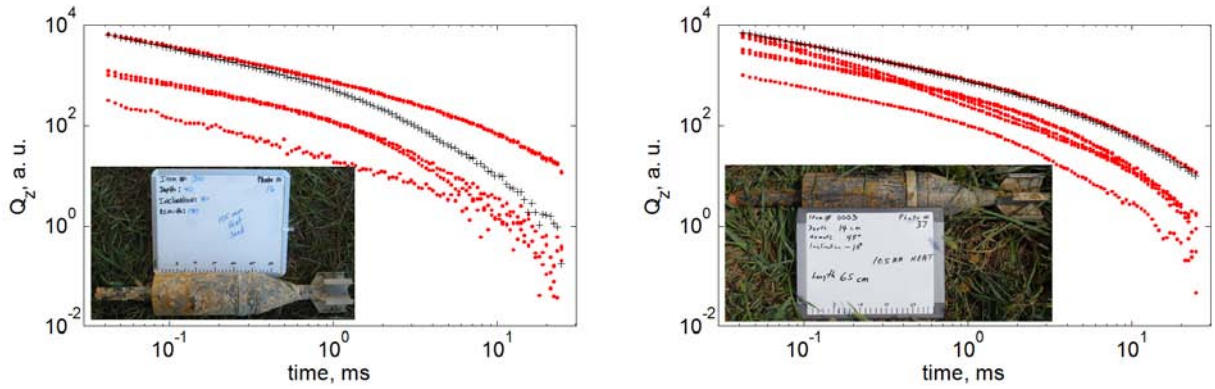

Figure 5.6: Results of 1-target and 3-target inversions of two Camp Butner anomalies containing 105-mm HEAT rounds. The differing noise environments and relative target/sensor locations cause the 1-target inversions (black crosses) to provide quite different EMI decay curves for two instances of the same object. On the other hand, the 3-target inversions (red dots, seven curves per plot) properly capture the responses from the different sections of the targets and synthesize them into consistent decay curves that come closer to representing the projectiles' true electromagnetic signatures.

We decrease the dimensionality of the feature space by fitting the decay curves to an empirical law popularized by Pasion and Oldenburg [99],

$$Q(t) = kt^{-b}e^{-gt}. \tag{5.4.1}$$

To decrease the effects of noise we first linearize (5.4.1) by taking its logarithm. We then extract the Pasion-Oldenburg parameters log k, b, and$g$ using nonlinear least squares, imposing the constraints $b > 0$ and $g > 0$ to preserve the physical essence of the data. The fits are always performed for times $t > 0.1$ ms to avoid perturbations due to the primary field, whose shutoff is not instantaneous. In order to disregard the "leveling-off" of the decay curves in log space when they reach the noise threshold we also assign an upper bound to the time channels used for the fit. This bound depends on the particular anomaly, and within each anomaly differs for the x-, y- and z- decay curves. To find it we estimate the inherent noise level of the decay curve $Q(t)$ as its mean value over the last N time channels (with $N = 10$ chosen by hand) and set the threshold value $t_{\max}$ to the time in which the curve falls below this average: $Q(t_{\max}) \leq mean(Q_{123-N}, \ldots, Q_{123})$. Due to the presence of several highly noisy anomalies we impose a lower bound on $t_{\max}$ to ensure that there is sufficient information for the fits; we chose $t_{\max} > 0.3$ ms. These considerations result in dramatically improved fits, as can be seen in Fig. 5.7 [130].

5.4.b.(2) Classification In this section we combine agglomerative hierarchical clustering [137] and probabilistic classification to perform semi-unsupervised learning for UXO discrimination; the classification features we use are the Pasion-Oldenburg parameters extracted from ONVMS decay curves. We first used clustering in feature space to split the entire data set into a finite number of clusters. The number of clusters is an external parameter and was set to be between 1% and 5% of the number of items in the data set. There are several options for clustering based on different

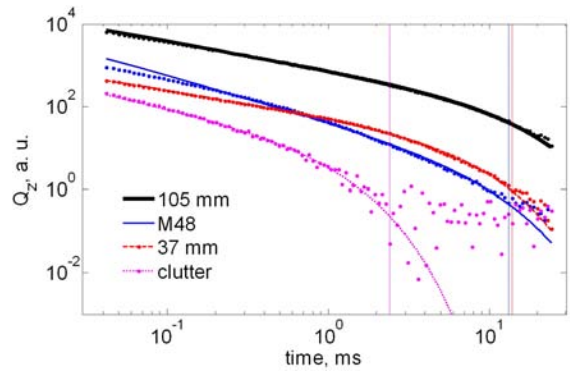

Figure 5.7: Actual Q_z EMI decay curves (dots) and constrained Pasion-Oldenburg fits (solid lines) for some of the targets of interest at Camp Butner. The vertical lines mark $t_{\max}$, the upper threshold of the fitting domain.

criteria and distance metrics; we found the following two combinations particularly useful for initial screening of the feature space [130]:

1. Ward linkage with Euclidean distances [138–140]. The Ward technique encourages the formation of homogeneous clusters by controlling the sum over all clusters of the sum of squared Euclidean distances between the members of a cluster and its centroid,

$$E = \sum_{k=1}^{K} \sum_{x_j \in C_k} \left\| \mathbf{x}_j - \mathbf{m}_k \right\|^2, \tag{5.4.2}$$

where K is the total number of clusters and $\mathbf{m}_k$ is the centroid of cluster C_k [139]. At each step of the process the two clusters whose merger increases E by the least amount are merged, decreasing the number of clusters by one unit. The process starts with the individual data points as clusters and stops when the desired number of clusters (set a priori to about 5% of the total number of anomalies) is reached.

1. Weighted Pair Group Method Average (WPGMA) linkage with Mahalanobis distances. Like Ward's, the method starts with the individual data points and merges them into clusters, decreasing the number of entities one by one until a preset value is reached. The clusters joined at each step are those found to be separated by the shortest WPGMA metric, which is defined recursively [139, 141] by the rule $d(R, P+Q) = (d(R,P) + d(R,Q))/2$ expressing the separation between a cluster R and another resulting from the merger of P and Q [142]. (To compute the separation between data points at the last level of recursion we use the Mahalanobis distance [143, 144], which takes into the account the natural variation and spread of physically different feature values in their own dimension and is thus potentially useful for clustering.)

Upon finding the clusters we requested the ground truth for the anomalies that lay closest to the geometric center of each. The clusters that happened to be centered around TOI were further labeled as potential UXO clusters and used as a basis to construct a Gaussian mixture model

(GMM) in which each suspicious cluster was fit with a multivariate normal distribution. Every anomaly was assigned a score—a measure of its probability of being a particular type of UXO—based on its position relative to the UXO clusters; those scores, in turn, were used to sort the anomalies and generate a prioritized dig list.

As we mentioned previously, multi-target inversion often provides better target localization and more precise and consistent—and thus more reliable—classification features. In a 2-target inversion case, however, this means having three times as many data points in feature space because each physical anomaly is represented by a triplet of points. If any of these three points is suspected to be a UXO, the whole anomaly (i.e., all objects buried at that specific location at the UXO site) will be treated as UXO.

While it is still possible to perform the data clustering in multi-target-inversion feature space, there is no straightforward way to identify which group of points to request as training data and how to interpret the results. Suppose a training data point is requested from a certain cluster that contains only clutter (perhaps even having outlier values as features). Whereas the data point corresponding to this object indeed has features peculiar to clutter, it can happen that this point belongs to a triplet containing a UXO, which will be revealed after the ground truth for the particular anomaly is studied. Since it is impossible to determine without prior library knowledge which of the points in the 2-target-inversion triplet (target 1, target 2, or their superposition) actually represents the signal from the UXO, one would have to flag all three locations in feature space as potential UXO and contend with an intolerably large false-alarm rate.

To get around this issue we employ a two-step approach. In the first step, the features extracted only from single-target inversions are clustered and the corresponding ground truth is requested. The central elements belonging to each of the clusters are then probed, and those identified as UXO are marked. In the second step, M-target-inversion features are clustered with the same algorithm, with the number of clusters being $2^M - 1$ times greater than in the first step. After that, the confirmed UXO feature coordinates from single-target inversion can be imported into the multi-target feature space, and the clusters closest to these points marked as potential UXO. Such an approach combines the ease of training data interpretation of the single-target-inversion case with the rigor and accuracy of multi-target inversion. The multivariate GMM can then be constructed around the identified UXO clusters, and the rest of the anomalies are assigned a score that quantifies their likelihood of being UXO.

The combined clustering/GMM approach therefore provides a natural way to find intrinsic patterns in noisy feature data and yields a convenient probabilistic measure of class membership for unknown items. It also reduces the amount of required training data and improves both classification sensitivity and specificity.

5.4.c Results

In this section we apply the classification technique described above to the Camp Butner blind-test data. The classification process consisted of the following steps:

1. No initial training data were requested. (We knew, however, that three types of UXO targets were expected: 37-mm and 105-mm projectiles, as well as M48 fuzes.)

2. The features log k, b, and g were extracted from the data for all anomalies starting from 1-target, 2-target, and 3-target inversions.

3. An initial Ward clustering (with Euclidean distances) was performed, and, in order to probe the feature space, the ground truth was requested for the 69 targets whose features were located closest to the cluster centroids.

4. Clusters containing at least one UXO were identified, and a smaller domain was selected within the feature space for further interrogation. (One projectile of each kind was identified, but no fuzes.)

5. A second clustering (WPGMA, with Mahalanobis distances) was performed within the selected domain, primarily to seek for M48 fuzes. The targets with features closest to the corresponding cluster centroids (26 at this step) were singled out and their ground truth requested. The clusters with at least one identified UXO were marked as *suspicious*.

6. All targets whose features (based on 2-object inversion) fell inside any of the *suspicious* clusters were used to train a 3-component GMM classifier and score all of the unknown targets.

7. All targets with a score greater than a specifically selected threshold were assumed to be UXO, and the ground truth was requested for them. (Selecting this threshold is one of the few parts of the process that involves human decision-making.) This set consisted of 131 targets, three of which had already been requested previously; of these, 118 were confirmed to be UXO.

8. A new 3-component GMM classifier was trained using features from the 3-object EMI inversions. All the items were re-scored to correct for changes and incorporate new information. Another 20 targets with scores decreasing from a certain expert-defined low value were selected for additional verification. At this point, if the verification had yielded that all the chosen targets were clutter, the algorithm would stop and the scored values would be used to produce a final dig list.

9. Four out of the 20 items requested happened to be UXO, and the classification continued. (The ground truth for three of these 20 items had already been requested in the previous steps, and one had been confirmed as UXO.)

10. All confirmed UXO were separated into three groups (105-mm, M48, and 37-mm); no further within-group discrimination was performed. Each of the three groups was used to train a separate 1-component GMM classifier that scored all the targets with respect to target type (based on the features obtained from precise 3-object EMI inversions). The ground truth was then selected individually for each object type, based on a certain threshold score. This step helped describe the individual clusters in more detail.

11. A total of 36 items were requested from a 105-mm scored data set, with 18 being already known; 174 items were requested from a 37-mm scored data set, with 118 being already known; and 53 items were requested from a M48 scored data set, with 27 of them being already known. At this stage a total of 322 items were requested, of which 162 were UXO.

12. Finally, a 3-component GMM classifier was trained on the confirmed UXO and further used to score all of the unknown targets. A specific threshold was then selected and the final dig list produced.

Fig. 5.8 shows the results of the first two clustering processes, corresponding to Steps 2 through 5 above. Only four UXO targets were identified at this stage: two 37-mm munitions (with features very close to each other in Fig. 5.8), one M48 fuze, and one 105-mm projectile. Fig. 5.9 illustrates the training data used to create a three-component GMM classifier in Step 6 and the resulting score distribution histogram. The external interaction from the expert in this case consisted in selecting an anomaly-scoring threshold beyond which the ground truth would be requested. We picked a value of log (score) ˜ 0.5, which resulted in the right peak of the histogram being probed and yielded a high number of 118 confirmed UXO out of 131 probed items.

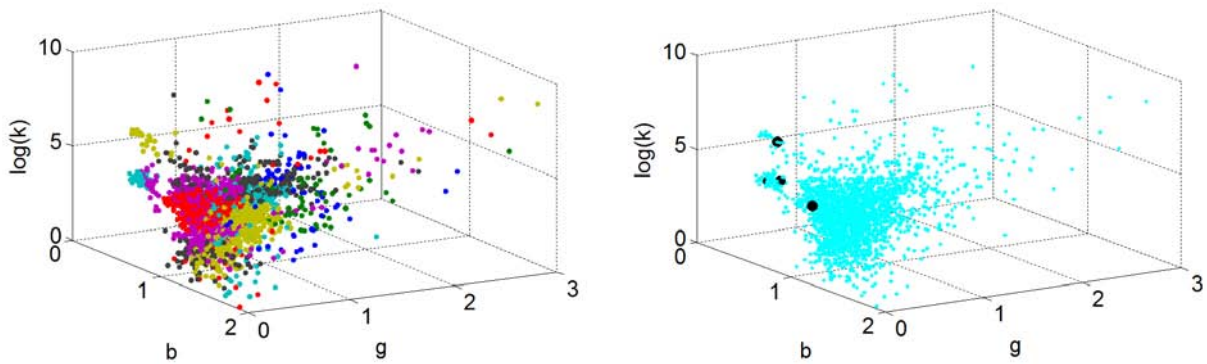

Figure 5.8: Clustering of the EMI features from a single-object inversion for Camp Butner. Left: Results of the first clustering using weighted linkage criteria with Mahalanobis distances. Dots are color-coded by cluster membership. Right: All four identified UXO (black markers) after the second clustering round within a smaller domain (log k $\in$ [2,8], b $\in$ [0.05,2], g $\in$ [0.05,2]) using Ward linkage and Euclidean distances. Two of the four dots belong to the same cluster of 37-mm targets.

The newly acquired data was then used to re-train the GMM-classifier (Step 8) using the features from a precise 3-object EMI inversion set. (Note that, since 3-target inversions provide seven decay curves per anomaly, only the features closest to the centroids of clusters already identified as containing UXO were considered for GMM training.) The results of the updated GMM-based clustering appear in Fig. 5.10. A broadening of the histogram peak corresponding to UXO is observed.

Based on the updated histogram, we requested the ground truth from an additional 20 suspicious items in order to assess statistically the performance of the classifier. The region containing these items had scores between –6 and –5. Here the expert intervened again by visually observing the isosurfaces (and how they encompass the existing UXO clusters) and considering the spread of the histogram peak corresponding to the UXO. (These tasks can potentially be automated to increase process efficiency). At this stage, if all of the 20 items were returned as clutter, the process would stop and the scored items would be used to create the final dig list. However, it turned out that 4 out of 20 items were UXO, and therefore the classifier had to be updated once again to ensure that all possible outliers were accounted for.

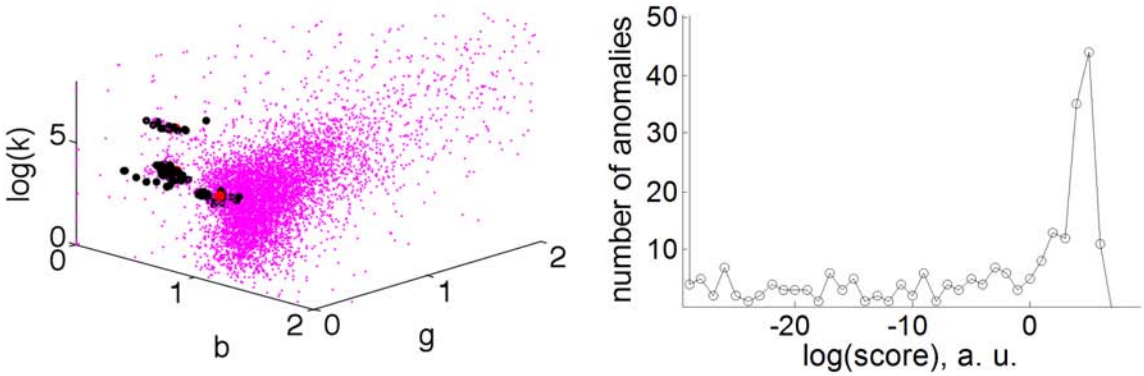

Figure 5.9: Clusters used to train the first GMM classifier and the scoring results. Left: Assumed UXO clusters used to generate the 3-component GMM classifier. There are three clusters, one for each type of UXO. Each cluster is centered close to a target previously identified as UXO (shown as a red dot and visible only for the cluster at center) and contains other anomalies that presumably are dangerous. Right: Histogram of the anomalies sorted by an arbitrary score that measures their likelihood of being UXO. The ground truth was requested based on thresholding the score at an externally selected value close to 0.5.

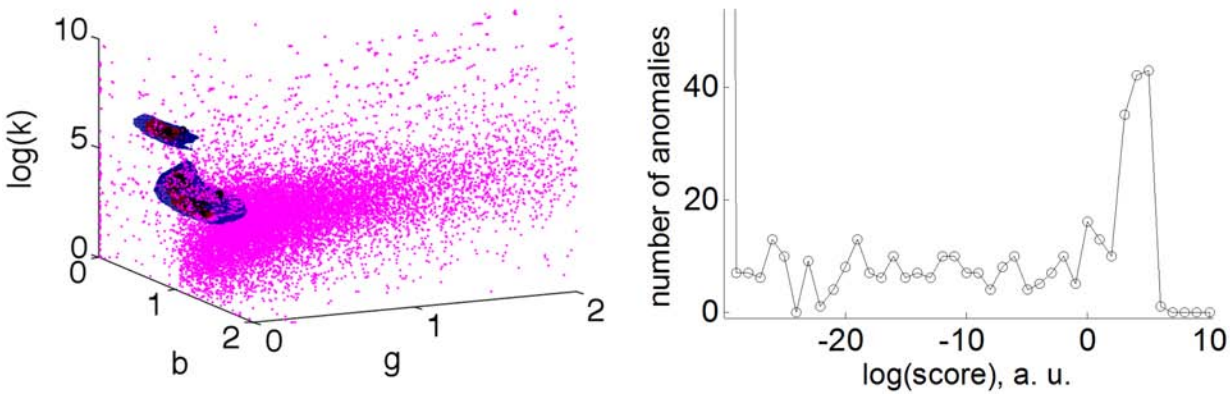

Figure 5.10: Updated GMM classifier after confirming 118 UXO in the Camp Butner data. Left: Score isosurfaces based on the GMM-classifier trained on all currently identified UXO, in the feature space corresponding to 3-object EMI inversion. Right: Score histogram using the new classifier. An additional 20 items were requested to investigate the region corresponding to log(score) within [–6, –5]. (This region was identified by the expert after observing the corresponding score isosurfaces and the histogram).

In order to resolve possible biases from simultaneous treatment of different types of targets, all confirmed UXO were separated into three categories based on their type (105-mm, M48 and 37-mm) and each group was used to train a separate 1-component GMM classifier that was then used to score every target with a separate score for each target type (Step 10). The ground truth was then selected individually for each of the object types, based on threshold score values that once more were identified visually by the expert. Fig. 5.11 presents the results obtained with these individual classifiers for 37-mm, M48 and 105-mm target clusters respectively.

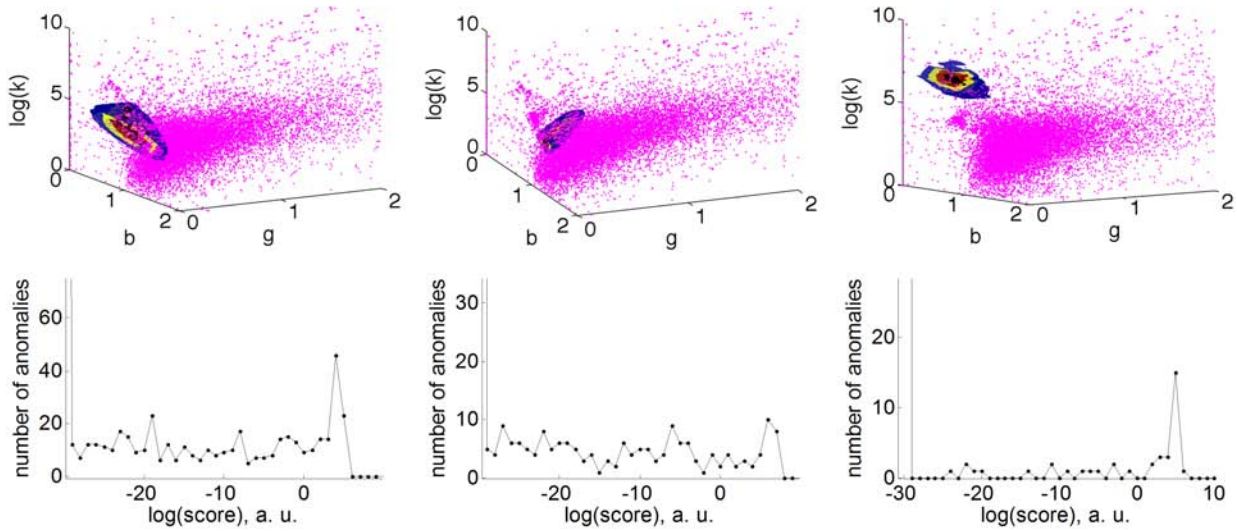

Figure 5.11: The 1-component GMM classifier was then applied to features resulting from 3-object inversion. Left: 37-mm targets; Middle: M48 fuzes; Right: 105-mm targets. The corresponding score histograms are on the bottom row. Initially, 174 anomalies were requested (with 118 being already known) based on the log(score) cutoff value of about –6 for 37-mm targets. After that, 53 anomalies (of which 27 were known) were requested based on a log(score) cutoff value of about –5 for M-48 fuzes. Finally, 36 anomalies (18 of them known already) were requested based on a cutoff of about –20 for 105-mm targets.

The ground truth obtained as a result of Steps 12–11 comprised 322 requested anomalies, of which 160 were confirmed as UXO. At the final stage, a 3-component GMM classifier was trained on the confirmed UXO from the accumulated ground truth and used to score all of the unknown targets (Fig. 5.12). A specific threshold was then selected manually and the final dig list produced. The results of the overall process are summarized in the ROC curve of Fig. 5.13.

5.4.d Conclusions

A hierarchical agglomerative clustering approach combined with Gaussian-mixture probabilistic modeling was applied to a blind UXO test carried out at the former Camp Butner. The ground truth for a total of 322 items was requested in a five-level iterative prediction-correction process. At the end, out of a total of 2291 anomalies, the method yielded 100% accuracy in detecting 171 UXO at a cost of 295 false alarms. Machine-learning techniques therefore hold promise for performing

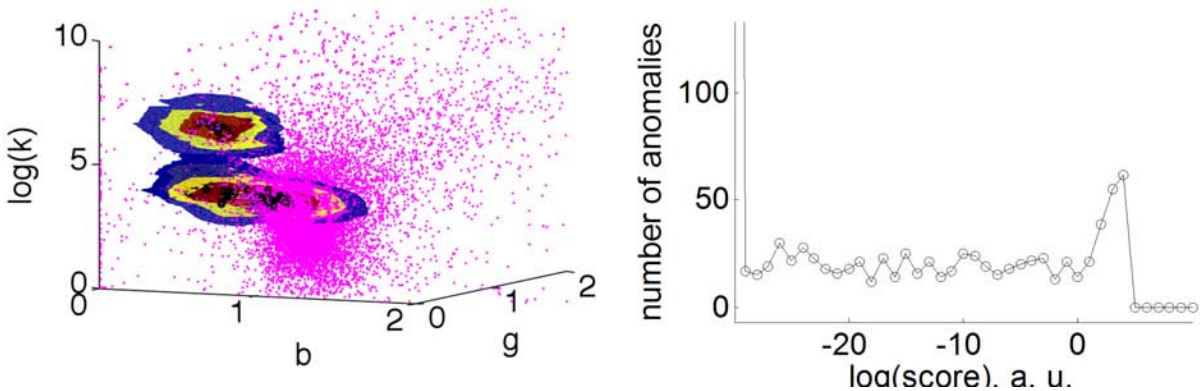

Figure 5.12: Final GMM classifier based on 3-object EMI inversion of Camp Butner data. Left: 3-component GM-classifier score isosurfaces in the classification case based on all already identified UXO targets. Right: Score histogram showing the number of anomalies scored within a particular range of the log(probability density) in arbitrary units. A total of 377 anomalies were scored as UXO based on a log(score) cutoff of about –10. This value was specified by hand to allow enough statistics and sufficient isosurface separation from identified UXO clusters.

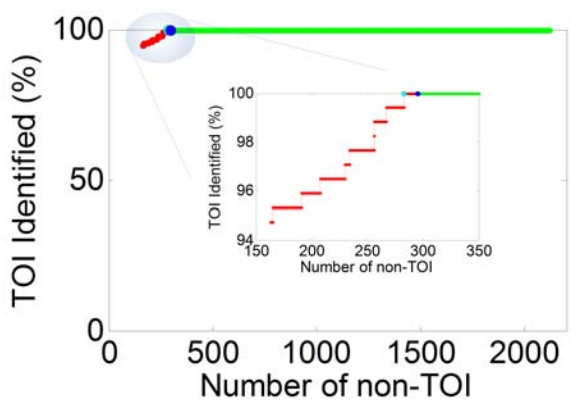

Figure 5.13: ROC curve for Camp Butner live site classification. The total number of anomalies was 2291. One hundred percent of the 171 targets of interest were identified correctly; there were only 295 false positives. The inset zooms in on the region of interest. The dark blue dot corresponds to the stop-digging threshold (the UXO/clutter boundary) suggested by the dig list; the cyan dot specifies the actual position of this boundary. In ideal circumstances the blue and cyan points would coincide, but performing extra digs helps maintain better statistics and improves the results.

high-quality automated UXO discrimination while reducing the workload for human experts and in general speeding up the process.

That said, it would be desirable to improve the process further so it results in even better classification and involves the expert even less. One possibility to reduce the number of false alarms and improve the overall quality of the classification may be to incorporate the symmetry exhibited by UXO by analyzing the decay curves of the *transverse* components of the effective polarizability. It could also be possible to create a library of features from previous discrimination tests; this knowledge, which is already available, could be used to make educated guesses that would help sort out and identify targets of interest in new live sites.

Further improvement of our combined clustering/GMM algorithm must involve ways to perform optimal data clustering, scoring and thresholding automatically. While external inputs from an expert are valuable for guiding the learning process, it is desirable to reduce human judgment to the point where it provides only system-wide quality checks and classification control. An ideal learning mechanism would first exhaust the information contained in the data itself before leaving the crucial decision-making to human experts, who after all are still better than computers at some tasks involving pattern recognition, matching or classification. Such a combined framework may result in overall improved performance and effective resource allocation. A system needing less human input will also be more useful in situations where the operators lack experience, and can potentially help them gain it.

5.5 Camp Beale live-site, hand-held EMI sensors data inversion and classification using advanced EMO models

ESTCP live-site UXO classification results are presented for cued data collected with two advanced EMI instruments, the cart-based 2 × 2 TEMTADS array and the Man Portable Vector (MPV) handheld sensor, at the former Camp Beale in California. There were two sets of targets of interest (TOI): the main set consisted of 105-mm, 81-mm, 60-mm, 37-mm and ISO projectiles, and the other (optional) set comprised site-specific fuzes and fuze fragments of varous sizes. The advanced models used for inversion and classification combine: 1) a joint-diagonalization (JD) algorithm that estimates the number of potential targets generating an anomaly directly from the measured data without need for inversion; 2) the ortho-normalized volume magnetic source (ONVMS) model, which locates targets, represents their EMI responses, and extracts their intrinsic feature vectors; and 3) a Gaussian mixture algorithm that uses extracted discrimination features to classify the corresponding buried objects as TOI or clutter. Initially the data are inverted using a combination of ONVMS and the differential evolution direct-search algorithm; this allows the determination of relevant intrinsic parameters, which in turn are classified by a mixture of clustering and library-matching techniques. This section describes in more detail the main steps of the classification process and demonstrates the results obtained for the 2 × 2 TEMTADS and MPV data taken at Camp Beale, as scored independently by the Institute for Defense Analyses. The advanced models are seen to produce superb classification in both cases.

5.5.a Introduction

In 2011, the Environmental Strategic Technology Certification Program (ESTCP) of the United States military conducted at the former Camp Beale in California the first classification pilot study using recently developed manportable electromagnetic induction (EMI) systems for munitions response [145]. ESTCP chose an area of approximately 10 acres to evaluate both handheld and commercial towed EMI systems. The area was divided into subsections: treed areas to demonstrate man-portable EMI systems performing in cued mode, open areas where the commercially available Geometrics MetalMapper towed array [2] was used (again in cued mode), and an overlap area where both systems were demonstrated. The man-portable systems included the Lawrence Berkeley National Laboratory's portable Berkeley UXO Discriminator (BUD), a 2 2 three-dimensional (3D) man-portable carted version of the Time-domain Electromagnetic Multi-sensor Towed Array Detection System (TEMTADS), developed by the Naval Research Laboratory (NRL) and G&G Sciences [5], and a new verion of the Man-Portable Vector (MPV) handheld system developed by ERDC-CRREL, G&G Scienes, and Sky Research [3, 64, 146–148]. Our group analyzed data taken by the latter two handheld systems.

The MPV-II is an advanced EMI system for UXO detection and discrimination developed and tested under the leadership of Sky Research, designed by the ERDC-CRREL/Dartmouth UXO group and built by G&G Sciences . The system has one transmitter (Tx) circular loop. It uses its own primary magnetic field to perform local positioning by means of a beacon system that provides sub-centimeter accuracy. The system illuminates targets from different directions/sides as it is moved by an operator. It has five 8-cm-side receiver (Rx) cubes that measure the secondary vector dB/dt at each of five spatial points on the plane of the transmitter loop. Thus the system provides fifteen independent transient secondary magnetic field measurements at each instrument

location.

The NRL 2 × 2 TEMTADS time-domain EMI sensor array is a next-generation cart-based portable system designed for subsurface target discrimination. The sensor consists of four Tx/Rx pairs arranged on a 2 2 flat grid, each with a 35-cm square transmitter loop and a coplanar concentric 8-cm-side triaxial receiver cube; the center-to-center separation between neighboring Tx/Rx pairs is 40 cm [5]. The sensor activates the transmitter loops in sequence, one at a time, and for each transmitter all receivers receive, measuring the complete transient response over a dynamic range of time going approximately from 100 microseconds (μs) to 25 milliseconds (ms) and distributed in 123 time gates. The sensor thus provides 48 spatial data points at each location, with high positional accuracy.

Our team processed both data sets independent using the suite of advanced EMI discrimination techniques that we have developed in recent years with support from ESTCP and the Strategic Environmental Research and Development Program (SERDP). Our set of tools for modeling, inversion, and classification combine: 1) a jointdiagonalization (JD) algorithm that estimates the number of potential targets generating an anomaly directly from the measured data without need for inversion [123]; 2) the ortho-normalized volume magnetic source (ONVMS) model (see Sec. 4.4) which locates targets, represents their EMI responses, and extracts their intrinsic feature vectors (in particular, their timedependent total ONVMS amplitudes) and 3) a Gaussian mixture algorithm that uses these extracted discrimination features to classify the corresponding buried objects as TOI or clutter. Initially the data are inverted using a combination of ONVMS and the differential evolution (DE) optimization algorithm [104, 105, 149] to determine the subsurface targets' locations and orientations; this allows the robust determination of their relevant intrinsic parameters, which in turn are classified by a mixture of clustering and library-matching techniques.

During the inversion stage, the total ONVMS is determined as a function of time for each anomaly. The ONVMS model is a further extension of the NSMS model (and hence of the dipole model) that builds on the assumption that the superposition of EMI responses of a collection of buried objects interrogated by a sensor can be represented as though it originated from a set of magnetic dipoles distributed over a volume.

Since all actual radiating sources are located within the scatterers-rather than in the soil or air-the spatial distribution of these fictitious dipoles indicates the locations and orientations of any targets present inside the computational volume. The great advantage of the ONVMS technique over the other models discussed above is that it takes into account mutual couplings between different sections of the different targets while simultaneously avoiding the appearance of singular matrices in multi-target situations. It is thus gracefully indifferent to the number of targets: Once the amplitudes and the locations of the corresponding dipoles are determined, one need only look at their clustering patterns, compute the time-dependent total polarizability tensor for each group, and subsequently diagonalize each of the tensors using JD. The resulting diagonal elements have been found to be intrinsic to the objects they represent, and can be used, on their own or combined with other quantities, in discrimination analysis. Recent ESTCP live-site discrimination studies have clearly indicated the superior discrimination performance of the ONVMS method in combination with statistical processing [119].

The section is organized as follows: Sec. 5.5.b describes the protocol used to invert 2 × 2 TEMTADS data, extract target features, and cluster and classify targets; it then presents and the TEMTADS classification results obtained in the Camp Beale blind test. Sec. 5.5.c describes the analysis procedure and the Camp Beale classification results obtained starting from MPV-II data.

Sec. 5.5.d provides a brief discussion and some conclusions.

5.5.b 2 × 2 TEMTADS Data Sets Data Inversion and Classification Scheme

The 2 × 2 TEMTADS area is a next-generation portable EMI system. The instrument's electronics, geometry, data collection procedure, and file formats are described in [4]. For the Camp Beale 2 × 2 TEMTADS cued data we applied the following inversion and classification protocol described above for the MM data sets.

1. Transfer all CSV files generated by the sensor to an ASCII-based format compatible with our TEMTADS ONVMS-DE code.

2. Construct the 2 × 2 TEMTADS multistatic response (MSR) data matrix as described in [123].

3. Apply JD to the 2 × 2 TEMTADS MSR data matrix to extract its time-dependent eigenvalues. Conduct an eigenvalue analysis to ascertain the quality of data and determine the number of potential targets in each cell. Figures 5.14 and 5.15 depict the TEMTADS time-dependent MSR eigenvalues for some camp Beale anomalies. Featured are an ISO, a 37-mm, a 60-mm, a 81-mm, and a sample magnetic soil. The results show that the 2 × 2 TEMTADS MSR eigenvalues are intrinsic properties of the targets. Each target has very distinguishable eigenvalues that stay the same even when the signal is contaminated with signals from nearby targets (see Fig. 5.14). We used the eigenvalues' characteristics directly to perform an initial classification. Figure 5.15 shows that the MSR eigenvalues also provide fast and robust information about the data quality. For example, comparing Case-352 with Case-356 (second column of Fig. 5.15) shows that when the sensor is well positioned above the target the eigenvalues are strong and well above the noise level; on the other hand, when the sensor is offset from the target the eigenvalues become noisy and mix with those of the soil (see Case-382 in the bottom left panel of Fig. 5.15). In order to avoid misclassification, those anomalies were placed into a training data list. Our studies [1, 119] also indicate that, as the number of targets producing an anomaly increases, so does the number of time-dependent MSR eigenvalues above the noise level. The anomalies with a significant number of eigenvalues (six or more) above the noise level were also included in the training data; the 2 × 2 TEMTADS MSR eigenvalues for one such case are shown in Fig. 5.16. The left panel of Fig. 5.16 shows that there are no clear background-related eigenvalues (i.e., eigenvalues that have similar magnitude variations for all time channels), and there are at least seven distinguishable eigenvalues. For these two reasons we included the anomaly in the training data list. The received ground truth revealed that the cell contained five targets, including a 3-cm fuze part that was ranked as a TOI by ESTCP.

4. Extract the total ONVMS for each anomaly. We ran the ONVMS/DE code and extracted the targets' parameters, both intrinsic and extrinsic (i.e., their burial depths). The extracted total ONVMS for the 3-cm fuze part from Test Case-758 using a five-target inversion code is depicted in the right panel of Fig. 5.16. We see that the total ONVMS decays fast and is not symmetric, which could be explained by the signal contamination level. The ground truth shows that the signal is indeed contaminated significantly, since the TOI is smaller than the clutter and buried deeper. Even in these circumstances our model was able to extract

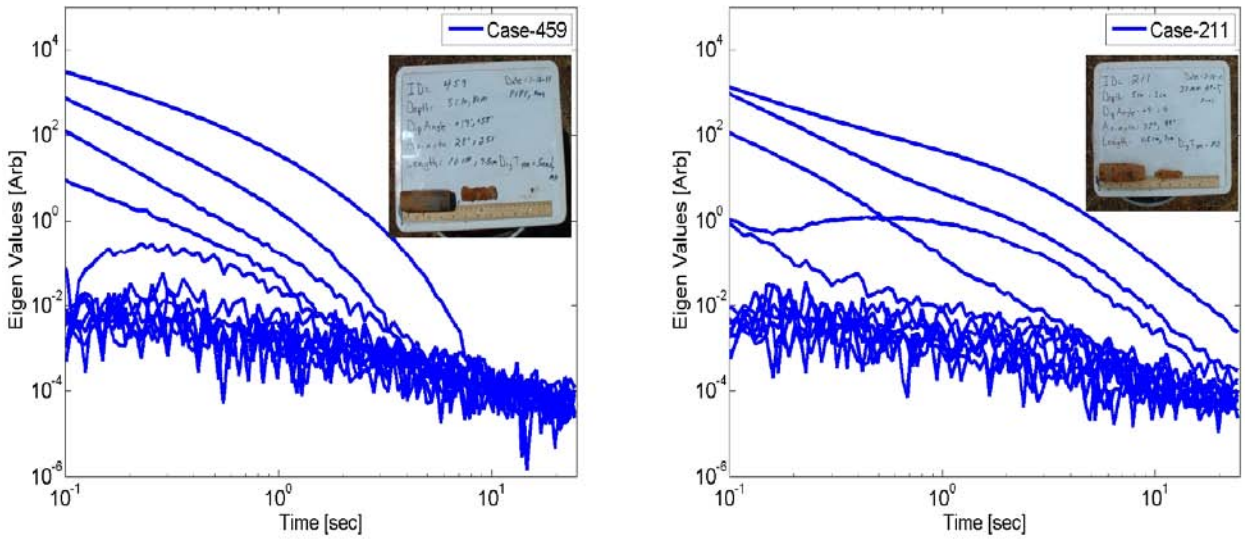

Figure 5.14: Camp Beale 2 2 MSR eigenvalues versus time for two-target cases involving ISO and 37-mm TOI.

meaningful parameters. This extracted ONVMS was then used to identify other similar fuze parts (seven in total).

5. Create a custom training list. To create the custom training list we used parameters that could describe the size and the decay rate of the total ONVMS curves (respectively, the inverted ONVMS at the first time channel and the ratio of the inverted total ONVMS at the first time channel to that at the 80th). The left panel of Fig. 5.16 contains a scatter plot of log10[Mzz(t1) / Mzz(t80)] vs. log10[Mzz(t1)] for the data set. To cluster the anomalies we applied statistical classification to the size and decay distributions using a Matlab built-in function. The clustering results appear in the right panel where each color/circle corresponds to a cluster. In addition, we inspected the eigenvalues and ONVMS time-decay curves for each anomaly to further validate or override the custom training anomaly list.

6. Request the ground truth for selected anomalies. The custom training list we created using a combination of JD, clustering, and ONVMS-DE inversion results was submitted to the ESTCP office, who provided us with the ground truth for the corresponding anomalies (a total of 98). We used this ground truth to identify the possible TOI types and their variations in size. This information we then used to generate a second list of training anomalies.

7. Create a ranked dig list. Using the ground truth from the previous step and the inverted total ONVMS for each 2 × 2 TEMTADS data file we created a library for 105-mm, 81-mm, 60-mm, 37-mm, and ISO munitions, as well as fuzes and fuze parts. The inverted total ONVMS for the anomalies that were classified as TOI appear in Fig. 5.18 and Fig. 5.19.

8. Submit the dig list to ESTCP. We used the clustering and library-matching techniques to classify anomalies as containing TOI or not and submitted the resulting ranked list to the

IDA for scoring. The scored results for the 911 TEMTADS anomalies shown on Fig. 5.20 (a) and (b), which respectively assume the fuze parts to be clutter and TOI. Of the 99 targets that were dug for training, 75 were not TOI (shift along x-axis) and 24 were (shift along yaxis). There were no false negatives: all TOI (a total of 124, of which 89 were UXO/ISO and 35 were fuzes) were classified correctly. To classify all TOI correctly, an extra 116 (false positive) digs were needed; 596 anomalies (76% of 787 clutter items) were identified with high confidence as containing no TOI.

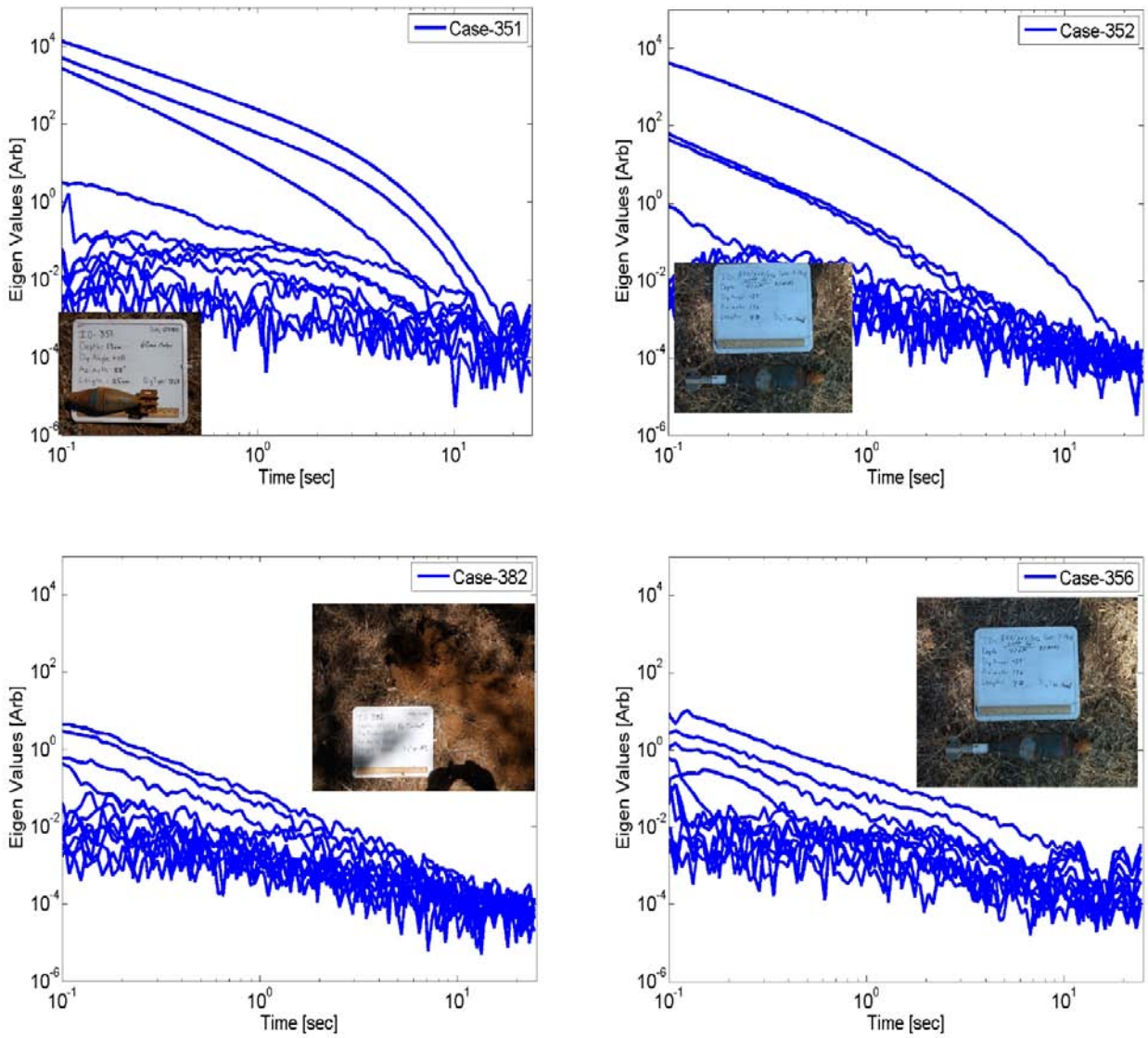

Figure 5.15: Camp Beale 2 2 MRS data matrix eigenvalues versus time for a 60-mm, an 81-mm, and a sample of magnetic soil.

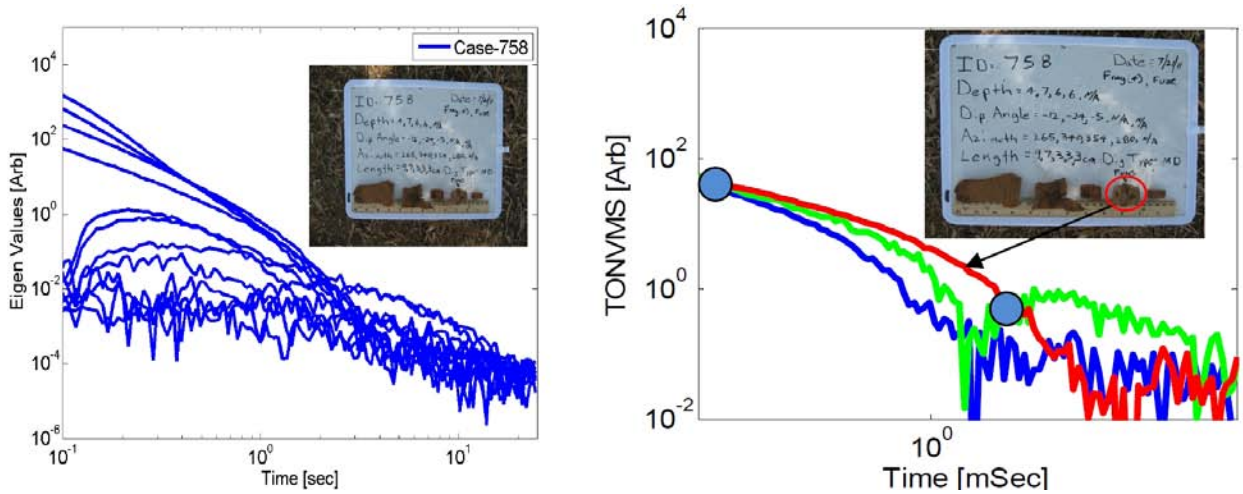

Figure 5.16: Left: Camp Beale 2 × 2 TEMTADS MSR data matrix eigenvalues versus time for Test Case 758. Right: Total ONVMS for the 3-cm fuze part from Test Case-758 extracted using a five-target inversion code.

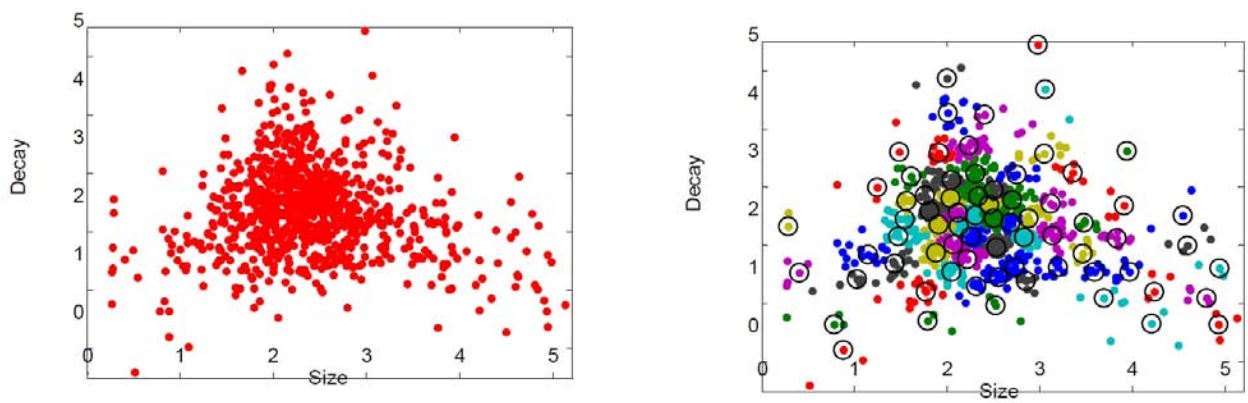

Figure 5.17: (Left) Scatter plot of size (log10[Mzz(t1)]) and decay (log10[Mzz(t1)/Mzz(t80)]) parameters for all Camp Beale 2 × 2 TEMTADS anomalies based on the extracted total ONVMS. (Right) Result of the supervised clustering classification for the anomalies using the size and shape information in the panel at left.

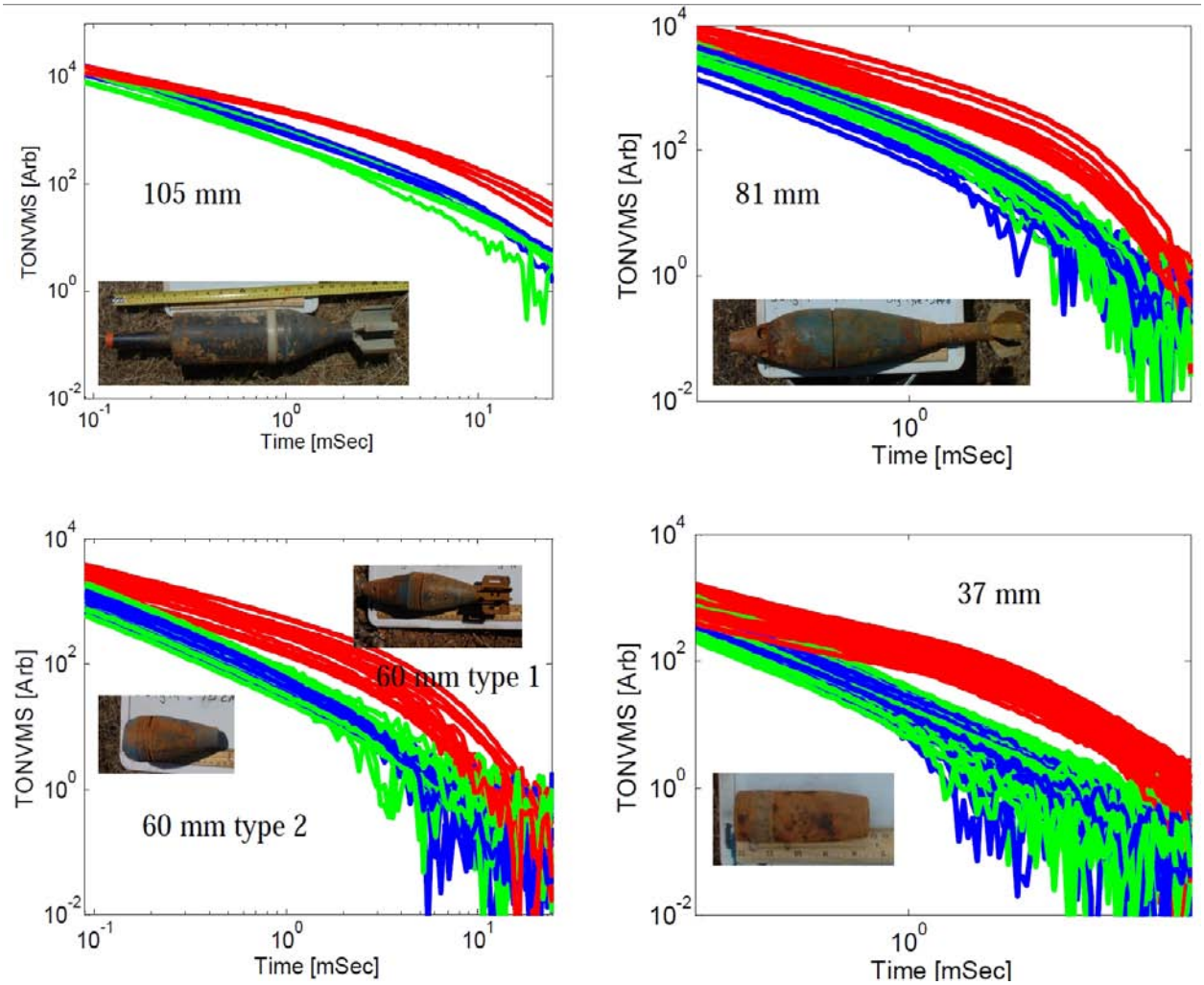

Figure 5.18: Total ONVMS time-decay curves for the 105-mm, 81-mm, 60-mm and 37-mm TOI buried at Camp Beale and interrogated by the 2 × 2 TEMTADS array.

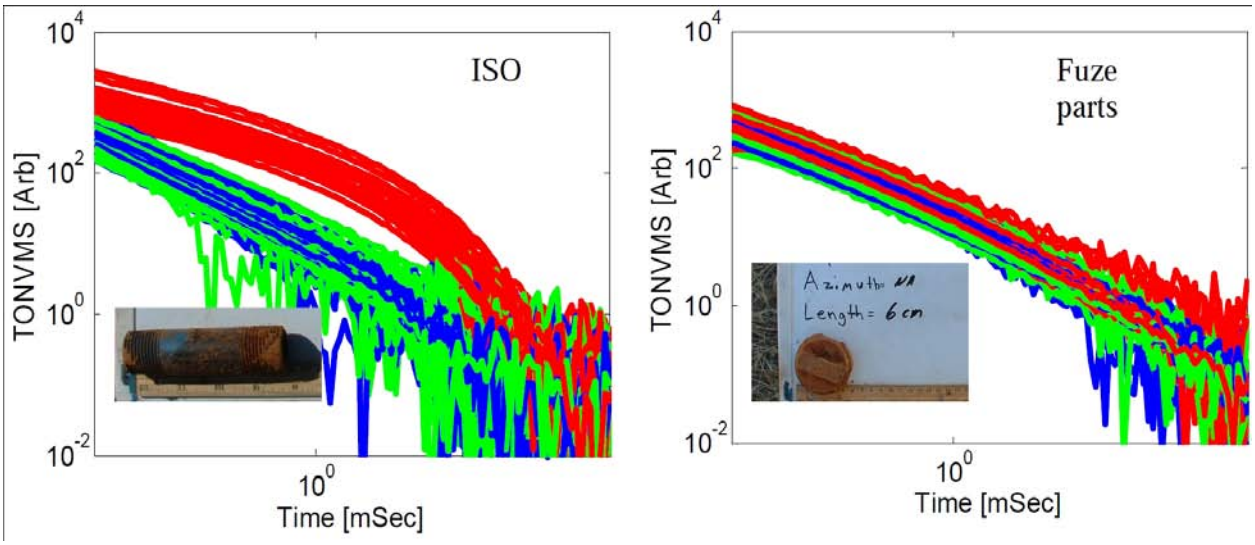

Figure 5.19: Total ONVMS time-decay curves for the ISO targets and fuze parts at Camp Beale as determined starting from 2 × 2 TEMTADS data.

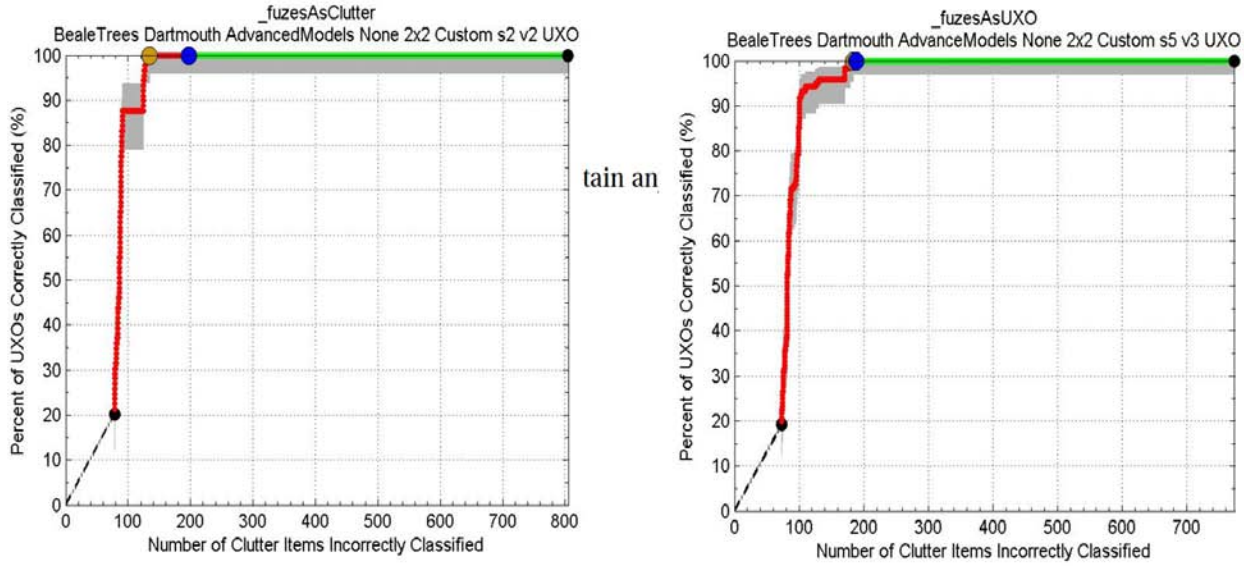

tain an

Figure 5.20: ROC curve for the Camp Beale 2 × 2 TEMTADS anomalies as identified by our procedure: (a) Taking the fuzes to be clutter; (b) Treating the fuzes as TOI.

5.5.c Inversion and Classification Scheme for MPV-II Data

The man portable vector MPV-II is an advanced handheld EMI system, originally developed by ERDC-CRREL, G&G Sciences, and Dartmouth College under SERDP Project 1443. The advanced EMI models have been adapted to this instrument and tested with various lab and test-site data sets. The inversion and classification analysis of the Camp Beale MPV-II cued data was done following the same steps enumerated above:

1. Extract total ONVMS for each anomaly.
2. Create a custom training list: We used size and decay parameters (taking the 25th time channel for the latter) as inputs to the statistical classification technique that clustered the anomalies using a Matlab built-in function.
3. Request ground truth for selected anomalies. We created a custom training list using combination of clustering and ONVMS-DE inversion results. The list was submitted to the ESTCP office and the ground truth for training anomalies was received.
4. Create ranked dig list. Using the ground truth of custom identified training anomalies (a total of 95) and the inverted total ONVMS for each case we created a library for the different munitions, fuzes, and fuze parts. The inverted total ONVMS for the anomalies that were classified as TOI appear in Fig. 5.21.
5. Submit the dig list to ESTCP. Using the clustering and library-matching techniques we classified the anomalies as TOI or non-TOI. The ranked list was submitted to the IDA for scoring; the results are shown on Fig. 5.23 (a) and (b), which respectively assume the fuze parts to be clutter and TOI.

The scored results for the 911 Camp Beale MPV-TD anomalies, depicted in Fig. 5.23, show that a) of the 95 targets that were dug for training, 79 were not TOI (shift along x-axis) and 16 were TOI (shift along y-axis); b) no false negatives: all TOI (124, of which 89 were UXO/ISO and 35 were fuzes) were classified correctly; c) to classify all TOI correctly one needed 121 extra (false positive) digs; d) 587 (~75 % of clutter items out of 787) were identified as non-TOI with high confidence.

5.5.d Conclusion

As part of its effort to make UXO remediation faster and more economic, ESTCP is in the process of administering a series of blind classification tests of increasing realism to measure the progress made in the development of sensors and inversion and classification algorithms. The latest of these tests took place at the former Camp Beale in California. Among the next-generation EMI sensing instruments used for the test were the 2×2 TEMTADS array and the MPV-II, both of which were used to collect data in cued mode at the live site. We analyzed the data from both instruments using an advanced EMI/statistical analysis protocol that 1) estimates how many targets are producing an anomaly using inversion-free joint diagonalization, 2) locates and characterizes the targets using a combination of the ONVMS model and DE optimization, and 3) classifies the targets (and, in particular, discriminates between TOI and clutter) using total ONVMS amplitudes as

inputs to a Gaussian mixture algorithm. We also used library matching and statistical classification techniques. The classification step used custom training data lists created independently for each sensor.

Our classification results for both sets of data were scored independently by the Institute for Defense Analyses. The advanced models were found to produce exceptional classification using the two sensors. Our methodology was able to achieve 100% target-of-interest classification while rejecting about 80 percent of the nonhazardous clutter. Our team was the only group able to classify all main and optional TOI correctly.

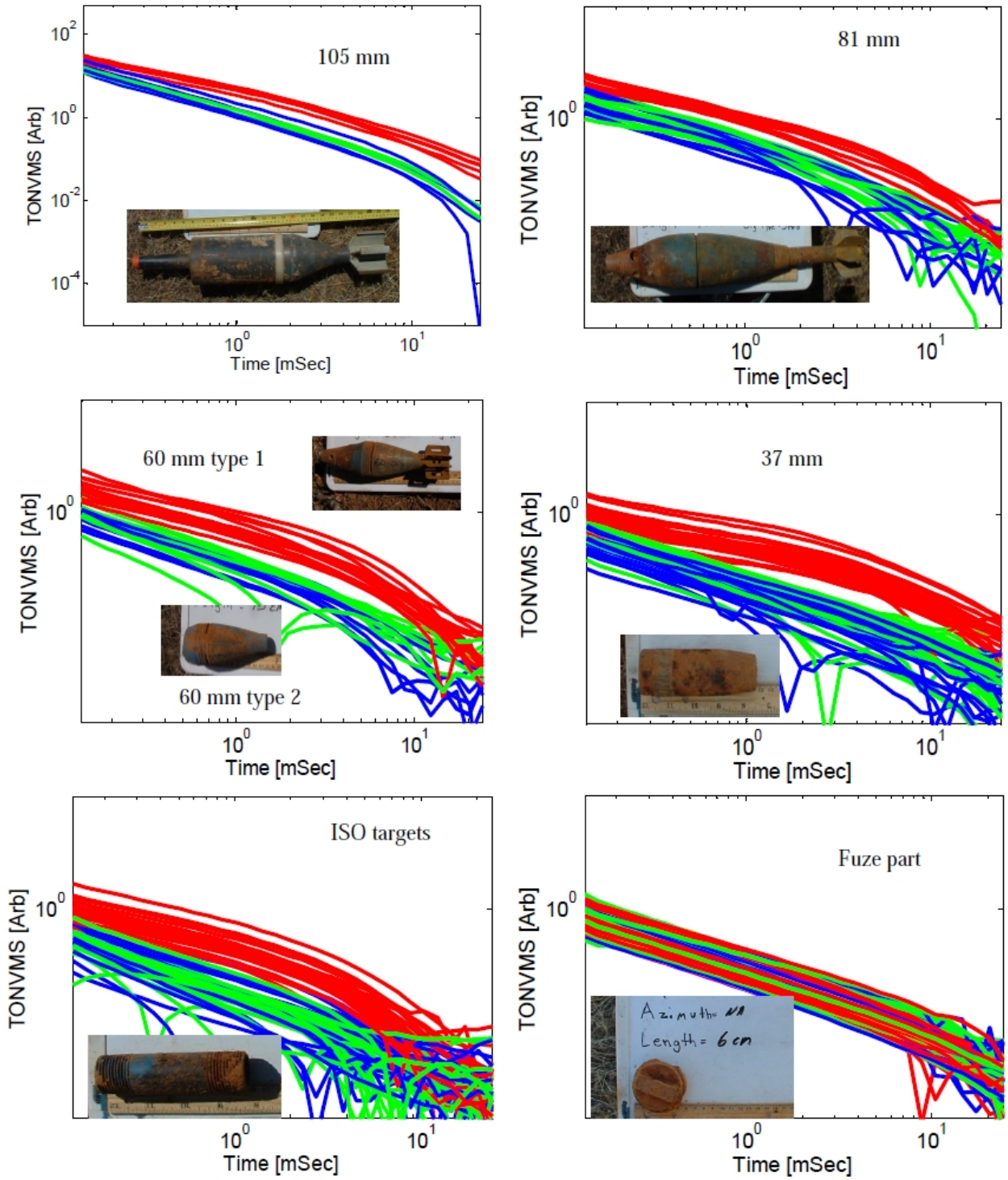

Figure 5.21: Time-dependent total ONVMS, inverted from MPV-II data, for the Camp Beale 105-mm, 81-mm, 60-mm 37-mm, and ISO munitions and for the fuze parts identified as potential TOI by ESTCP.

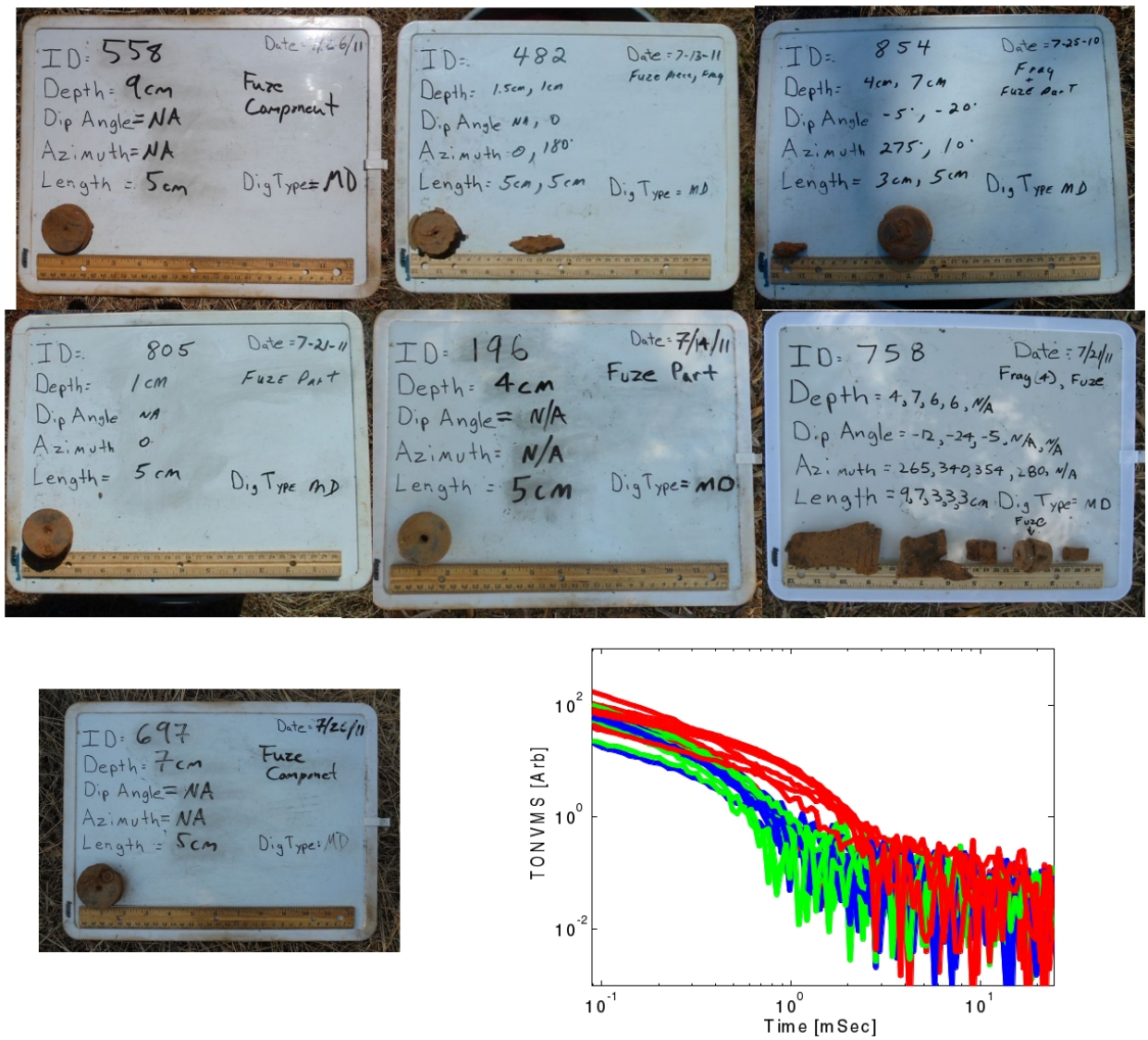

Figure 5.22: Images of seven small fuze parts that were identified as TOI by the ESTCP office. The bottom-right panel has the inverted total ONVMS for all these seven small fuze parts.

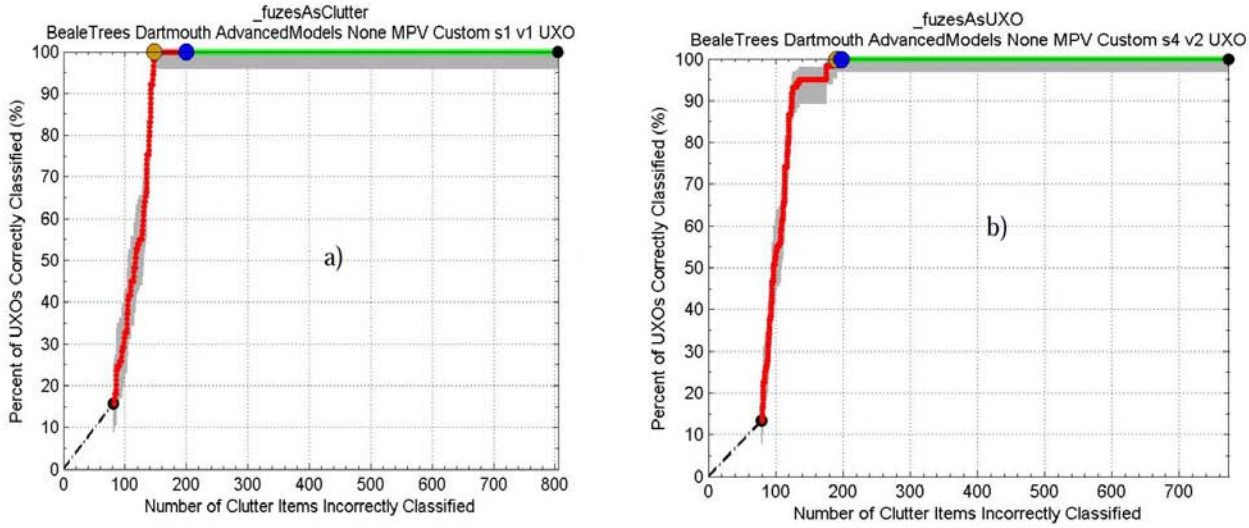

Figure 5.23: ROC curve for the Camp Beale MPV-II anomalies, (a) assuming the fuzes to be clutter and (b) considering them as TOI.

6 Conclusions and Implications for Future Research/Implementation

SERDP project MR-1664 entitled "Isolating and Discriminating Overlapping Signatures in Cluttered Environments" is complete. We have developed two major methods of finding multiple targets in EMI data even when the targets are in close proximity. The multiple dipole Jacobian based gradient search method (see Sec. 4.2) finds multiple targets by assuming that each target exhibits a dipolar response. A gradient search algorithm then searches for these multiple sources. This method needs to know the number of targets in order to perform accurately. The JD method provides this estimate for N to either the Jacobian search method or the ONVMS method. The ONVMS method (see Sec. 4.4) searches for dipole like (but orthonormal) sources in the data without inversion difficulties arising from solving linear systems. Both of these methods are able to distinguish at least six different targets in EMI data from modern time domain instruments. The combined JD and ONVMS method (together with expert guidance) performed very well at the Camp Butner and Camp Beale demonstration sites.

A Appendices – Supporting Data

A.1 MPV Single Target Blind Test Results

We collected data using the MPV1 instrument over several single target cases as a blind test for our models. During the data collection, we employed the laser positioning system to locate our data though we used a grid as a rough guide when we moved the MPV instrument itself. We took data at two heights, separated by 10 cm or two blue board thicknesses. At each height and after acquiring background data, we took a total of 17 measurement in a four by four grid followed by a single shot located precisely on our grid. We used this last data point to define a global coordinate system for each set of 17 data points. The true locations and orientation of the five targets are given in Table 11. These results are very encouraging for single target cases even considering only 5 data shots (=75 data points) from the MPV. Sample results, presented at Partners 2007, are given in Fig. A.1.

Target	ID	x_0 (cm)	y_0 (cm)	z_0 (cm)	ϕ (°)	dip (°)
1	81-mm	−23.26	22.5	56.16	0	−18.3
2	105-mm	−20.26	22.5	69.14	180	−18.6
3	BLU26	0.00	22.5	43.21	0	0.0
4	57-mm	5.22	22.5	51.45	180	306.6
5	60-mm	0.00	22.5	54.50	0	0.0

Table 11: Correct answers for the blind-test data runs.

Target	ID	x_0 (cm)	y_0 (cm)	z_0 (cm)	ϕ (°)	dip (°)
1	81-mm	-21.2	23.6	56.56	0	−2
2	105-mm	- 6.0	23.7	67.57	170	−20.8
3	BLU26	0.25	21.8	47.55	*0	*180
4	57-mm	0.75	21.6	58.19	0	320.4
5	60-mm	0.67	19.3	54.02	*3	0

Table 12: NSMC model inversion results for position and orientation for blind test data. Numbers with an asterisk are arbitrary due to BOR considerations.

A.2 Previous Multiple Target Inversion Results

Though we would not use the GEM-3 for the research proposed here, our prior work in this area involves GEM-3 data.

We acquired data using the GEM-3 instrument in 2005 over 9 sets of targets in the CRREL test plots. In each test hole, we emplaced either 1 UXO and 1 piece of clutter, or 2 UXOs. We then acquired data at two elevations over each test hole and used these data in a blind test. Sample data from one of the test holes is shown in Fig. A.2. As can be seen from the picture, it is not at all clear by eye how many targets are present in the data much less where they are located. The NSMC model was used to simultaneously invert for the positions, orientations and Q (or the total NSMC) for each of these test holes. Results are shown in Fig. A.3. The NSMC algorithm was able to discriminate between targets in close proximity in some cases, but in others, the results were less clear.

While encouraging this study provides an excellent example of the problems faced when signals from objects overlap [14, 18, 134]. These problems include positional uncertainties, scalar

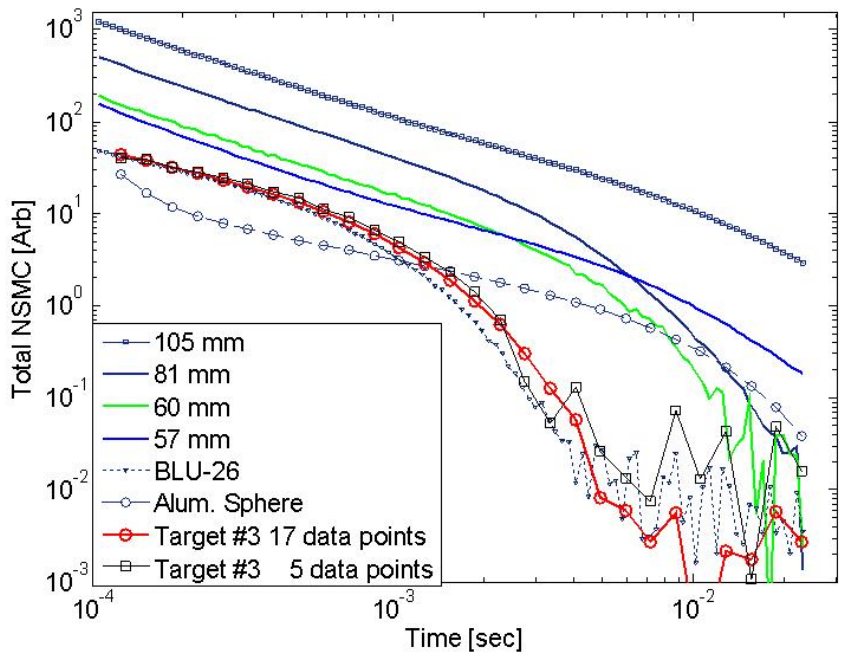

Figure A.1: NSMC model comparison to library for blind test #3.

data, and sensor limitations. The research conducted under MR-1664 helped overcome these limitations with clutter mitigation techniques, an N-target locator, and more diverse, higher quality data.

A.2.a GEM-3 Data over 2 UXO

Data were collected on a 7x7 grid at two heights above each test hole. The NSMC was then used in an iterative fashion in an attempt to discriminate both UXO simultaneously.

A.2.b Projection of GEM-3 Data over 1 UXO Obscured by Clutter

Data projection involves using the data from mono-static or multi-static instruments to achieve the same purpose as that for bistatic instruments, that is, to use data at lower elevations (closer to clutter) to provide estimates on what data would look like if acquired at higher elevations (farther from clutter). An early attempt at a data projection technique for GEM-3 data is described here.

We acquired data from a 105mm UXO (Fig. A.4) which was obscured by the clutter layer affixed to a plywood substrate as shown in Fig. A.5. The clutter layer was situated 5cm above the upmost part of the UXO, and GEM-3 measurements were taken at 2 heights: 15cm and 20 cm above the upmost part of the UXO respectively. The H_z at 90Hz from the GEM-3 is shown at these two height in Fig. A.6 (top subfigures). Using our preliminary upward projection technique, we were able to use these data at lower heights to estimate data as if acquired at higher elevations (in this case 25cm and 30cm above the UXO). These projected in Fig. A.6 (bottom subfigures) show the diminished influence of the clutter layer as a function of height. Note that this clutter layer is an

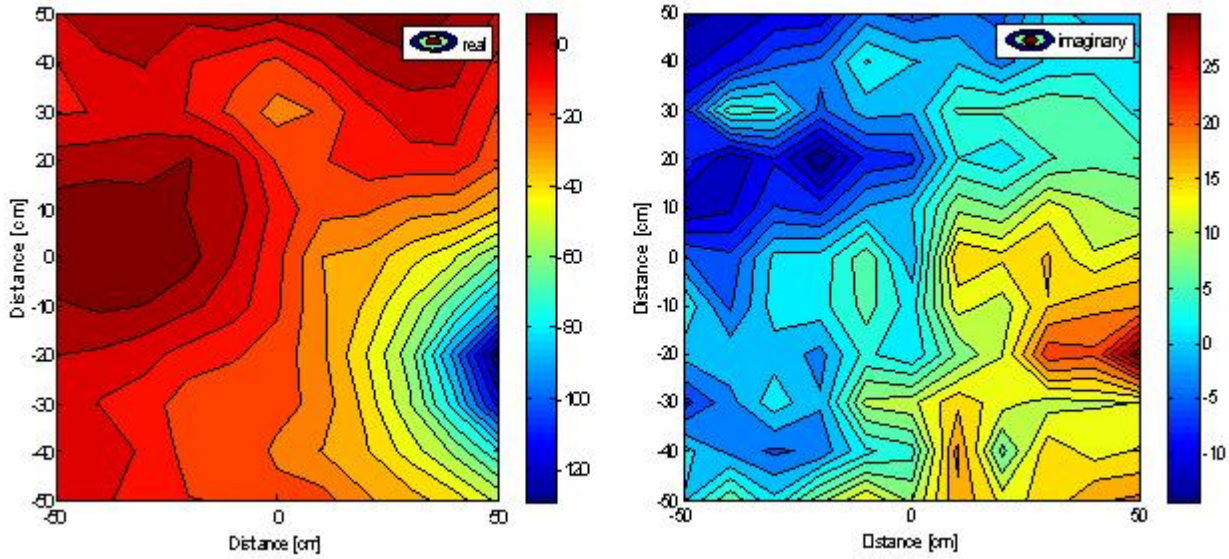

Figure A.2: GEM-3 data acquired over 2 buried targets.

extreme case (to begin with) and reacts almost as a sheet of dispersed clutter, which has a different power law than discrete targets [150].

The decay of the projected data for both the UXO+clutter case and the clutter only case both approach the same power law. This suggests that the higher up the data is projected, the less the influence the clutter has until only the EMI response from the UXO is non-negligible. This effect may be exploited for use in discrimination and needs further research.

A.3 Simplified Model of the MSR Matrix

We consider an idealized version of TEMTADS consisting of a 5×5 array of vertical dipoles of unit moment $\hat{\mathbf{z}}$—corresponding to a combination of unit current and unit area—each of which at a given time gate transmits a primary field

$$\mathbf{H}^{\mathrm{pr}} = \frac{1}{4\pi R^5}\left[3(\hat{\mathbf{z}}\cdot\mathbf{R})\mathbf{R} - \hat{\mathbf{z}}R^2\right] = \frac{3ZX}{4\pi R^5}\hat{\mathbf{x}} + \frac{3ZY}{4\pi R^5}\hat{\mathbf{y}} + \frac{3Z^2 - R^2}{4\pi R^5}\hat{\mathbf{z}}, \tag{A.3.1}$$

where $\mathbf{R} \equiv X\hat{\mathbf{x}} + Y\hat{\mathbf{y}} + Z\hat{\mathbf{z}} = \mathbf{r} - \mathbf{r}_t$, $\mathbf{r}$ is an observation point, and $\mathbf{r}_t$ is the location of the transmitter. Each TEMTADS dipole receives from a buried source a response $\mathbf{H}^{\mathrm{sc}}$ whose z-component reads

$$H_z^{\mathrm{sc}} = \frac{1}{4\pi R^5}\left(3(\mathbf{m}\cdot\mathbf{R})\mathbf{R}\cdot\hat{\mathbf{z}} - \mathbf{m}\cdot\hat{\mathbf{z}}R^2\right) = \frac{1}{4\pi R^5}\left[3(\hat{\mathbf{z}}\cdot\mathbf{R})\mathbf{R} - \hat{\mathbf{z}}R^2\right]\cdot\mathbf{m}, \tag{A.3.2}$$

where now $\mathbf{R} = \mathbf{r}_r - \mathbf{r}$ with $\mathbf{r}_r$ the location of the receiver. Note that the expressions in square brackets in equations (A.3.1) and (A.3.2) coincide if and only if the (infinitesimal) transmitters and receivers are co-located, as is the case with TEMTADS. The moment $\mathbf{m}$ induced in the responding source is given as in (4.4.5). The MSR matrix for the transmitter/receiver array is constructed by

Tasks #	Inverted targets		Ground truth	
	Object #1	Object #2	Object #1	Object#2
1		Clutter	Correct	Correct
2		Clutter	Correct	Correct
3		Clutter	Incorrect	Correct
4		Clutter	Incorrect	Correct
5			Correct	Correct
6			Correct	Incorrect
7			Incorrect	\ Correct
8		An aluminum plate ??	Correct	Incorrect
9			Incorrect	Correct

Figure A.3: GEM-3 data inversion results from Partners poster 2006.

assembling N_t samples of (A.3.1) for the transmitted field and N_r samples of the received response (A.3.2), thus forming the Green tensors

$$\mathbf{G}^{\mathrm{pr}} = \begin{bmatrix} \frac{3ZX}{4\pi R^5} & \frac{3ZY}{4\pi R^5} & \frac{3Z^2-R^2}{4\pi R^5} \end{bmatrix} \in \mathrm{R}^{N_t \times 3}, \tag{A.3.3}$$

$$\mathbf{G}^{\mathrm{sc}} = \begin{bmatrix} \frac{3ZX}{4\pi R^5} & \frac{3ZY}{4\pi R^5} & \frac{3Z^2-R^2}{4\pi R^5} \end{bmatrix} \in \mathrm{R}^{N_r \times 3}. \tag{A.3.4}$$

The measured secondary signal given in equation (4.3.1) is

$$\mathbf{S} = \mathbf{G}^{\mathrm{sc}}(\mathbf{U}\boldsymbol{\Lambda}\mathbf{U}^T)(\mathbf{G}^{\mathrm{pr}})^T = (\mathbf{G}^{\mathrm{sc}}\mathbf{U})\boldsymbol{\Lambda}(\mathbf{G}^{\mathrm{pr}}\mathbf{U})^T, \tag{A.3.5}$$

where $\mathbf{U}$ and $\boldsymbol{\Lambda}$ are 3×3 matrices.

We can use this simplified model to provide a plausibility argument for one of our findings: targets with cylindrical or spherical symmetry have a pair of eigenvalues whose log-log decay curves look parallel (i.e., there is a constant ratio between the two). Take $\mathbf{G}^{\mathrm{pr}}$ and $\mathbf{G}^{\mathrm{sc}}$ to be identical, as the geometry above demands, and consider a 2×2 sensor array such that the Tx/Rx pairs are located at $\mathbf{r}_i = \ell(\pm\hat{\mathbf{x}} \pm \hat{\mathbf{y}})$, where $\ell = 0.20$ cm in the case of TEMTADS. Suppose the target is a dipole buried at depth z_0 below the center of the array and characterized by the cylindrically

Figure A.4: 105mm UXO under clutter layer.

Figure A.5: Dense clutter layer affixed to plywood substrate.

symmetric polarizability tensor $\mathbf{\Lambda} = \beta\ \mathrm{diag}(1,1,\lambda)$. Ordering the Tx/Rx dipoles clockwise from the top left of the array, we obtain the MSR matrix

$$\mathbf{S} = \beta \left(\frac{3z_0\ell}{4\pi R^5}\right)^2 \begin{bmatrix} -1 & 1 & \kappa \\ 1 & 1 & \kappa \\ 1 & -1 & \kappa \\ -1 & -1 & \kappa \end{bmatrix} \mathbf{U}\mathbf{\Lambda}\mathbf{U}^T \begin{bmatrix} -1 & 1 & 1 & -1 \\ 1 & 1 & -1 & -1 \\ \kappa & \kappa & \kappa & \kappa \end{bmatrix}, \tag{A.3.6}$$

where we have introduced the dimensionless parameter

$$\kappa = \frac{3z_0^2 - R^2}{3z_0\ell} = \frac{2}{3}\left(\frac{z_0}{\ell} - \frac{\ell}{z_0}\right), \quad \text{which implies} \quad z_0 = \frac{\ell}{4}(3\kappa + \sqrt{9\kappa^2+16}). \tag{A.3.7}$$

If the target is a horizontal dipole, the polarizability tensor is $\mathbf{U}\mathbf{\Lambda}\mathbf{U}^T = \beta\ \mathrm{diag}(\lambda,1,1)$ and the MSR matrix A.3.6 becomes

$$\mathbf{S} = \beta \left(\frac{3z_0\ell}{4\pi R^5}\right)^2 \begin{bmatrix} (1+\lambda)+\kappa^2 & (1-\lambda)+\kappa^2 & -(1+\lambda)+\kappa^2 & -(1-\lambda)+\kappa^2 \\ (1-\lambda)+\kappa^2 & (1+\lambda)+\kappa^2 & -(1-\lambda)+\kappa^2 & -(1+\lambda)+\kappa^2 \\ -(1+\lambda)+\kappa^2 & -(1-\lambda)+\kappa^2 & (1+\lambda)+\kappa^2 & (1-\lambda)+\kappa^2 \\ -(1-\lambda)+\kappa^2 & -(1+\lambda)+\kappa^2 & (1-\lambda)+\kappa^2 & (1+\lambda)+\kappa^2 \end{bmatrix}. \tag{A.3.8}$$

The eigenvalues of this 4×4 matrix are 0, 4, $4\kappa^2$, and 4λ. One eigenvalue vanishes, confirming that there is only one target. The nonzero eigenvalues are in general not degenerate, even for highly symmetric configurations. (The eigenvalues coincide for the special case $z_0 = 2\ell$.) On the other hand, there is a constant *ratio* κ^2 between two of the eigenvalues, allowing extraction of the "extrinsic" depth z_0 through the definition A.3.7. (Cylindrical symmetry is important here; if $\mathbf{\Lambda} = \beta\ \mathrm{diag}(1,\mu,\lambda)$ the MSR eigenvalues become 0, $4\kappa^2$, 4μ, and 4λ, with all significant ratios now time-dependent.) This undertaking quickly becomes nontrivial: for example, when the target is vertical, the MSR eigenvalues are 0, 4, 4, and $4\lambda\kappa^2$; the intrinsic and extrinsic features are coupled. The analysis is further complicated if the target is displaced from the center of the Tx/Rx array or has another orientation or if the Tx/Rx array is larger than 2×2.

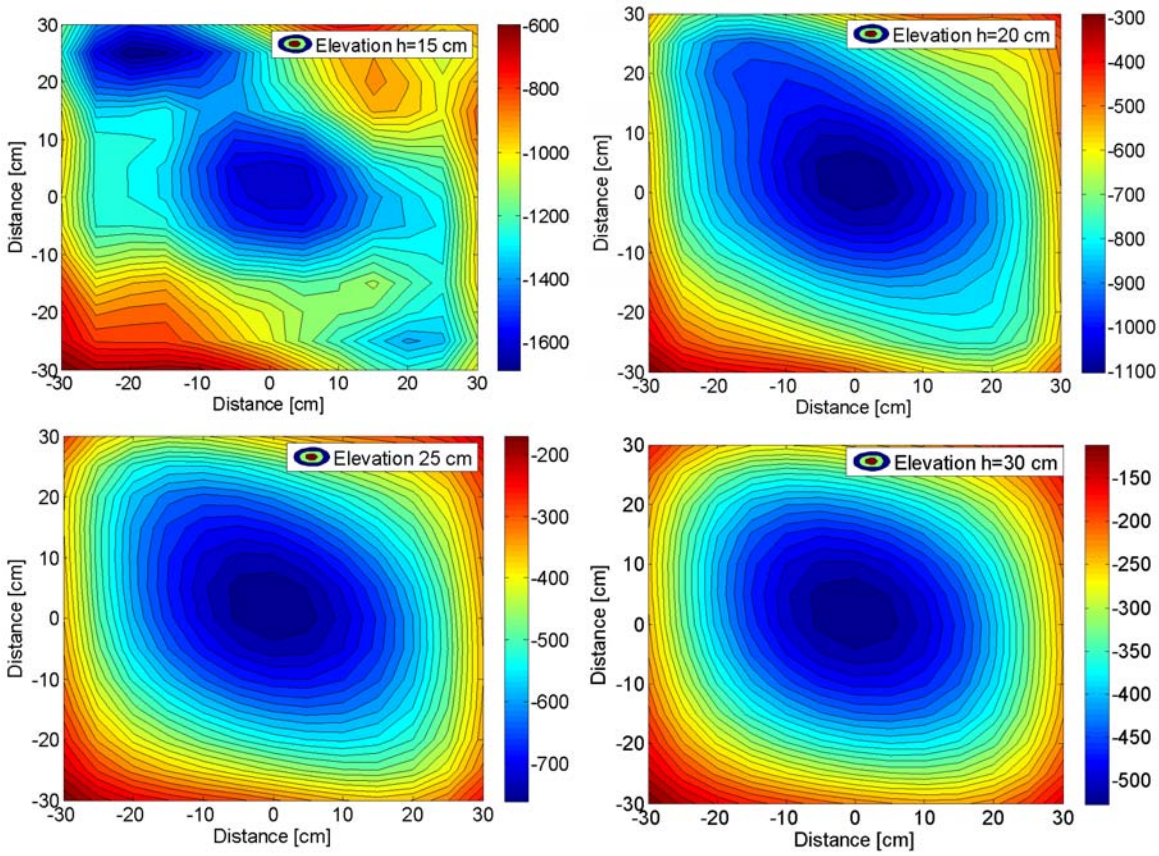

Figure A.6: As the sensor is raised, the contribution of clutter to the overall EMI response is reduced compared to the response of the 105mm UXO.

A.4 Algorithm for Joint Diagonalization

The joint diagonalization algorithm we use [71, 74, 75] is a generalization of Jacobi's procedure to find the eigenvalues of a single matrix. Formally we solve the optimization problem

$$\begin{aligned} \min_{V} \quad & \frac{1}{2}\sum_{q=1}^{N_g}\sum_{i\neq j}\left([VA(t_q)V^T]_{ij}\right)^2 \\ \text{s.t.} \quad & V^TV = I, \end{aligned} \tag{A.4.1}$$

which we accomplish by making repeated Givens-Jacobi similarity transformations designed to gradually accumulate the "content" of the matrices on their diagonals until a certain tolerance level is reached. The transformations are of the form $A(t_q) \to A'(t_q) = V_{rs}A(t_q)V_{rs}^T$, with the matrix V_{rs} being the identity but with the four elements V_{rr}, V_{rs}, V_{sr}, and V_{ss} replaced by the two-dimensional rotation array

$$\begin{bmatrix} \cos\phi_{rs} & \sin\phi_{rs} \\ -\sin\phi_{rs} & \cos\phi_{rs} \end{bmatrix}, \quad \text{with} \quad \tan 2\phi_{rs} = \frac{f_{rs}}{n_{rs} + \sqrt{f_{rs}^2 + n_{rs}^2}}, \tag{A.4.2}$$

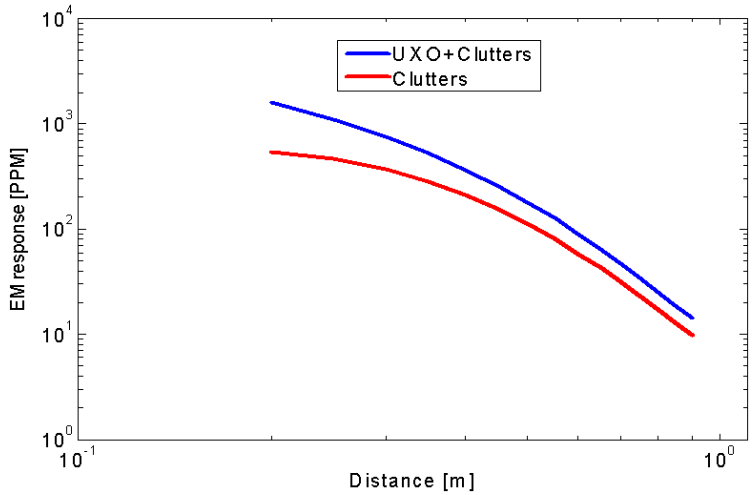

Figure A.7: Projected data as a function of elevation at the center of the measurement grid.

where

$$n_{rs} = \sum_q \left\{ [a_{rr}(t_q) - a_{ss}(t_q)]^2 - [a_{rs}(t_q) + a_{sr}(t_q)]^2 \right\}, \tag{A.4.3}$$

$$f_{rs} = 2\sum_q [a_{rr}(t_q) - a_{ss}(t_q)][a_{rs}(t_q) + a_{sr}(t_q)]. \tag{A.4.4}$$

The indices are swept systematically, and the procedure is repeated until convergence is reached. The computational burden is equivalent to that of diagonalizing the matrices one by one. The resulting eigenvalues and eigenvectors are all real because all the MSR matrices are symmetric.

We have also solved the nonlinear constrained optimization problem A.4.1 directly using sequential quadratic programming as implemented in the function *fmincon* of the Matlab Optimization Toolbox. This procedure unsurprisingly takes a longer time to run than the Givens-Jacobi algorithm sketched above. The two procedures gave equivalent results in all cases we tried; Fig. 4.17 (lower) shows an example.

A.5 The Green Tensor

We assume that each source that contributes to produce the secondary field is an anisotropic dipole with an associated set of principal axes such that a primary magnetic field pointing along each axis induces a dipole moment parallel to the field. The proportionality factors are the principal polarizabilities, the intrinsic signatures that we ultimately seek. The principal axes do not necessarily coincide with the global coordinate frame defined by the sensor, which dictates the direction of the primary field; thus we must transform the field to the principal "body" frame, compute the moment, and transform back to the global system. At the end of the process we obtain

$$\mathbf{M} = P\mathbf{H}^{\mathrm{pr}} \equiv \begin{bmatrix} m_{xx} & m_{xy} & m_{xz} \\ m_{xy} & m_{yy} & m_{yz} \\ m_{xz} & m_{yz} & m_{zz} \end{bmatrix} \begin{bmatrix} H_x^{\mathrm{pr}} \\ H_y^{\mathrm{pr}} \\ H_z^{\mathrm{pr}} \end{bmatrix} \tag{A.5.1}$$

for the induced dipole moment. The polarizability tensor P is symmetric, since it results from an orthogonal similarity transformation on a diagonal matrix, and (A.5.1) displays this symmetry explicitly. Inserting expression (A.5.1) into the field of a point dipole,

$$\mathbf{H} = \frac{3(\mathbf{M}\cdot\mathbf{R})\mathbf{R} - \mathbf{M}R^2}{4\pi R^5}, \tag{A.5.2}$$

where $\mathbf{R} = \mathbf{r} - \mathbf{r}' \equiv X\hat{\mathbf{x}} + Y\hat{\mathbf{y}} + Z\hat{\mathbf{z}}$ points from the location of the source to the observation point, introducing the stretched-out polarizability vector

$$\mathbf{m} = \begin{bmatrix} m_{xx} & m_{xy} & m_{xz} & m_{yy} & m_{yz} & m_{zz} \end{bmatrix}^T \tag{A.5.3}$$

and rearranging, we obtain

$$\mathbf{H} = G\mathbf{m}, \tag{A.5.4}$$

where

$$G = \frac{3}{4\pi R^5}\begin{bmatrix} (X^2-\frac{R^2}{3})H_x^{\mathrm{pr}} & (X^2-\frac{R^2}{3})H_y^{\mathrm{pr}} + XY\,H_x^{\mathrm{pr}} & (X^2-\frac{R^2}{3})H_z^{\mathrm{pr}} + XZ\,H_x^{\mathrm{pr}} & XY\,H_y^{\mathrm{pr}} & XY\,H_z^{\mathrm{pr}} + XZ\,H_y^{\mathrm{pr}} & XZ\,H_z^{\mathrm{pr}} \\ YX\,H_x^{\mathrm{pr}} & YX\,H_y^{\mathrm{pr}} + (Y^2-\frac{R^2}{3})H_x^{\mathrm{pr}} & YX\,H_z^{\mathrm{pr}} + YZ\,H_x^{\mathrm{pr}} & (Y^2-\frac{R^2}{3})H_y^{\mathrm{pr}} & (Y^2-\frac{R^2}{3})H_z^{\mathrm{pr}} + YZ\,H_y^{\mathrm{pr}} & YZ\,H_z^{\mathrm{pr}} \\ ZX\,H_x^{\mathrm{pr}} & ZX\,H_y^{\mathrm{pr}} + ZY\,H_x^{\mathrm{pr}} & ZX\,H_z^{\mathrm{pr}} + (Z^2-\frac{R^2}{3})H_x^{\mathrm{pr}} & ZY\,H_y^{\mathrm{pr}} & ZY\,H_z^{\mathrm{pr}} + (Z^2-\frac{R^2}{3})H_y^{\mathrm{pr}} & (Z^2-\frac{R^2}{3})H_z^{\mathrm{pr}} \end{bmatrix} \tag{A.5.5}$$

is the 3 ×6 Green tensor of (4.4.1) [78, 82]. When there is more than one transmitter operating in sequence (as is the case with TEMTADS, where there are 25) the primary field in the matrix of (A.5.5) ceases to be unique. These additional data points can be threaded into the tensor by adding rows to the matrix, which as a result has size $3N_t \times 6$, where N_t is the number of transmitters. As we discuss in the text, the field and polarizability of (A.5.3) can also be transformed into matrices in order to incorporate the time dependence. After finding $\mathbf{m}$ one can use joint diagonalization [71, 108] to extract the time-dependent intrinsic signatures and the "body" axes associated with the different sources. The procedure finds a single orthogonal matrix V such that at each time gate t_k the polarizability tensor $P(t_k) = V\Lambda(t_k)\,V^T$ with Λ as diagonal as possible [64]. These diagonal elements constitute the ONVMS amplitudes, and the columns of V give the orientation of each dipole.

B List of Scientific/Technical Publications

Publications produced in whole or part with funds from this project are [17, 78, 95, 96, 100, 109, 114, 119–123, 151–158].

C Other Supporting Materials

References

[1] Fridon Shubitidze, Irma Shamatava, Alex Bijamov, Ben Barrowes, and Kevin O'Neill. Camp butner uxo data inversion and classification using advanced emi models. 2010. SERDP-MR-1572. 1, 69, 83

REFERENCES

[2] Mark Prouty. Draft demonstration plan: Detection and classification with the MetalMapper™ at former Camp San Luis Obispo. San Jose, CA: Geometrics, Inc. (http://www.geometrics.com), 2009. 1, 46, 81

[3] Juan Pablo Fernandez, Benjamin Barrowes, Alex Bijamov, Tomasz Grzegorczyk, Nicolas Lhomme, Kevin O'Neill, Irma Shamatava, and Fridon Shubitidze. MPV-II: an enhanced vector man-portable emi sensor for uxo identification. volume 8017, page 801707. SPIE, 2011. doi: 10.1117/12.884085. URL http://link.aip.org/link/?PSI/8017/801707/1. 1, 46, 49, 81

[4] H. H. Nelson, D. A. Steinhurst, B. Barrow, T. Bell, N. Khadar, B. SanFilipo, and I. J. Won. Enhanced UXO discrimination using frequency-domain electromagnetic induction. Final report to the ESTCP program office (DOD) Arlington VA for project MM-0601, Naval Research Laboratory, 2007. URL http://oai.dtic.mil/oai/oai?&verb=getRecord&metadataPrefix=html&identifier=ADA469893. Accession Number : ADA469893. 1, 71, 83

[5] B. Spargo. ESTCP MR-201165 Demonstration Data Report Former Camp Beale TEMTADS MP 2x2 Cart Survey. Technical report, ESTCP technical report, 2011. 1, 71, 81, 82

[6] F. Shubitidze, K. O'Neill, K. Sun, and I. Shamatava. Interaction between highly conducting and permeable metallic objects in the EMI frequency range. Annual Review of Progress in Applied Computational Electromagnetics, pages 625 – 631, 2003. 2

[7] F. Shubitidze, K. O'Neill, I. Shamatava, K. Sun, and K.D. Paulsen. Analysis of EMI scattering to support UXO discrimination: Heterogeneous and multi objects. Proceedings of SPIE - The International Society for Optical Engineering, 5089(2):928 – 939, 2003. ISSN 0277-786X. 2

[8] Wei Hu, Stacy L. Tantum, and Leslie M. Collins. EMI-based classification of multiple closely spaced subsurface objects via independent component analysis. IEEE Transactions on Geoscience and Remote Sensing, 42(11): 2544 – 2554, 2004. ISSN 0196-2892. 2, 9, 47, 69

[9] Chandra S. Throckmorton, Stacy L. Tantum, Yingyi Tan, and Leslie M. Collins. Independent component analysis for UXO detection in highly cluttered environments. Journal of Applied Geophysics, 61(3-4):304 – 317, 2007. ISSN 0926-9851. 2

[10] Ian T. McMichael and Carl V. Nelson. Investigation of the electromagnetic induction spatial response of two closely spaced targets. volume 5089, pages 894 – 903, Orlando, FL, United States, 2003. 2, 9

[11] F. Shubitidze, K. O'Neill, S.A. Haider, Keli Sun, and K.D. Paulsen. Application of the method of auxiliary sources to the wide-band electromagnetic induction problem. IEEE Transactions on Geoscience and Remote Sensing, 40(4):928 – 42, 2002/04/. ISSN 0196-2892. 2

[12] K. O'Neill, K. Sun, C.C. Chen, F. Shubitidze, and K.D. Paulsen. Combining GPR and EMI Data for Discrimination of Multiple Subsurface Metallic Objects. volume 7, pages 4157 – 4159, Toulouse, France, 2003. 2, 9

[13] K. Sun, K. O'Neill, C.-C. Chen, H. S. Youn, F. Shubitidze, I. Shamatava, , and K.D. Paulsen. Highly contaminated UXO sites: combination of GPR and EMI for discrimination of clustered scatterers. SAGEEP, 2005. 2, 9

[14] F. Shubitidze, K. O'Neill, I. Shamatava, K. Sun, , and K. D. Paulsen. Total magnetic charge for fast screening of highly contaminated UXO sites. In proceedings of 2005 IEEE international symposium on Antennas and Propagation and USNC/CN/URSI North American Radio Science meeting, on CD, 2005. 2, 70, 95

[15] I. Shamatava, F. Shubitidze, C.C. Chen, H.S. Youn, K. O'Neill, and K. Sun. Potential benefits of combining EMI and GPR for enhanced UXO discrimination at highly contaminated sites. Proceedings of SPIE - The International Society for Optical Engineering, 5415(PART 2):1201 – 1210, 2004. ISSN 0277-786X. 2

[16] Leslie M. Collins, Yan Zhang, and Lawrence Carin. Model-based statistical sensor fusion for unexploded ordnance detection. volume 3, pages 1556 – 1559, Toronto, Ont., Canada, 2002. 2

[17] F. Shubitidze, B. Barrowes, I. Shamatava, and K. O'Neill. Multiple subsurface targets localization from next-generation EMI sensor data using MUSIC algorithm. Proc. IEEE Int. Geosci. Remote Sensing Symp. (IGARSS), 2010. 2, 102

[18] F. Shubitidze, B. Barrowes, and K. O'Neill. Normalized surface magnetic charge for UXO discrimination: multiple objects. SERDP Partners Symposium, November 2006. Poster. 3, 70, 95

[19] K. O'Neill, S.A. Haider, S. Geimer, and K.D. Paulsen. Effects of the ground surface on polarimetric features of broadband radar scattering from subsurface metallic objects. IEEE Trans. on Geosci. Remote Sens., 39(6): 1556–1565, June 2001. 8

[20] Chi-Chih Chen, Matthew B. Higgins, Kevin O'Neill, and Richard Detsch. Ultrawide-bandwidth fully-polarimetric ground penetrating radar classification of subsurface unexploded ordnance. IEEE Trans. Geosci. Remote Sens., 39:1221–1230, June 2001. 8

[21] C. E. Baum. Detection and Identification of Visually Obscured Targets. Taylor & Francis, Philadelphia, 1999. 8

[22] John David Jackson. Classical Electrodynamics. Wiley, New York, 2nd edition, 1975. 8, 11

[23] T. H. Bell, B. J. Barrow, and J. T. Miller. Subsurface discrimination using electromagnetic induction sensors. IEEE Trans. on Geoscience and Remote Sensing, 39(6):1286–1293, June 2001. 8

[24] Yan Zhang, L. Collins, Haitao Yu, C.E. Baum, and L. Carin. Sensing of unexploded ordnance with magnetometer and induction data: theory and signal processing. IEEE Transactions on Geoscience and Remote Sensing, 41(5):1005 – 15, 2003/05/. ISSN 0196-2892. 8, 47, 69

[25] C. O. Ao, H. Braunisch, K. O'Neill, and J. A. Kong. Quasi-magnetostatic solution for a conducting and permeable spheroid with arbitrary excitation. IEEE Trans. on Geoscience and Remote Sensing, 40(4):887–897, April 2002. 8

[26] Benjamin E. Barrowes, Kevin O'Neill, Tomasz M. Grzegorczyk, Xudong Chen, and Jin A. Kong. Broadband analytical magnetoquasistatic electromagnetic induction solution for a conducting and permeable spheroid. IEEE Trans. on Geoscience and Remote Sensing, 42(11):2479–2489, November 2004. 8

[27] Tomasz M. Grzegorczyk, Beijia Zhang, Jin Au Kong, Benjamin E. Barrowes, and Kevin O'Neill. Electromagnetic induction from highly permeable and conductive ellipsoids under arbitrary excitation - application to the detection of unexploded ordnances. IEEE Trans. on Geoscience and Remote Sensing, 46(4):1164–1176, April 2008. 8

[28] F. Shubitidze, K. O'Neill, B.E. Barrowes, I. Shamatava, J.P. Fernandez, K. Sun, and K.D. Paulsen. Application of the normalized surface magnetic charge model to UXO discrimination in cases with overlapping signals. Journal of Applied Geophysics, 61(3-4):292 – 303, 2007. ISSN 0926-9851. 8, 48, 70

[29] C. D. Moss, T. M. Grzegorczyk, K. O'Neill, and J. A. Kong. A hybrid time domain model of electromagnetic induction from conducting, permeable targets. IEEE Trans. on Geoscience and Remote Sensing, 44(10):2916–2926, October 2006. 8

[30] S. L. Tantum and L. M. Collins. A comparison of algorithms for subsurface target detection and identification using time-domain electromagnetic induction data. IEEE Trans. on Geosci. Remote Sens., 2001. 9

[31] Xudong Chen, K. O'Neill, T.M. Grzegorczyk, and Jin Au Kong. Spheroidal mode approach for the characterization of metallic objects using electromagnetic induction. IEEE Transactions on Geoscience and Remote Sensing, 45(3):697 – 706, 2007/03/. ISSN 0196-2892. 9

REFERENCES

[32] Fridon Shubitidze, Juan Pablo Fernández, Benjamin E. Barrowes, Irma Shamatava, and Kevin O'Neill. Normalized Surface Magnetic Source model applied to Camp Sibert data: Discrimination studies. In Applied Computational Electromagnetics Symposium (ACES), Monterey, CA, Mar. 2009. 9

[33] Juan Pablo Fernández, Fridon Shubitidze, Irma Shamatava, Benjamin E. Barrowes, and Kevin O'Neill. Realistic subsurface anomaly discrimination using electromagnetic induction and an svm classifier. Applied Computational Electromagnetics Journal. 9, 51

[34] Chandra S. Throckmorton, Stacy L. Tantum, Yingyi Tan, and Leslie M. Collins. Independent component analysis for UXO detection in highly cluttered environments. Journal of Applied Geophysics, 61(3-4):304–317, 2007. 9

[35] Lin-Ping Song, Douglas W. Oldenburg, Leonard R. Pasion, and Stephen D. Billings. Transient electromagnetic inversion for multiple targets. SPIE Proceedings, 7303, May 2009. 9, 13

[36] A. J. Devaney. Time reversal imaging of obscured targets from multistatic data. 53(5):1600–1610, May 2005. doi: 10.1109/TAP.2005.846723. 9

[37] F. Shubitidze, B. Barrowes, I.Shamatava, and K. O'Neill. Multiple subsurface target localization from next generation EMI sensor data using MUSIC algorithm. IGARSS, 2010. 9

[38] Yu Zhong and Xudong Chen. MUSIC imaging and electromagnetic inverse scattering of multiply scattering small anisotropic spheres. 55(12):3542–3549, December 2007. doi: 10.1109/TAP.2007.910488. 9

[39] Tomasz M. Grzegorczyk, Benjamin Barrowes, Fridon Shubitidze, J. P. Fernandez, Irma Shamatava, and Kevin O'Neill. Kalman filters applied to the detection of unexploded ordnance. In Proc. of SPIE, Detection and Sensing of Mines, Explosive Objects, and Obscured Targets, volume 7664, 2010. doi: 10.1117/12.848564. Orlando, FL. 9

[40] Tomasz M. Grzegorczyk, Benjamin Barrowes, Fridon Shubitidze, J. P. Fernandez, Irma Shamatava, and Kevin O'Neill. Detection of multiple subsurface metallic targets using EMI data. In Proc. of SPIE, Detection and Sensing of Mines, Explosive Objects, and Obscured Targets, volume 73030T, 2009. Orlando, FL. 9

[41] H. H. Nelson and J. R. McDonald. Multi-sensor towed array detection system (mtads) for uxo detection. IEEE Trans. on Geosci. Remote Sens., 39(6):1139–1145, June 2001. 10

[42] H. H. Nelson, D. A. Steinhurst, B. Barrow, T. Bell, N. Khadar, B. SanFilipo, and I. J. Won. Enhanced UXO discrimination using frequency-domain electromagnetic induction. Final report to the ESTCP program office (DOD) Arlington VA for project MM-0601, Naval Research Laboratory, 2007. URL http://oai.dtic.mil/oai/oai?&verb=getRecord&metadataPrefix=html&identifier=ADA469893. Accession Number : ADA469893. 10

[43] David C. George and Joan L. George. Data report: Tests of MPV at Vicksburg, February 26 to March 2, 2007. Technical Note 2007-2. Grand Junction, CO: G&G Sciences Inc. (http://www.ggsciences.com), 2007. 10, 11

[44] Julius Adams Stratton. Electromagnetic Theory. McGraw-Hill, New York, 1941. 11

[45] Fridon Shubitidze, Kevin ONeill, Shah A. Haider, Keli Sun, and Keith D. Paulsen. Application of the method of auxiliary sources to the wide-band electromagnetic induction problem. IEEE Trans. on Geosci. Remote Sens., 40(4):928–942, April 2002. 11

[46] F. Shubitidze, K. ONeill, I. Shamatava, and K. Sun. Coupling between highly conducting and permeable metallic objects in the emi frequency range. Applied computational electromagnetic society Journal, pages 139–148, March 2004. 11

[47] Henning Braunisch, Chi O. Ao, Kevin ONeill, and Jin A. Kong. Magnetoquasistatic response of a distribution of small conducting and permeable objects. In IEEE 2000 International Geoscience and Remote Sensing Symposium, 2000. 11

[48] F. Shubitidze, K. O'Neill, I. Shamatava, K. Sun, and K. D. Paulsen. A standardized excitation approach for classification of buried UXO. In IEEE 2000 International Geoscience and Remote Sensing Symposium, volume 7, pages 4905–4908, 2004. 13

[49] Jonathan Miller. Classification using electromagnetic induction sensors. In UXO Forum, Orlando, FL, 24-27 August 2009. 13

[50] . We acknowledge the work of Dr. Dan Steinhurst of Nova Research Inc. in acquiring TEMTADS data. 15

[51] . We acknowledge the work of Drs. Gregory Schultz, Sam Segal, and Irma Shamatava of Sky Research Inc. in acquiring MPV data. 15

[52] . We acknowledge the private communication with Dr. James Kingdon of SAIC for the validation of single target TEMTADS inversion results. 19

[53] Fridon Shubitidze, David Karkashadze, Juan Pablo Fernandez, Benjamin E. Barrowes, Kevin O'Neill, Tomasz M. Grzegorczyk, and Irma Shamatava. Applying a volume dipole distribution model to next-generation sensor data for multi-object data inversion and discrimination. Proc. of SPIE, page 766407, 2010. 19

[54] F.G. Bogdanov, R.S. Zaridze, D.D. Karkashadze, and Ph.F. Shubitidze. Modified auxiliary sources method for investigation of diffraction on the voluminous bodies of complicated form. pages 69 – 72, Lviv, Ukraine, 1996. 27

[55] F. G. Bogdanov, D. D. Karkashadze, and R. S. Zaridze. The method of auxiliary sources in electromagnetic scattering problems. Generalized multipole techniques for electromagnetic and light scattering: Elsevier Science, 1999. 27, 47

[56] David Karkashadze, Juan Pablo Fernandez, and Fridon Shubitidze. Scatterer localization using a left-handed medium. Optics Express, 17(12):9904 – 9917, 2009. ISSN 10944087. URL http://dx.doi.org/10.1364/OE.17.009904. 27

[57] Yogadhish Das, John E. McFee, Jack Toews, and Gregory C. Stuart. Analysis of an electromagnetic induction detector for real-time location of buried objects. IEEE Trans. Geosci. Remote Sens., 28:278–288, May 1990. 27

[58] Bruce J. Barrow and H. H. Nelson. Model-based characterization of electromagnetic induction signatures obtained with the MTADS electromagnetic array. IEEE Trans. Geosci. Remote Sens., 39:1279–1285, June 2001. 27

[59] Thomas H. Bell, Bruce J. Barrow, and Jonathan T. Miller. Subsurface discrimination using electromagnetic induction sensors. IEEE Trans. Geosci. Remote Sens., 39:1286–1293, June 2001. 27

[60] Leonard R. Pasion and Douglas W. Oldenburg. A discrimination algorithm for UXO using time-domain electromagnetic induction. J. Environ. Eng. Geophys., 6:91–102, 2001. 27

[61] Yan Zhang, Leslie Collins, Haitao Yu, Carl E. Baum, and Lawrence Carin. Sensing of unexploded ordnance with magnetometer and induction data: Theory and signal processing. IEEE Trans. Geosci. Remote Sensing, 41:1005–1015, May 2003. 27

[62] J. Torquil Smith and H. Frank Morrison. Estimating equivalent dipole polarizabilities for the inductive response of isolated conductive bodies. IEEE Trans. Geosci. Remote Sens., 42:1208–1214, June 2004. 27, 47

[63] Ashley B. Tarokh, Eric L. Miller, I. J. Won, and Haoping Huang. Statistical classification of buried objects from spatially sampled time or frequency domain EMI data. Radio Sci., 39:RS4S05, June 2004. 27, 47, 69

[64] Juan Pablo Fernández, Benjamin E. Barrowes, Tomasz M. Grzegorczyk, Nicolas Lhomme, Kevin O'Neill, and Fridon Shubitidze. A man-portable vector sensor for identification of unexploded ordnance. IEEE Sensors Journal, 2011. In press. 27, 47, 48, 51, 70, 81, 102

[65] Fridon Shubitidze, Kevin O'Neill, Benjamin E. Barrowes, Irma Shamatava, Keli Sun, Juan Pablo Fernández, and Keith D. Paulsen. Application of the normalized surface magnetic charge model to UXO discrimination in cases with overlapping signals. J. Appl. Geophys., 61:292–303, Mar. 2007. 27, 28, 38

[66] Fridon Shubitidze, David Karkashadze, Juan Pablo Fernández, Benjamin E. Barrowes, Kevin O'Neill, Tomasz Grzegorczyk, and Irma Shamatava. Applying a volume dipole distribution model to next-generation sensor data for multi-object data inversion and discrimination. In Russell S. Harmon, J. Thomas Broach, and John H. Holloway, Jr., editors, Detection and Sensing of Mines, Explosive Objects, and Obscured Targets XV, volume 7664 of Proceedings of SPIE, pages 7664–07, Bellingham, WA, Apr. 2010. 27, 28

[67] Lin-Ping Song, Douglas W. Oldenburg, Leonard R. Pasion, and Stephen D. Billings. Transient electromagnetic inversion for multiple targets. In Russell S. Harmon, J. Thomas Broach, and John H. Holloway, Jr., editors, Detection and Sensing of Mines, Explosive Objects, and Obscured Targets XIV, volume 7303 of Proceedings of SPIE, page 73030R, Bellingham, WA, May 2009. 27

[68] Lin-Ping Song, Leonard R. Pasion, Stephen D. Billings, and Douglas W. Oldenburg. Nonlinear inversion for multiple objects in transient electromagnetic induction sensing of unexploded ordnance: Technique and applications. IEEE Transactions on Geoscience and Remote Sensing, 49(10 PART 2):4007 – 4020, 2011. ISSN 01962892. URL http://dx.doi.org/10.1109/TGRS.2011.2132138. 27

[69] Tomasz M. Grzegorczyk, Benjamin E. Barrowes, Fridon Shubitidze, Juan Pablo Fernandez, and Kevin O'Neill. Simultaneous identification of multiple unexploded ordnance using electromagnetic induction sensors. IEEE Transactions on Geoscience and Remote Sensing, 2011. ISSN 01962892. URL http://dx.doi.org/10.1109/TGRS.2011.2108302. 27, 49

[70] P. Comon. Independent component analysis, a new concept? Signal Processing, pages 287–314, 1994. 28

[71] A. Belouchrani, K. Abed-Meraim, J.-F. Cardoso, and E. Moulines. A blind source separation technique using second-order statistics. IEEE Transactions on Signal Processing, 45:434–444, 1997. 28, 32, 48, 100, 102

[72] S. Harmeling, A. Ziehe, M. Kawanabe, and K.-R. Müller. Kernel-based nonlinear blind source separation. Neural Computation, 2003. 28

[73] Dan A. Steinhurst, Glenn R. Harbaugh, Jim B. Kingdon, T. Furuya, Dean A. Keiswetter, and David C. George. EMI array for cued UXO discrimination. ESTCP Project MM-0601 Final Report, http://www.serdp.org/Program-Areas/Munitions-Response/Land/Sensors/MR-200601/MR-200601, July 2010. 28, 46

[74] B. N. Flury and W. Gautschi. An algorithm for simultaneous orthogonal transformation of several positive definite symmetric matrices to nearly diagonal form. SIAM Journal on Scientific and Statistical Computing, 1986. 32, 100

[75] Jean-François Cardoso and Antoine Souloumiac. Jacobi angles for simultaneous diagonalization. SIAM J. Matrix Anal. Appl., 17(1):161–164, Jan. 1996. 32, 100

[76] Juan Pablo Fernández, Benjamin E. Barrowes, Kevin O'Neill, Irma Shamatava, and Fridon Shubitidze. Realistic subsurface anomaly discrimination using electromagnetic induction and an SVM classifier. EURASIP Journal on Advances in Signal Processing, 2010:305890, 2010. 38

[77] Irma Shamatava, Fridon Shubitidze, Juan Pablo Fernández, Benjamin E. Barrowes, Kevin O'Neill, Tomasz M. Grzegorczyk, and Alex Bijamov. SLO blind data set inversion and classification using physically complete models. In Russell S. Harmon, J. Thomas Broach, and John H. Holloway, Jr., editors, Detection and Sensing of Mines, Explosive Objects, and Obscured Targets XV, volume 7664 of Proceedings of SPIE, pages 7664–03, Bellingham, WA, Apr. 2010. 38

[78] F. Shubitidze, J. P. Fernandez, B. E. Barrowes, K. O'Neill, I. Shamatava, and A. Bijamov. Comparison of the physically complete model with a simple dipole model for UXO detection and discrimination. Detection and Sensing of Mines, Explosive Objects, and Obscured Targets Xv, 7664, 2010. doi: 10.1117/12.850654. 38, 57, 70, 102

[79] Success classifying small munitions at camp butner, 2010. URL http://serdp-estcp.org/News-and-Events/In-the-Spotlight-Archive/Success-Classifying-Small-Munitions-at-Camp-Butner. 38, 44

[80] A. Andrews, H. H. Nelson, and K. Kaye. Estcp pilot program: Classification approaches in munitions response, camp butner, north carolina, 2011. URL http://serdp-estcp.org/content/download/10723/136271/version/4/file/Butner+Demonstration+Program+Office+Final+Report+July.pdf. 38, 40

[81] S. Cazares, M. Tuley, and E. Ayers. The uxo classification demonstration at former camp butner, nc, 2011. URL http://serdp-estcp.org/content/download/12777/151554/version/1/file/IDA_Camp+ButnerReport1-13.pdf. 38, 40, 44, 47, 51, 52, 57

[82] F. Shubitidze, D. Karkashadze, J. P. Fernandez, B. E. Barrowes, K. O'Neill, Grzegorczyk, and I. Shamatava. Applying a volume dipole distribution model to next-generation sensor data for multi-object data inversion and discrimination. Detection and Sensing of Mines, Explosive Objects, and Obscured Targets Xv, 7664, 2010. doi: 10.1117/12.850651. 40, 47, 70, 102

[83] T. Maehara and K. Murota. Simultaneous singular value decomposition. Linear Algebra and its Applications, 2011. 46

[84] Sailaja V. Chilaka, Daniel L. Faircloth, Lloyd S. Riggs, and Herb H. Nelson. Enhanced discrimination among UXO-like targets using extremely low-frequency magnetic fields. IEEE Trans. on Geosci. Remote Sens., 44 (1):10–21, January 2006. 46

[85] J.D. McNeill and M. Bosnar. Application of time domain electromagnetic techniques to UXO detection. 1996. 46

[86] Erika Gasperikova, J. Torquil Smith, H. Frank Morrison, Alex Becker, and Karl Kappler. UXO detection and identification based on intrinsic target polarizabilities—A case history. Geophysics, 74:B1–B8, Jan.-Feb. 2009. 46

[87] I. J. Won, D. A. Keiswetter, D. Hansen, E. Novikova, and T. M. Hall. Gem-3: a monostatic broadband electromagnetic induction sensor. Jour. Envir. Eng. Geophysics, 2(1):53–64, 1997. 46

[88] K. O'Neill, I.J. Won, A. Oren, Chi-Chih Chen, Hyoun-Sun Youn, Xudong Chen, and Keli Sun. Data diversity for UXO discrimination in realistic settings with a handheld EMI sensor. Proceedings of the SPIE - The International Society for Optical Engineering, 5415(1):253 – 62, 2004. ISSN 0277-786X. 46

[89] J.P. Fernandez, B. Barrowes, K. O'Neill, I. Shamatava, and F. Shubitidze. A vector handheld frequency-domain sensor for uxo identification. In Proceedings of the SPIE - The International Society for Optical Engineering, volume 7303, pages 73030W (12 pp.) –, USA, 2009. URL http://dx.doi.org/10.1117/12.818812. 46

[90] H.H. Nelson and J.R. McDonald. Multisensor towed array detection system for uxo detection. IEEE Transactions on Geoscience and Remote Sensing, 39(6):1139 – 1146, 2001. ISSN 01962892. URL http://dx.doi.org/10.1109/36.927427. 46

[91] D.D. Snyder and David C. George. The advanced ordnance locator (AOL): A dual-mode TEM and magnetics system for detection and classification of UXO. SAGEEP, Envir. & Eng. Geophys. Soc., 2005. Atlanta, GA. 46

[92] Yan Zhang, Xuejun Liao, and Lawrence Carin. Detection of buried targets via active selection of labeled data: Application to sensing subsurface UXO. IEEE Trans. Geosci. Remote Sensing, 42:2535–2543, Nov. 2004. 47

[93] Alireza Aliamiri, Jack Stalnaker, and Eric L. Miller. Statistical classification of buried unexploded ordnance using nonparametric prior models. IEEE Trans. Geosci. Remote Sens., 45:2794–2806, Sep. 2007. 47, 69

[94] Qiuhua Liu, Xuejun Liao, and L. Carin. Detection of unexploded ordnance via efficient semisupervised and active learning. IEEE Trans. Geosci. Remote Sens., 46:2558–2567, Sep. 2008. 47, 69

[95] Fridon Shubitidze, Juan Pablo Fernandez, Irma Shamatava, Benjamin E. Barrowes, and Kevin O'Neill. Realistic subsurface anomaly discrimination using electromagnetic induction and an svm classifier. Eurasip Journal on Advances in Signal Processing, 2010, 2010. ISSN 16876172. URL http://dx.doi.org/10.1155/2010/305890. 47, 69, 102

[96] A. Bijamov, F. Shubitidze, J. P. Fernández, B. E. Barrowes, I. Shamatava, and K. O'Neill. Camp Butner live-site UXO classification using hierarchical clustering and Gaussian mixture modeling. IEEE Trans. Geosci. Remote Sens., submitted for publication. 47, 57, 102

[97] T.H. Bell, B.J. Barrow, and J.T. Miller. Subsurface discrimination using electromagnetic induction sensors. IEEE Trans. on Geoscience and Remote Sensing, 39(6):1286 – 1293, June 2001. 47, 48, 70

[98] L. Carin, H. Yu, Y. Dalichaouch, A.R. Perry, P.V. Czipott, and C.E. Baum. On the wideband EMI response of a rotationally symmetric permeable and conducting target. IEEE Transactions on Geoscience and Remote Sensing, 39(6):1206 – 1213, 2001. ISSN 0196-2892. 47

[99] L. R. Pasion and D. W. Oldenburg. A discrimination algorithm for UXO using time domain electromagnetics. J. Engg & Envir. Geophys, Vol. 20:pp91–102, 2001. 47, 48, 69, 72

[100] Fridon Shubitidze, Juan Pablo Fernandez, Irma Shamatava, Leonard R. Pasion, Benjamin E. Barrowes, and Kevin O'Neill. Application of the normalized surface magnetic source model to a blind unexploded ordnance discrimination test. Applied Computational Electromagnetics Society Journal, 25(1):89 – 98, 2010. ISSN 10544887. 47, 52, 70, 71, 102

[101] Fridon Shubitidze, Kevin O'Neill, Irma Shamatava, Keli Sun, and Keith D. Paulsen. Fast and accurate calculation of physically complete EMI response by a heterogeneous metallic object. IEEE Transactions on Geoscience and Remote Sensing, 43(8):1736 – 1750, 2005. ISSN 0196-2892. 47

[102] K. Sun, K. O'Neill, F. Shubitidze, I. Shamatava, and K.D. Paulsen. Fast data-derived fundamental spheroidal excitation models with application to UXO identification. Proceedings of SPIE - The International Society for Optical Engineering, 5415(PART 2):855 – 865, 2004. ISSN 0277-786X. 47

[103] Fridon Shubitidze, David Karkashadze, Benjamin E. Barrowes, Irma Shamatava, and Kevin O'Neill. A new physics based approach for estimating a buried object's location, orientation and magnetic polarization from EMI data. J. Env. Eng. Geophys., 13:115–130, Sep. 2008. 48

[104] Rainer Storn and Kenneth Price. Differential evolution - a simple and efficient adaptive scheme for global optimization over continuous spaces. Technical Report TR-95-012, Berkeley, CA, 1995. 48, 82

[105] R. Storn. System design by constant adaptation and differential evolution. IEEE Trans. Evol. Comput., 1999. 48, 82

[106] X. Chen, K. O'Neill, B. E. Barrowes, T. M. Grzegorczyk, , and Jin Au Kong. Application of a spheroidal mode approach with differential evolution in inversion of magneto-quasistatic data for UXO discrimination. Inverse Problems, 20(6):27–40, 2004. 48

[107] C. E. Baum, editor. Detection and Identification of Visually Obscured Targets. Taylor & Francis, Philadelphia, PA, 1999. 48

[108] J. F. Cardoso and A. Souloumiac. Jacobi angles for simultaneous diagonalization. SIAM Journal of Matrix Analysis and Applications, 17(1):161–164, 1996. 48, 102

[109] Fridon Shubitidze, Juan Pablo Fernandez, Irma Shamatava, Benjamin E. Barrowes, and Kevin O'neill. Joint diagonalization applied to the detection and discrimination of unexploded ordnance. Geophysics, 77(4):WB149 – WB160, 2012. ISSN 00168033. URL http://dx.doi.org/10.1190/geo2011-0387.1. 48, 52, 57, 71, 102

[110] Lin-Ping Song, Douglas W. Oldenburg, and Leonard R. Pasion. Estimating source locations of unexploded ordnance using the multiple signal classification algorithm. Geophysics, 77(4):WB127 – WB135, 2012. ISSN 00168033. URL http://dx.doi.org/10.1190/geo2011-0379.1. 49

[111] Mathematical Handbook for Scientists and Engineers. New York: McGraw-Hill, 1968. 49

[112] Matrix Algebra: Theory, Computations, and Applications in Statistics. New York: Springer, 2007. 49

[113] Lin-Ping Song, Fridon Shubitidze, Leonard R. Pasion, Douglas W. Oldenburg, and Stephen D. Billings. Computing transient electromagnetic response of a metallic object with a spheroidal excitation approach. Geoscience and Remote Sensing, IEEE Transactions Letter, 2008. 49, 51

[114] I. Shamatava, F. Shubitidze, J. P. Fernandez, B. E. Barrowes, K. O'Neill, T. M. Grzegorczyk, and A. Bijamov. Slo blind data set inversion and classification using physically complete models. Detection and Sensing of Mines, Explosive Objects, and Obscured Targets Xv, 7664, 2010. doi: 10.1117/12.850621. 51, 102

[115] J.T. Miller, T.H. Bell, J. Soukup, and D. Keiswetter. Simple phenomenological models for wideband frequency-domain electromagnetic induction. IEEE Transactions on Geoscience and Remote Sensing, 39(6):1294 – 1298, 2001. ISSN 0196-2892. 52

[116] J. R. Wait and K. P. Spies. Quasi-static transient response of a conducting and permeable sphere. Geophysics, 34:789–792, Oct. 1969. 55

[117] Leonard R. Pasion, Stephen D. Billings, Douglas W. Oldenburg, and Sean E. Walker. Application of a library based method to time domain electromagnetic data for the identification of unexploded ordnance. J. Appl. Geophys., 61:279–291, Mar. 2007. 55

[118] T. Fawcett. Roc graphs: Notes and practical considerations for data mining researchers. Technical report, Hewlett-Packard, Palo Alto, CA, 2003. Tech. Rep. HPL-2003-4. 57

[119] I. Shamatava, F. Shubitidze, J. P. Fernandez, A. Bijamov, B. E. Barrowes, and K. O'Neill. Live-site uxo classification studies using advanced emi and statistical models. volume 8017, page 801709. SPIE, 2011. doi: 10.1117/12.884404. URL http://link.aip.org/link/?PSI/8017/801709/1. 57, 82, 83, 102

[120] Fridon Shubitidze, Benjamin E. Barrowes, Irma Shamatava, Juan Pablo Fernandez, Alex Bijamov, and Kevin O'Neill. Advanced uxo discrimination: resolving multiple targets and overlapping emi signals. volume 8017, page 80170A. SPIE, 2011. doi: 10.1117/12.884405. URL http://link.aip.org/link/?PSI/8017/80170A/1. 57, 102

REFERENCES

[121] Fridon Shubitidze, Ben Barrowes, Irma Shamatava, Juano Pablo Fernndez, and Kevin O'Neill. The orthonormalized volume magnetic source technique applied to live-site uxo data: Inversion and classification studies. SEG Special Issue, September 2011. 57, 102

[122] F. Shubitidze, J. P. Fernndez, J. Miller, J. Keranen, B. E. Barrowes, and A. Bijamov. Inversion and classification studies of live-site production-level metalmapper data sets. pages 835704–835704–10, 2012. doi: 10.1117/12.919565. URL +http://dx.doi.org/10.1117/12.919565. 57, 102

[123] F. Shubitidze, J. P. Fernndez, I. Shamatava, A. Luperon, B. E. Barrowes, K. O'Neill, and A. Bijamov. Inversion-free discrimination of unexploded ordnance in real time. pages 835705–835705–9, 2012. doi: 10.1117/12.919549. URL +http://dx.doi.org/10.1117/12.919549. 57, 82, 83, 102

[124] A. Paski. Former camp butner site description and EM61 data collection and analysis. SERDP-ESTCP Partners Symposium, 2010. 69

[125] L. Pasion. Uxo discrimination using full coverage and cued interrogation data sets at camp butner, nc. SERDP-ESTCP Partners Symposium, 2010. 69

[126] Stacy L. Tantum and Leslie M. Collins. A comparison of algorithms for suburface target detection and identification using time-domain electromagnetic induction data. IEEE Trans. Geosci. Remote Sens., 39:1299–1306, June 2001. 69

[127] David Williams, Yijun Yu, Levi Kennedy, Xianyang Zhu, and Lawrence Carin. A bivariate gaussian model for unexploded ordnance classification with emi data. IEEE Geoscience and Remote Sensing Letters, 4(4):629 – 633, 2007. ISSN 1545598X. URL http://dx.doi.org/10.1109/LGRS.2007.903972. 69

[128] Laurens Beran and Douglas W. Oldenburg. Selecting a discrimination algorithm for unexploded ordnance remediation. IEEE Transactions on Geoscience and Remote Sensing, 46(9):2547 – 2557, 2008. ISSN 01962892. URL http://dx.doi.org/10.1109/TGRS.2008.921394. 69

[129] S. D. Billings. Processing and Discrimination Strategies for Next-Generation EMI Sensor Data. SERDP and ESTCP Partners in Environmental Technology Technical Symposium & Workshop, 2009. Washington, DC. 69

[130] Alex Bijamov, Fridon Shubitidze, Juan Pablo Fernandez, Irma Shamatava, Benjamin E. Barrowes, and Kevin O'Neill. Comparison of supervised and unsupervised machine learning techniques for uxo classification using emi data. volume 8017, page 801706. SPIE, 2011. doi: 10.1117/12.884076. URL http://link.aip.org/link/?PSI/8017/801706/1. 69, 70, 71, 72, 73

[131] David Williams, Chunping Wang, Xuejun Liao, and Lawrence Carin. Classification of unexploded ordnance using incomplete multisensor multiresolution data. IEEE Trans. on Geosci. Remote Sens., 45(7):2364–2373, July 2007. 69

[132] Yan Zhang, Leslie M. Collins, and Lawrence Carin. Unexploded ordnance detection using bayesian physics-based data fusion. Integrated Computer-Aided Engineering, 10(3):231 – 247, 2003. ISSN 10692509. 69

[133] F. Shubitidze, K. O'Neill, I. Shamatava, K. Sun, and K.D. Paulsen. A simple magnetic charge model for classification of multiple buried metallic objects in cases with overlapping signals. SAGEEP, 2005. 70

[134] F. Shubitidze, B. Barrowes, J. P. Fernández, Irma Shamatava, and K. O'Neill. NSMC for UXO discrimination in cases with overlapping signatures. SPIE, 2007. 70, 95

[135] Fridon Shubitidze, Kevin O'Neill, Irma Shamatava, Keli Sun, and Keith Paulsen. Combined differential evolution and surface magnetic charge model algorithm for discrimination of UXO from non-UXO items: Simple and general inversions. Proceedings of SPIE - The International Society for Optical Engineering, 5794(PART I):346 – 357, 2005. ISSN 0277-786X. 70

[136] MR-201165, 2011. URL http://www.serdp.org/Program-Areas/Munitions-Response/Land/Live-Site-Demonstrations/MR-201165/MR-201165. 71

[137] Statistics Toolbox User's Guide. The MathWorks, Natick, MA. 72

[138] J. H. Ward. Hierarchical grouping to optimize an objective function. Journal of the American Statistical Association, 58:236–244, 1963. 73

[139] Clustering. Wiley-IEEE Press, 2008. 73

[140] G. N. Lance and W. T. Williams. A general theory of classificatory sorting strategies. 2. clustering systems. Computer Journal, 10, 1967. 73

[141] Algorithms for clustering data. Prentice Hall, 1988. 73

[142] J. Quackenbush. Computational analysis of microarray data. Nat Rev Genet, 2, 2001. 73

[143] P. C. Mahalanobis. On the generalized distance in statistics. Proceedings of the National Institute of Sciences of India, pages 49–55, 1936. 73

[144] Multivariate Statistical Inference and Applications. Wiley, New York, 1998. 73

[145] Estcp uxo classification study, former camp beale, ca. Technical report, Environmental Security Technology Certification Program, Arlington, VA, 2010. 81

[146] Fridon Shubitidze, Benjamin E. Barrowes, Irma Shamatava, Juan P. Fernández, and Kevin O'Neill. Application of the nsms model to multi-axis time domain emi data. Proceedings of SPIE - The International Society for Optical Engineering, 6953:The International Society for Optical Engineering (SPIE) –, 2008. ISSN 0277786X. 81

[147] B. Barrowes and K. O'Neill. Recent Developments in Vector Man-Portable EMI Sensors. SERDP Partners Symposium, December 2007. Presentation. 81

[148] Ben Barrowes. Man-portable vector time domain emi sensor and discrimination processing: SERDP MM1443 - FY06 annual report. Technical report, The Strategic Environmental Research and Development Program (SERDP), 2012. 81

[149] F. Shubitidze, K. O'Neill, B. Barrowes, J. P. Fernández, I. Shamatava, K. Sun, and K.D. Paulsen. Application of the normalized surface magnetic charge model to UXO discrimination in cases with overlapping signals. J. Appl. Geophys., 61(3-4):292–303, Mar. 2007. 82

[150] K. O'Neill, Keli Sun, F. Shubitidze, I. Shamatava, and K.D. Paulsen. Accounting for the effects of widespread discrete clutter in subsurface EMI remote sensing of metallic objects. IEEE Transactions on Geoscience and Remote Sensing, 44(1):32 – 46, 2006. ISSN 0196-2892. 97

[151] T. M. Grzegorczyk, B. Barrowes, F. Shubitidze, J. P. Fernandez, and K. O'Neill. Simultaneous discrimination of multiple unexploded ordnance using electromagnetic induction sensors. IEEE Trans. on Geosci. Remote Sens., 2010. Accepted for publication. 102

[152] Ben Barrowes, Tomasz Grzegorczyk, Fridon Shubitidze, Pablo Fernandez, and Kevin O'Neill. Techniques in electromagnetic induction for discriminating multiple targets. Memphis, TN, Nov 18 2009. USACE Research and Development Conference. 102

[153] J. P. Fernandez, B. Barrowes, A. Bijamov, T. Grzegorczyk, K. O'Neill, I. Shamatava, and F. Shubitidze. Combining electromagnetic induction and automated classification in a uxo discrimination blind test. Detection and Sensing of Mines, Explosive Objects, and Obscured Targets Xv, 7664, 2010. doi: 10.1117/12.850446. 102

REFERENCES

[154] T. M. Grzegorczyk, B. Barrowes, F. Shubitidze, J. P. Fernandez, I. Shamatava, and K. O'Neill. Kalman filters applied to the detection of unexploded ordnance. Detection and Sensing of Mines, Explosive Objects, and Obscured Targets Xv, 7664, 2010. doi: 10.1117/12.848564. 102

[155] K. O'Neill, B. E. Barrowes, F. Shubitidze, J. P. Fernandez, T. M. Grzegorczyk, and I. Shamatava. Upward continuation of emi data for sensing of subsurface uxo in cluttered, multi-object cases. Detection and Sensing of Mines, Explosive Objects, and Obscured Targets Xv, 7664, 2010. doi: 10.1117/12.850441. 102

[156] T.M. Grzegorczyk, B. Barrowes, F. Shubitidze, J.P. Fernandez, I. Shamatava, and K. ONeill. Detection of multiple subsurface metallic targets using emi data. In Proceedings of the SPIE - The International Society for Optical Engineering, volume 7303, 2009. 102

[157] I. Shamatava, J. P. Fernndez, B. E. Barrowes, K. O'Neill, A. Bijamov, and F. Shubitidze. Camp beale live-site handheld-sensor data inversion and classification using advanced emi models. pages 835706–835706–10, 2012. doi: 10.1117/12.919586. URL +http://dx.doi.org/10.1117/12.919586. 102

[158] Benjamin E. Barrowes, Fridon Shubitidze, Tomasz M. Grzegorczyk, Pablo Fernndez, and Kevin O'Neill. Pedemis: a portable electromagnetic induction sensor with integrated positioning. pages 835702–835702–10, 2012. doi: 10.1117/12.918321. URL +http://dx.doi.org/10.1117/12.918321. 102